EFFECTS OF INITIAL CONDITIONS AND MACH NUMBER ON TURBULENT MIXING TRANSITION OF SHOCK-DRIVEN VARIABLE-DENSITY FLOW

A Dissertation
Presented to
The Academic Faculty

By

Mohammad Mohaghar

In Partial Fulfillment
of the Requirements for the Degree
Doctor of Philosophy in the
School of Mechanical Engineering

Georgia Institute of Technology

May 2019

EFFECTS OF INITIAL CONDITIONS AND MACH NUMBER ON TURBULENT MIXING TRANSITION OF SHOCK-DRIVEN VARIABLE-DENSITY FLOW

Approved by:

Professor Devesh Ranjan, Advisor
School of Mechanical Engineering
Georgia Institute of Technology

Professor Ari Glezer
School of Mechanical Engineering
Georgia Institute of Technology

Professor Suresh Menon
School of Aerospace Engineering
Georgia Institute of Technology

Professor Donald Webster
School of Civil Engineering
Georgia Institute of Technology

Professor Cyrus Aidun
School of Mechanical Engineering
Georgia Institute of Technology

Date Approved: March 8, 2019

“Do not let your difficulties fill you with anxiety, after all it is only in the darkest nights that stars shine more brightly.”

-Ali Ibn Abi Talib AS

To my beloved wife, my best friend, my great companion, Zeinab, whose endless love and support made this work possible. To my son, Mehdi, for coping with the undue paternal deprivation during the course of my study. To my parents, Ali and Maasoumeh, for their unconditional trust, selfless love, and endless patience. To my parents-in-law, Mirsaeid and Hamideh, for their sincere encouragement and support despite the long distance between us.

ACKNOWLEDGEMENTS

There are a number of people without whom this thesis might not have been written, including my family members, my great friends in our group, and the scholars whom I had the privilege to meet and work with.

First and foremost, there are no proper words to convey my deep gratitude and respect for my thesis and research advisor, Professor Devesh Ranjan. He has trusted me to work on one of the main experimental facilities in his lab, the shock tube, even though my previous background was completely computational. He inspired me to become an independent researcher and helped me realize the power of critical reasoning. He also demonstrated what a brilliant and hard-working scientist can accomplish. His commitment to guide me for carrying out high-impact and high-quality research has helped me to form a visionary research personality and be always ambitious about my goals.

I am also grateful to the members of my PhD committee: Professor Ari Glezer, Professor Cyrus Aidun, Professor Donald Webster, and Professor Suresh Menon. They generously gave their time to offer me valuable comments toward improving my work.

I am also grateful to all the current and previous members of STAM Lab who supported and worked with me to make my PhD enjoyable and memorable. First of all, I would like to thank my friend and colleague in the shock tube project, John Carter, for his continued support. This dissertation would not have been possible without the experimental and intellectual contribution of John. I will not forget all days and crazy nights that we spent together to produce the highest quality data in our field. Moreover, I would like to thank my great friend and mentor, Dr. Jacob McFarland. Thanks for being patient with me during our heated research discussions and giving me your precious feedback comments. I would also like to thank my other colleague in the first two years of this journey, David Reilly, who taught me several experimental details of this project. In addition, I am grateful to work with Dr. Svyatoslav Yorish, who gave me great suggestions and helped me

regarding modifying experimental setups. I am also so thankful to my fellow labmates, Mark Mikhaeil, Stephen Johnston, Prasoon Suchandra, Benjamin Musci, Dan Fries, and Dr. Gokul Pathikonda for always being supportive and providing great ideas and technical comments. Also, I thank my other fellow labmates, Sandeep Pidaparti, Miad Karimi, Sam Lim, Steven Roth, Sam Petter, Taegyu Kang, Cameron Ahmad, Jessica Imgrund, Alon Katz, Malavika Bagepalli, Justin Yarrington, Dr. Vladimer Tsiklashvili, and Dr. Dorrin Jarrahbashi for all the fun we have had during these years. I should not forget to also thank my undergraduate students who I had the privilege to mentor and supervise, Juan Sebastian Rubio (collecting $M \sim 1.9$ data), Brandon Conner, Debapriya Bhattacharjee, Cody Huggins, and Karamjit Singh (collecting $M \sim 1.55$ data). I greatly look forward to having all of you as colleagues in the years ahead.

During my PhD, thanks to my advisor, I had the opportunity to discuss my work with several scholars in the field. I would like to thank Dr. Ricardo Mejia-Alvarez for his guidance regarding proper orthogonal decomposition analysis, Professor Praveen Ramaprabhu and his group for their complete support and help to better understand FLASH code, and Dr. Oleg Schilling who always enthusiastically provided constructive feedback to our work and papers.

I would like to express my gratitude to my parents-in-law, Professor Mirsaeid Mousavi Karimi and Dr. Hamideh Haeri Tehrani, for their encouragement and support throughout the duration of my research. I also sincerely thank my sister-in-law, Zahra Mousavi Karimi, who has been always taking care of our son, Mehdi, whenever my wife and I were busy with our studies.

I deeply thank my parents, Professor Ali Mohaghar and Maasoumeh Tohidifar, who have been a source of encouragement and inspiration to me throughout my life. I salute you for the selfless love, care, pain and sacrifice you gave to shape my life. Thank you both for giving me the strength needed to chase my dreams. I would also like to thank my brother, Rohollah Mohaghar, and my sisters, Fatemeh Mohaghar and Maedeh Mohaghar,

who have also been generous with their love and encouragement despite the long distance between us.

I owe many thanks to the most special person in my life, my wife, Zeinab Mousavi Karimi. Thank you for always being around at times when I thought that it was impossible to continue this journey. Thank you for sacrificing almost two years of your PhD to take care of our son. Thank you for your belief in me during this journey. I greatly value your contribution, patience, and all your help during these challenging times. I also hope that my little son, Mehdi, will forgive me for being so preoccupied during writing of papers and this thesis, and long times that I spent in the laboratory trying to finish all of my experiments. I appreciate your patience, my son. Words would never be enough to convey my love and to show how grateful I am to both of you.

TABLE OF CONTENTS

LIST OF TABLES

LIST OF FIGURES

NOMENCLATURE

β	Growth rate exponent
β_{ij}	Normalized anisotropy
$\boldsymbol{\omega}$	Vorticity vector
$\boldsymbol{\tau}$	Viscous stress tensor
$\boldsymbol{u}$	Velocity vector
Δx_L	Distances from left side of the top row of the original image
Δx_R	Distances from right side of the top row of the original image
δz	Depth of field
δ	Mixing layer thickness
$\dot{\eta}$	Perturbation growth rate
$\dot{h}_0'$	Initial growth rate after reshock
$\dot{h}_0$	Initial growth rate after incident shock
η	Perturbation amplitude
η_0'	Amplitude after incident shock passes through the interface
Γ	Circulation
γ	Ratio of specific heats
$\hat{\phi}(x)$	Estimator for any statistics of the random variable x
λ	Wave length
λ_ν	Inner-viscous scale
λ_D	Diffusion scale (time-dependent scale)
λ_L	Liepmann-Taylor scale
λ_T	Taylor microscale

$\mathscr{M}$	Mixed-mass
ν_{mix}	Kinematic viscosity of the mixture
ρ	Density
ρ_1	Light gas density
ρ_2	Heavy gas density
τ	Dimensionless time
τ_i	Dimensionless time after incident shock
τ_r	Dimensionless time after reshock
θ	Mixedness
$\tilde{u_i}$	Mass weighted average velocity
ε	Attenuation coefficient
ζ	Normalized concentration
A	Atwood number across the interface
a	Turbulent mass flux
a_1	Speed of sound in the gas in the driven section
a_4	Speed of sound in the gas in the driver section
b	Density self-correlation
C_0	Pure light gas concentration
D	Particle displacement
$E_{\varphi'}$	One dimensional energy spectrum of any quantity
$f(r)$	Correlation function
h	Mixing width
I	Intensity of de-warped image
I_{trans}	Intensity of the straightened image
J	Pixel intensity along the light ray
K	Kinetic energy per unit area of the mixing region
k	Wave number

L_1 Integral scale

M Mach number

m Molecular mass

Mag Magnification

N_i Total number of independent samples

P Pressure

P_1 Pressure ahead of shock wave

P_2 Pressure behind shock wave

P_4 Driver pressure

R Gas constant

R_{ij} Favre-averaged Reynolds stress

Re Reynolds number

$S_2(r)$ Second order longitudinal structure function

std Standard deviation

$stderr$ Standard error

T Temperature

t Experimental time

t'^* time required for reshock to traverse the interface immediately before reshock

t^* time required for the shock wave to traverse the inclined interface

U Mean velocity in streamwise direction

u' Velocity fluctuation (from ensemble averaging)

u'' Velocity fluctuation from mass weighted average quantities

u'_{rel} Velocity fluctuation (from boxcar averaging)

u'_{span} Relative velocity minus the spanwise-averaged velocity

u_b Streamwise and spanwise spatial average of the velocity

u_{rel} Relative velocity

unc Uncertainty

V	Mean velocity in spanwise direction
v_0	Interface jump velocity after the incident shock
v_{rs}	Perturbation growth rate after reshock
w_i	Velocity of incident shock
X	Mole fraction
Y	Mass fraction
y_{int}	Vertical location of plano-concave cylindrical lens relative to the top of image
z_α	z-score for the normal distribution at the desired confidence interval (α)

SUMMARY

This thesis presents results on the effects of initial conditions (single- and multi-mode) and incident shock wave Mach numbers (M) on several mixing characteristics in Richtmyer–Meshkov instability (RMI) evolution. These goals are achieved by performing two different experimental campaigns using a shock strength with an incident Mach number of 1.9 and 1.55. Each campaign follows the interface evolution after interaction with incident shock and reflected shock from the wall (reshock). In addition, two different initial perturbations are imposed to study RMI evolution at each Mach number. The first perturbation is a predominantly single-mode long-wavelength interface which is formed by inclining the entire tube to 80° relative to the horizontal, and thus can be considered as half the wavelength of a triangular wave. The second initial condition is a multi-mode interface, containing additional shorter wavelength perturbations due to the imposition of shear and buoyancy on the inclined perturbation of the first case. In both single- and multi-mode cases at each Mach number, the interface consists of a nitrogen-acetone mixture as the light gas over carbon dioxide as the heavy gas (Atwood number, $A \sim 0.22$). The evolving density and velocity fields are measured simultaneously using planar laser-induced fluorescence (PLIF) and particle image velocimetry (PIV) techniques to provide the first detailed turbulence statistics measurements (i.e., Density, velocity, and density-velocity cross-statistics) using ensemble averaging for shock-accelerated variable density flows at $M > 1.5$ before and after reshock.

The evolution of mixing is investigated via the density fields by computing mixed-mass and mixing layer thickness, along with mixing width, mixedness, and the density self-correlation (DSC). It is shown that the amount of mixing is dependent on both the initial conditions and the incident shock Mach number before reshock. Evolution of the density self-correlation is discussed and the relative importance of different DSC terms is shown through fields and spanwise-averaged profiles. The localized distribution of vorticity and

the development of roll-up features in the flow is studied through the evolution of interface wrinkling and length of the interface edge, and indicates that the vorticity concentration shows a strong dependence on the Mach number. The contribution of different terms in the Favre-averaged Reynolds stress is shown, and while the $\langle\rho\rangle\langle u_i'u_j'\rangle$ term is dominant, a high dependency on the initial condition and reshock is observed for the turbulent mass-flux term. Regarding the effects of initial conditions, density and velocity data show that a distinct memory of the initial conditions is maintained in the flow before interaction with reshock. After reshock, the influence of the long-wavelength inclined perturbation present in both initial conditions is still apparent, but the distinction between the two cases becomes less evident as smaller scales are present even in the single-mode case.

Mixing transition is analyzed through two criteria: Reynolds number (Dimotakis, 2000) and time-dependent length scales (Robey *et al.*, 2003). The Reynolds number threshold is surpassed in all cases after reshock. In addition, the Reynolds number is around the threshold range for the multi-mode, high Mach number case (M $\sim$1.9) before reshock. However, the time-dependent length-scale threshold is surpassed by all cases only at the latest time after reshock, while all cases at early times after reshock and the high Mach number case at the latest time before reshock fall around the threshold. The scaling analysis of turbulent kinetic energy spectra after reshock at the latest time, at which mixing transition analysis suggests that an inertial range has formed, indicates power scaling of -1.8$\pm$0.05 for the low Mach number case and -2.1$\pm$0.1 for the higher Mach number case. This is related to the high anisotropy observed in this flow resulting from strong, large-scale, streamwise fluctuations produced by large-scale shear.

This work will help develop the capability to accurately predict and model extreme mixing, potentially leading to advances in a number of fields: energy, environment (atmospheric and oceanographic), aerospace engineering, and most pertinently, inertial confinement fusion (ICF).

CHAPTER 1
INTRODUCTION AND BACKGROUND

1.1 Overview

Strong shock waves from explosions or collisions produce highly compressible flows in a wide variety of physical situations covering broad ranges of spatial, temporal and energy scales including, but not limited to, astrophysical flows (Kane, Drake, and Remington, 1999; Kifonidis *et al.*, 2006; Arnett, 2000), supersonic combustion systems (Reilly *et al.*, 2015; Waitz, Marble, and Zukoski, 1993; Yang, Chang, and Bao, 2014; Marble, Hendricks, and Zukoski, 1989), shock propagation through foams and bubbly liquids, the fragmentation of gallstones or kidney stones by shock waves, and "high-energy-density" systems such as ICF devices. In the case of the ICF system, an understanding of the physical mechanisms responsible for the onset and evolution of instabilities in the non-linear stages may allow engineers to design a more efficient fuel pellet capable of producing higher yield at lower driving energy (Zhou, 2017; Brouillette, 2002; Ranjan, Oakley, and Bonazza, 2011; Niederhaus and Jacobs, 2003; Hogan, Bangerter, and Kulcinski, 1992; Lindl *et al.*, 2014). In these scenarios, the shock wave propagates through a medium with non-uniform thermodynamic properties; where several coupled hydrodynamic processes occur simultaneously, altering the geometry of the shock wave and the thermodynamic state of the medium. These processes include (1) shock-induced compression and heating; (2) shock-reflection, refraction and diffraction (or nonlinear acoustic effects); and (3) vorticity production. When the magnitude of these effects is great, they can significantly alter the behavior of the flow, and strongly distort and complicate the evolution of the fluid interface, often leading to the growth of features including secondary vortex rings, jetting, prominent and long-lived vortices, and eventually transition to turbulent mixing.

The mixing transition state refers to a turbulent state in which the flow drives rapid mixing down to the atomic scale. In this turbulent state, momentum will be dissipated rapidly, and large-scale motion will result in the entrainment of one fluid species into the other one. This leads to stretching and increased surface contact between mixing species, which leads to the generation of smaller scales than the largest eddy sizes. The evolution to a mixing transition requires the generation of a broad range of scales, which implies separation between large, driving scales, and viscous, dissipative scales. This concept was reported by Dimotakis (2000) for stationary or steady state fluid flows and he proposed a Reynolds number criteria for mixing transition. However, it is not properly understood if such a criteria exists in shock driven variable density flows. A critically large Reynolds number is a necessary but not sufficient criteria for turbulence transition in unsteady flows like shock-driven flows, since the inertial subrange also requires time to develop (Robey *et al.*, 2003).

Moreover, a thorough understanding of the memory of initial conditions through the mixing transition in instability-driven turbulent flows still remains a fundamental challenge. In certain shock and gravity driven variable-density flows, the memory of initial conditions (IC) remains noticeable as the flow transitions to turbulence (George and Davidson, 2004; George, 2008; Banerjee and Andrews, 2009; Kuchibhatla and Ranjan, 2013). Further insight into how the characteristic statistical behavior of transitional turbulence might depend upon these initial conditions can be provided by studying Richtmyer–Meshkov instability (RMI) (Richtmyer, 1960). RMI occurs at the interface of two impulsively accelerated fluids, each of different density. RMI is closely related to Rayleigh–Taylor instability (RTI) (Strutt, 1900; Taylor, 1950), which occurs when a heavy and a light fluid are both accelerated such that the density and pressure gradients are oriented in opposite directions, causing growth of initial interface perturbations. Conversely, RMI develops regardless of the relative position of the gases at the interface (heavy/light or light/heavy), and can be considered as an extension of RTI, where the constant acceleration of the interface is replaced by an

impulsive acceleration, e.g. a shock which amplifies initial perturbations on the interface. In both instabilities, the vorticity equation for compressible flow is

$$\frac{D\boldsymbol{\omega}}{Dt} = (\boldsymbol{\omega}\cdot\boldsymbol{\nabla})\boldsymbol{u} - \boldsymbol{\omega}(\boldsymbol{\nabla}\cdot\boldsymbol{u}) + \boldsymbol{\nabla}\times(\frac{1}{\rho}\boldsymbol{\nabla}\cdot\boldsymbol{\tau}) + \frac{1}{\rho^2}(\boldsymbol{\nabla}\rho\times\boldsymbol{\nabla}P) \tag{1.1}$$

where D/Dt is the material derivative, u is the flow velocity and τ is the viscous stress tensor. This equation highlights the relationship between vorticity (ω) and the gradient of density, ρ, and pressure, P, showing how the shock deposits baroclinic vorticity at the interface. For large Reynolds numbers, the viscous effect is negligible (τ is the viscous stress tensor). Moreover, upon initial shock, the baroclinic term is dominant over the vortex stretching $(\boldsymbol{\omega}\cdot\boldsymbol{\nabla})\boldsymbol{u}$ and the vortex dilation $\boldsymbol{\omega}(\boldsymbol{\nabla}\cdot\boldsymbol{u})$ terms, and therefore the vorticity equation can be approximated by the baroclinic production term

$$\frac{D\boldsymbol{\omega}}{Dt} \approx \frac{1}{\rho^2}(\boldsymbol{\nabla}\rho\times\boldsymbol{\nabla}P). \tag{1.2}$$

As the initial perturbations grow, vorticity further distorts the interface, and is a primary driving force of RMI evolution. As RMI progresses it induces turbulence and mixing, making it a phenomenon of interest to a variety of fields.

Understanding the physics responsible for the increase in mixing and turbulent behavior in these systems begins by recognizing the phenomena driving the production of vorticity. More specifically, the baroclinic production of vorticity at the interface is due to the misalignment of the pressure gradient (provided by the shock) and the density gradient between the two materials. In shock-accelerated flows, the strength of the pressure gradient is indicated by the Mach number (M) of the incident/reflected shock wave. The strength of the density gradient in a two fluid system is expressed nondimensionally by the Atwood number

$$A = \frac{\rho_2 - \rho_1}{\rho_2 + \rho_1}, \tag{1.3}$$

where the subscripts 1 and 2 respectively refer to the light fluid and heavy fluid. The Atwood number can be used for unshocked and shocked interfaces. Initial interface perturbations can be characterized by the ratio (α= η/λ) of their amplitude, η, to their wavelength, λ. Additionally, this parameter can be related to the growth rate of the overall mixing region, or extent of fluid interpenetration, and essentially defines the misalignment between the interface and the shock (see equation 1.1).

1.2 Perturbation Growth Models in Shock-driven Flow

The growth of Richtmyer-Meshkov instability can be broken down into various stages. To describe these stages, one can describe the interface perturbations as a wave or sum of waves. In the case of multi-mode perturbations, the interface can be decomposed into a Fourier series of modes . The instability first starts in a linear growth regime where perturbation amplitudes are much smaller than their wavelengths. As the interface evolves, their amplitudes begin to exceed their wavelength and they are considered to be in the nonlinear regime. At later times, vorticity causes the spikes, which is where the heavy gas penetrates into the light gas, to evolve, rolling up into mushroom shaped structures, and the Kelvin-Helmholtz shear instability causes small scale features to appear along the distorting interface. Eventually, breakdown of large scales to small scales can lead to turbulent mixing.

The onset of RM instabilities takes place in the linear regime and therefore the criteria for instability can be explored using the assumptions of the linear theory. According to analytical work using linear stability theory developed by Taylor (1950), the amplitude of sinusoidal perturbation on an interface between two fluids with different densities (heavy fluid over light fluid) under a gravitational acceleration, g, when the amplitude to wavelength ratio is much smaller than 1, $k\eta \ll 1$, grows as

$$\frac{d^2\eta(t)}{dt^2} = kgA\eta(t) \tag{1.4}$$

where η is the amplitude, $k = 2\pi/\lambda$ is the wavenumber, and A is the atwood number (Taylor, 1950). In Rayleigh–Taylor instability, where a heavy fluid is on top of a light fluid, as long as $k\eta \ll 1$, the interface perturbation grows exponentially in time (Richtmyer, 1960; Niederhaus and Jacobs, 2003; Collins and Jacobs, 2002; Brouillette and Sturtevant, 1989). It should be noted that the system is unstable as long as the acceleration direction is from heavy fluid to light fluid. However in the opposite direction, it will stabilize (Richtmyer, 1960; Brouillette, 2002; Niederhaus and Jacobs, 2003).

The formulation derived by Taylor was then expanded by Richtmyer to predict the growth of initial perturbations affected by an impulsive force (Richtmyer, 1960). The simple case when a weak planar shock wave propagates normal to the interface from light to heavy gas was investigated by Richtmyer. Assuming incompressibility in the flow and using linear stability theory, Richtmyer modified Taylor's equations by substituting the gravitational acceleration with a Dirac delta function (impulsive acceleration). The growth rate then is defined as

$$\dot{\eta} = kv_0 A\eta_0' \tag{1.5}$$

where v_0 is the interface jump velocity after the impulsive acceleration (incident shock) interacts with interface, $\eta_0' = \eta_0(1 - \frac{v_0}{w_i})$ is the amplitude at $t = 0$ ms, which is exactly after incident shock passes through the interface, and w_i is the velocity of incident shock. Linear growth only occurs when the amplitude is sufficiently small and $k\eta < 1$ (Niederhaus and Jacobs, 2003). Unlike RTI, it should be noted that the perturbation grows regardless of the direction of acceleration, and orientation of fluids in the Richtmyer–Meshkov instability. The difference in the case of a heavy fluid over a light fluid is that the amplitude of the interface after the passage of the shock initially decreases until the phase reverses, after which the interface grows in the linear regime as long as the condition of $k\eta < 1$ is satisfied (Brouillette, 2002; Niederhaus and Jacobs, 2003). The first experimental results which confirmed the theory derived by Richtmyer, were performed by Meshkov (1969).

After instability develops and the amplitude of the perturbation becomes larger than the wavelength, the interface grows nonlinearly, and eventually by breakdown of large scales to small scales, the flow reaches a state of turbulent mixing at late times. The non linear growth of RMI has been investigated for many decades. Several works found a power law growth for the mixing width (amplitude) in the nonlinear regime (Dimonte and Schneider, 1997; Dimonte and Schneider, 2000; Jacobs *et al.*, 2013; Weber *et al.*, 2014; Prasad *et al.*, 2000). The power law relationship can be derived using the kinetic energy per unit area of the mixing region,

$$K = \frac{1}{2}\rho h V^2 \tag{1.6}$$

where h and V are length scale (mixing width) and velocity magnitude. The dissipation rate of kinetic energy then is defined as

$$\frac{dK}{dt} = \frac{-cKV}{h}. \tag{1.7}$$

By implementing the definition of kinetic energy (equation 1.6) in the dissipation rate equation (equation 1.7), one can easily find

$$\frac{d(hV^2)}{dt} = -cV^3, \tag{1.8}$$

where c is a dissipation coefficient. Velocity is also related to mixing width using $V = dh/dt$. Therefore, the solution for this differential equation, can be written as $h \propto t^{\beta}$, where $\beta = \frac{2}{3+c}$ (*It should be noted that θ was used in the literature for growth rate exponent, however, θ is replaced by β here since θ will represent the mixedness parameter in chapter 4*). Although the nonlinear growth of RMI evolution has been studied experimentally and computationally for decades, there are still several unanswered questions related to this topic. Since a wide range of values have been reported by different works (Dimonte and Schneider, 1997; Dimonte and Schneider, 2000; Jacobs *et al.*, 2013; Weber *et al.*, 2014;

Prasad *et al.*, 2000), the β value and whether it should be constant for the whole nonlinear regime is an important topic in the RM field. In addition, effects of reshock and initial condition on the nonlinear growth rate are still not completely clarified nor understood. Several models which were suggested for non-linear regime in the literature are discussed and compared with mixing width data in chapter 4.1.2 (Richtmyer, 1960; Zhang and Sohn, 1997; Sadot *et al.*, 1998; McFarland, Greenough, and Ranjan, 2011).

1.3 Previous Studies

Having reviewed the theoretical work on RMI, the validation of these theories can now be examined through experiments and simulations. The experimental studies in RMI can be categorized based on two major factors, (1) method of generating impulsive acceleration and (2) method of creating initial perturbation. To address the first factor, three primary methods have been utilized: laser ablation, mechanical acceleration, and shock wave acceleration. In the laser ablation method, a high energy laser can be used to drive a high energy shock through an ablative material like polystyrene, polycarbonate or beryllium (Anderson *et al.*, 2000). The strength of shock waves in this method can go up to the order of 10 Mbar. Single-mode RMI (Blue *et al.*, 2005), blast wave driven RTI (Miles *et al.*, 2005) and also high energy KHI (Harding *et al.*, 2009) were studied using these laser driven experiments and their simulations.

Another method to generate the impulsive acceleration, which was employed by the University of Arizona, is to accelerate the mechanical system. In this experiment, a tank with stably stratified fluids is attached to a sled which is dropped and accelerated by a spring at the bottom of the rail (Chapman and Jacobs, 2006; Niederhaus and Jacobs, 2003). This sled method had also been used to perform RTI experiments by generating a continuous acceleration opposite to gravity (Jacobs and Catton, 1988), using rockets (Read, 1984) and linear electric motors (Dimonte and Schneider, 1996).

The final method employs a shock tube where the shock wave is generated mechani-

cally by the sudden release of pressure from driver section into the driven section. This mechanically generated shock wave intersects the interface which contains the density gradient. This shock wave can then reflect from the end wall of the tube and re-intersect the previously shocked interface, an event called reshock. The interaction of the developing interface with a second shock, which can be provided by the reflection of an incident shock at a wall, causes additional deposition of vorticity on a wider range of length scales. In this way, Balakumar *et al.* (2008b) showed that a rapid redistribution of previously ordered vorticity is believed to drive the mixing region to a turbulent state. Balakumar *et al.* (2008b) showed that the vortex configuration resulting from the initial shock advects material and neighboring vorticies, which strongly affect the extent of the mixing region and the state of the field that interacts with the reshock wave.

The methods to create a misaligned density gradient should be discussed in addition to the aforementioned methods for creating the necessary pressure gradient. Due to the importance of initial conditions on the evolving flow field, significant attention has been given to characterization and creation of the initial perturbation. The earliest method for perturbing the fluid interface was using a thin membrane to separate two fluids with a prescribed initial condition by Meshkov (1969). This method has been employed in many shock tube facilities (Brouillette and Sturtevant, 1994; Houas and Chemouni, 1996; Vetter and Sturtevant, 1995). However, this technique introduces membrane fragments into the mixing process, influencing instability development as well as complicating flow visualization. The late non-linear growth stages, however, were found to be relatively insensitive to the presence of the membrane, with the growth rates agreeing well with the theoretical predictions (Erez *et al.*, 2000). Using a soap film or fluid membrane to shape the interface such as in shock bubble interaction are another form of the membrane experiments (Ranjan, Oakley, and Bonazza, 2011; Niederhaus *et al.*, 2008; Ranjan *et al.*, 2005).

To avoid the problems associated with the interaction of the shock wave and membrane material in the flow field, subsequent researchers created membrane-less, slightly diffuse

interfaces between two gases. Using a plate to separate two gases and then retracting that plate before shock interaction is one method to create membrane-less interface. The shear which is induced by the retracting plate creates a perturbation (Bonazza and Sturtevant, 1996). This method also has been used in RTI experiments (Dalziel, 1993; Jacobs and Dalziel, 2005). One can also create a cylindrical membrane-less interface by dropping a column of heavy gas through a light gas (Jacobs, 1992; Quirk and Karni, 1996). Tomkins *et al.* (2003) considered two cylinders interacting with one another. This method was then extended to a gas curtain in a light-heavy-light configuration by creation of several cylinders together (Balakumar *et al.*, 2008a; Balasubramanian *et al.*, 2012; Balakumar *et al.*, 2012; Orlicz, Balasubramanian, and Prestridge, 2013; Orlicz *et al.*, 2015). In this configuration, the shock wave passes through the driver fluid to the test gas and then back to the driver gas and is limited to the case of three fluid interactions. The other membrane-less method is to rest a light fluid on top of a heavy fluid to create a stable stratification, and control diffusion by injecting continuous flow and creating exit ports at the interface location. Several various methods are then used to create single- and multi-mode perturbations along the interface. Jones and Jacobs (1997), Jacobs and Sheeley (1996), and Motl *et al.* (2009) used the resulting stable configuration to create a well-defined sinusoidal initial condition between the gases by horizontally oscillating the entire shock tube. The interface perturbation was also created by vertically oscillating the fluid in the shock tube (Long *et al.*, 2009; Jacobs *et al.*, 2013). The growth of the mixing layer thickness for a predominantly single-mode interface has been found to be different compared to a multi-mode interface. While imparting modal content on the interface is relatively easy using solid membranes to separate the gases, this is more complicated with membrane-less experiments. one method which is used to create a multi-mode interface is to perturb the interface by imparting a transverse shear layer (Weber *et al.*, 2012; Mohaghar *et al.*, 2017).

Finally, an inclined interface perturbation can be created in a membrane-less stratification of gases. This configuration which can be generated by inclining the shock tube, is a

simple and smart method to deposit baroclinic vorticity on the interface. McFarland *et al.* (2014) and Reilly *et al.* (2015) investigated the effects of inclination angle and reshock on circulation deposition using Mie-scattering and PIV techniques. The interface growth using a similar 'V' shaped interface was also recently investigated experimentally (Luo *et al.*, 2016).

The evolutions of the aforementioned interfaces have been observed in various ways as knowledge of RMI and technology has changed. The earliest studies on RMI viewed the growth of the perturbations and the interface growth using line-of-sight averaged methods such as scheliren and X-ray photography. But with the advent of planar optical diagnostic techniques such as quantitative-PLIF and PIV, recent studies have also investigated transition to turbulence and the subsequent turbulent mixing. Several works such as Orlicz *et al.* (2015) have attempted to compare their results to the criterion of Dimotakis (2005) on mixing transition in RMI. This transition is typically achieved using a sufficiently strong shock (high M) (Vetter and Sturtevant, 1995; Reese *et al.*, 2018; Orlicz, Balasubramanian, and Prestridge, 2013; Lombardini, Pullin, and Meiron, 2012; Orlicz *et al.*, 2009), large Atwood number (high A) (Balakumar *et al.*, 2008a; Motl *et al.*, 2009), modal content of inital interface perturbation (Weber *et al.*, 2012; Weber *et al.*, 2014), or by using the reflected shock to perturb the interface a second time (Balakumar *et al.*, 2012; Mohaghar *et al.*, 2017). For example, Weber *et al.* (2012) have observed a transition to turbulence and a broad range of scales even before reshock, using an interface with a continuous broadband spectrum perturbation consisting of structures with small separation of length scales. Alternatively, works such as Balakumar *et al.* (2012) have shown late time non-linear growth of RMI, but transition to turbulence only after reshock. Note that the vorticity deposition from the reshock will occur on a more corrugated interface and in the opposite sense (heavy to light gas) of the initial vorticity deposition.

Due to the complexity of RMI physics, there have also been many efforts dedicated to understanding RMI using computational methods. As in experimental work, compu-

tational studies have concentrated on modeling the instability evolution originating from different initial conditions, with great attention dedicated to understanding the evolution from well-defined, two-dimensional, harmonic initial conditions. Furthermore, just as advances in simulations have bolstered RMI experiments, the improvement of experimental diagnostic capabilities have improved the fidelity and breadth of information available for validating and improving simulations. RANS (Schilling and Latini, 2010; Morán-López and Schilling, 2013; Schwarzkopf *et al.*, 2016) and LES (Hill, Pantano, and Pullin, 2006; Thornber *et al.*, 2012) have been employed to investigate RMI in a similar sense. Schilling and Latini (2010) and Morán-López and Schilling (2013) have also used weighted essentially non-oscillatory (WENO) flux reconstruction in simulations to study the variable density physics and the associated evolution of turbulent kinetic energy in RMI. Schilling, Latini, and Don (2007) have also shown the necessity for higher order WENO simulations to accurately capture the instabilities inside the roll-ups in RMI. There have also been combined computational-experimental works evaluating the computational tools (Leinov *et al.*, 2009; McFarland, Greenough, and Ranjan, 2011; McFarland *et al.*, 2015; McFarland, Greenough, and Ranjan, 2014; Morgan *et al.*, 2012).

Particularly, Schilling, Latini, and Don (2007) performed simulations of single-mode RMI before and after reshock, and the results were compared to the Planar Laser Induced Fluorescence (PLIF) experimental work by Collins and Jacobs (2002), and Latini, Schilling, and Don (2007) compared dissipation effects using WENO methods of different orders. Ukai, Balakrishnan, and Menon (2011) also analyzed the accuracy of the growth models for both single- and multi-mode RMI before and after reshock.

McFarland, Greenough, and Ranjan (2011) furthered the relationship between experiments and simulations by performing a computational study of RMI development from an inclined interface covering multiple incident shock strengths, initial interface inclinations, and various Atwood numbers using ARES code. The research covered experiments performed on the shock tube which the present work was completed on, and was thus con-

strained to the capabilities of this facility. The interface mixing width is computed for wide range of Mach number and Atwood number, and a modified Richtmyer's model was proposed for inclined interface. This model includes the initial offset time that transmitted wave travels through the inclined interface. Morgan *et al.* (2012) also used ARES code to investigate late-time development of RMI in shock tubes, and later compared with a compressible version of the Miranda code (Cook and Cabot, 2005; Cook, 2007). The effect of different three-dimensional, multi-mode, small-scale initial perturbations on RMI evolution was previously investigated numerically by Thornber *et al.* (2011a) and Thornber *et al.* (2012) using implicit large-eddy simulation (ILES) with systematic grid refinement, which showed the mixing layer transition to a turbulent state.

The modal interactions of the initial conditions investigated in this thesis, a large-wavelength inclined interface perturbation and a small-wavelength multi-mode perturbation superimposed on the inclined interface, and their effect on RMI evolution were initially investigated using simulations by McFarland *et al.* (2015). The study includes an extension to 3-D and other improvements upon the work in McFarland, Greenough, and Ranjan (2011), as early simulations had some differences in qualitative results. These simulations encompassed a large range of parametric variations including the perturbation, resolution, and boundary conditions. The ARES work found that before reshock, distinct memory of initial condition was found in both large and small scales. However, as the post-reshock flow proceeded towards turbulence, it only retained some memory of the initial conditions for high-amplitude large-wavelength perturbations. The results and conclusions of this work have a large influence on the first objective of this thesis.

Overall, barring the recent work of Reese *et al.* (2018) ($M = 2.2$), RMI investigations using simultaneous PLIF/PIV have typically been in the $M < 1.5$ regime. Additionally, it should be noted that Reese *et al.* (2018) investigated effects of Mach number after incident shock on only multi-mode initial condition, and they did not have effects of reshock on the flow. Few experimental works performed at higher Mach numbers ($M > 1.5$) considered

integral measures (mixing width), and many of them collected only PLIF (density) measurements for mixing transition study. However, measurement of mixing width or density alone is insufficient to understand the relationships between kinetic energy, flow structures, scaling, and mixing. Moreover, previous mixing transition studies in shock-driven flows did not investigate effects of the initial condition on this subject. In addition, few shock tube experimental works have been performed using multi-mode initial conditions because the setup of controlled, repeatable, well quantified initial conditions of this kind are very hard to achieve in the laboratory. This is a fundamental difficulty in the investigation of mixing transition and turbulence statistics measurements in these unsteady flows. Moreover, a strong shock is essential to develop RMI to a late turbulent regime to investigate the asymptotic behaviour of the small scale mixing. While the effect of Mach number has been studied recently by Reese *et al.* (2018), the current work also attempts to leverage the presence of a well defined dominant mode (i.e., inclined interface) and a superposed multi-mode perturbation, and in addition to investigate turbulence statistics in the post-reshock regime. Therefore, despite previous efforts on shock-driven flows, how the Mach number and Atwood number affect modal interactions and transition to a turbulent mixing zone still represent the main open questions in the study of RMI.

1.4 Objectives and Outline of Present Work

The present experimental study aims to address the following objectives:

1. Quantify the effect of the initial conditions (single- and multi-mode) and the incident shock Mach number ($M \sim 1.55$ and $M \sim 1.9$) on the perturbation growth and mixing rate; and determine a critical value of Reynolds number necessary for turbulence transition to occur in these flows.

RMI evolution is studied for two different initial conditions at two times following the incident shock-interface interaction, and at two different times after the reflected shock

(reshock) has interacted with the evolving interface. The first initial condition is a predominantly single-mode (cases 1 and 3 in Table 1.1 or case S) long-wavelength interface which is formed by inclining the entire tube to 80° relative to the horizontal, yielding what can be considered as half of a triangular wave with an amplitude-to-wavelength ratio ($\frac{\eta}{\lambda}$=0.088). It should be noted that the gases are oriented so that the light gas rests on the heavy gas (light/heavy), i.e. the incident shock travels from the light to the heavy gas (nitrogen seeded with acetone/carbon dioxide, A$\sim$0.22). The second set of experiments, referred to as the multi-mode case (cases 2 and 4 in Table 1.1 or case M), were performed with a perturbed, multi-mode, inclined interface. The imposed perturbation creates density gradients of varying smaller scales, hypothesized to result in various sized density and velocity scales which develop in addition to the major scale of the inclined interface, and do so differently than the single-mode case. The effect of Mach numbers of $\sim$1.55 and $\sim$1.9 will be considered on both initial conditions. Concentration and velocity fields are obtained by performing instantaneous, simultaneous Planar Laser Induced Fluorescence (PLIF) and particle image velocimetry (PIV) measurements.

The results from the proposed experiments will investigate the early/transitional period of the growing mixing layer. In order to quantify the turbulent mixing transition we will calculate the Liepmann-Taylor scale ($\lambda_L = 5\delta Re^{-1/2}$) and inner viscous scale ($\lambda_\nu = 50\delta Re^{-3/4}$). Dimotakis proposed the notion of a mixing transition taking place at a universal value of the Reynolds number ($Re = 10,000 - 20000$) if $\lambda_L/\lambda_\nu > 1$. In our experiments the width of the mixing layer will be used as the outer length scale δ. The experimental measurements will be used to check the validity of this hypothesis for high Mach number conditions. For the first time in shock-driven flows, the mixing transition criteria which is suggested by Robey *et al.* (2003) for unsteady and time-dependent flows is investigated in addition to the one suggested by Dimotakis (2000).

2. Measure the change in growth rate upon interaction of the interface with reshock for both initial conditions and Mach numbers.

An aspect of shock-accelerated flow which is not yet completely understood is the effect of reshock on the turbulent mixing and the growth of the instability. Reshock is significant because it is believed to produce orders of magnitude increases in the molecular mixing and turbulence intensity. However, there are surprisingly few experiments capable of quantifying either of these effects, and those that exist were carried out using membranes to produce the initial interface. According to previous computational works, after reshock, a wide range of length scales becomes evident in the flow field, regions of very thorough mixing develop, and a disordered and apparently chaotic state arises, particularly evident when looking at the vorticity fields. Clearly, experiments are necessary where turbulence intensity and/or molecular mixing can be reliably quantified. The instability produced by the interaction of the incident shock wave on the density interface will be allowed to grow until it is reaccelerated by the shock wave reflected from the shock tube end wall. Determining the post reshock growth law and exponent is of importance as long as it is applicable. It should be noted that published studies of this type have found that the growth of the mixing zone is linear and only dependent on the reshock strength. However, these experiments used only a flat membrane to prepare the initial interface and employed only Schlieren visualization. It will therefore be interesting to compare those results with our proposed experiments, which will utilize our membrane-less approach with planar imaging diagnostics.

3. Acquire simultaneous density-velocity measurements of shock-accelerated variable-density flows to allow for the direct measurement of several turbulence quantities for the first time (for $M > 1.5$).

Simultaneous density-velocity measurements will be acquired for these flows using the process that will be explained in the flow diagnostics section. From the velocity field data, we can directly calculate the vorticity field in these experiments, allowing us to understand the vortex dynamics associated with shock accelerated flow. From the vorticity field, we

will calculate the circulation present in the system at a given time. This provides an opportunity to test the validity of the circulation models as well as to understand the connection between instantaneous scalar dissipation rate and the vorticity field. The well-controlled interface in our experiments also allows us to introduce ensemble averaging of the velocity and density fields, and to calculate the statistics of the averaged flow fields and of the fluctuating quantities. These averages will be calculated from experiments which have an almost identical initial interface. A complete turbulence database for shock-driven variable density flows (before and after reshock) will be generated which includes (but is not limited to) $\overline{\rho'^2}$,$\rho'u'$,$\rho'v'$; velocity fluctuations,$\overline{u'^2}$and $\overline{v'^2}$; and Reynolds stress, $\overline{u'v'}$. The careful analysis of the acquired temporal history of concentration and velocity fields from the planned experiments will allow researchers to evaluate physics-based turbulence mixing models for variable-density and compressible flows.

A summary of the experimental study in this thesis is presented in Table 1.1. For all cases, density field evolutions for the parametric study will be captured and included. The experimental times in the table are the ones which will be chosen to extract turbulence statistics through several realizations (more than 30 realizations at each time).

The organization of this dissertation is as follows. In chapter 2, the experimental facility used to conduct this study and the conditions in which the study was completed are discussed. Also, initial condition creation and characterization are investigated in detail. Chapter 3 includes PLIF image processing and PIV processing to obtain density and velocity data respectively, and uncertainty and error analysis in PLIF/PIV results are quantified. Furthermore, methods of velocity/density field decomposition in the RMI community, and how fluctuations are calculated, are discussed in chapter 3. Chapter 4 starts with a qualitative analysis of the density fields obtained from PLIF and shows the temporal evolution of the flow field for all experimental cases. Then, a complete quantitative analysis of the flow field using PLIF and PIV data is provided, and a discussion on the flow transition towards turbulence is presented. Finally, chapter 5 provides the conclusions for this study.

Table 1.1: Overview of the experimental study

Case no.	**1**	**2**	**3**	**4**
Gas pair	**(**N_2**-acetone)/** CO_2	**(**N_2**-acetone)/** CO_2	**(**N_2**-acetone)/** CO_2	**(**N_2**-acetone)/** CO_2
Initial Condition	Single-mode	Multi-mode	Single-mode	Multi-mode
Mach number	1.55	1.55	1.9	1.9
Initial Atwood number	0.22	0.22	0.22	0.22
Experimental times for turbulence statistics	2 pre-reshock 2 post-reshock	2 pre-reshock 2 post-reshock	2 pre-reshock 2 post-reshock	2 pre-reshock 2 post-reshock
Inclination angle of tube (Degrees)	80	80	80	80
Data points collected for evolution	12	12	20	20

CHAPTER 2
EXPERIMENTAL SETUP AND DIAGNOSTICS

2.1 The Shock Tube Facility

The experiments were performed at the inclined shock tube facility at Georgia Institute of Technology. The shock tube measures 9 m in total length and has an 11.43 cm by 11.43 cm internal cross section. It is designed to be capable of high incident shock Mach number experiments ($M \approx 2.5$ in air at atmospheric conditions) (Reilly *et al.*, 2015; McFarland *et al.*, 2014).

The shock tube consists of a driver section, driven section, and test section, which can be seen in Figure 2.1. The shock wave is generated by the rupture of a diaphragm separating the driver section from the driven. The design uses a hydraulic mechanism to secure the diaphragm between the flanges of the driver and driven sections. This design allows the use of strong diaphragm materials, such as mild steel, to produce a high difference in pressure across the diaphragm. Immediately prior to an experiment, the driver is filled to approximately 70% of the desired diaphragm break pressure. The experiment is initiated by opening a fast acting boost valve, resulting in high mass influx into the driver from a separate boost tank at a controlled pressure. This rapid increase in pressure pushes the diaphragm against an X shaped knife edge located in the driven section. Contact with the knife edge produces a dynamic break of the diaphragm and a near instantaneous release of the high pressure gas in the driver section.

The driven section provides sufficient distance for the translating pressure to coalesce into a shock wave and become planar. Pressure measurements are performed using two pressure transducers which are located directly above the test section. The distance between the two transducers is 10 cm. The second pressure transducer is used to trigger the

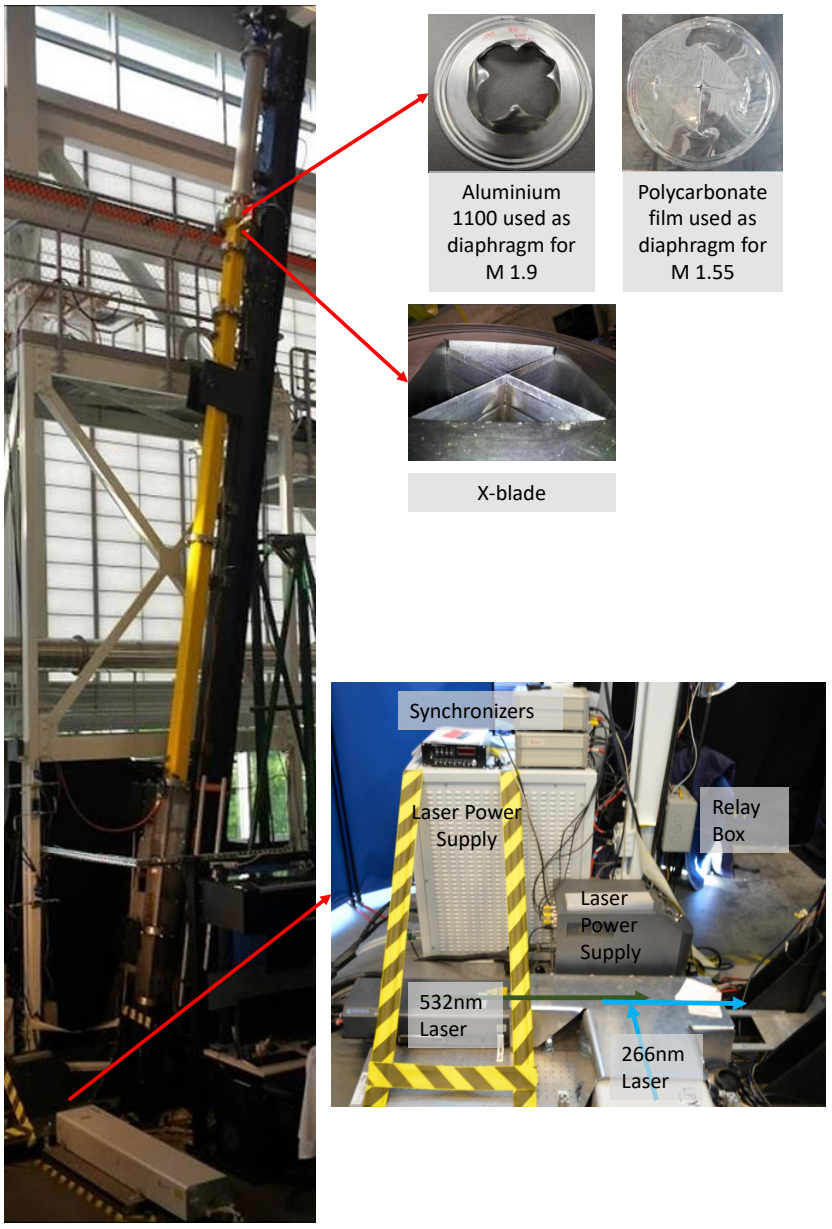

(a) Georgia Tech shock tube facility

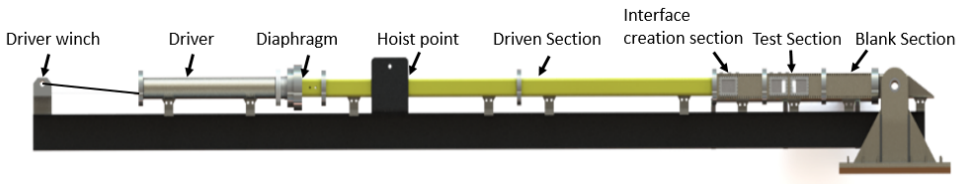

(b) Shock tube component diagram

Figure 2.1: (a) Left: Shock tube inclined at $80°$, Top right: Ruptured aluminum and polycarbonate film diaphragms which are used for $M \sim 1.9$ and $M \sim 1.55$, respectively, and X-blade, Bottom right: Equipment for imaging diagnostics to capture simultaneous PLIF/PIV images. (b) Labeled depiction of shock tube components.

diagnostic system while both transducers are used to determine the shock strength. The triggering mechanism utilized allows for the recording of the interface at a repeatable time and location after initial shock interaction. The use of these transducers also allows for the output of a temporal pressure trace which also contains the interface reflected shock.

Within the test section, the strength of the transmitted and reflected shocks and expansion waves are monitored by another pair of dynamic pressure transducers. This pair can be moved to any available window location within the test section. The pressure transducers are mounted flush to the inside shock tube wall so their presence does not disturb the traveling shock wave. Optical access can be attained at any of the test section modules through overlapping half-length windows or full-wall windows when needed. Full optical access is essential when recording the time series development from initial condition (IC) to the latest experimental time. This experimental duration is limited by the interaction of the expansion waves from the driver with the interface. It should be clarified that the experimental duration includes the interaction with weak expansion waves which originate at the interface upon reshock and then reflect off the end wall of the tube.

The test section has a modular design which allows creation of an interface at various distances from the end wall to control the time of reshock interaction. When the angle of the tube is varied, the modules are simply reconfigured to allow interface creation. In the present work, the interface between the two gases is created close to the top of the test section while the tube is at 80° relative to the ground.

2.2 Interface Creation and Characterization

One of the main goals of this work is to understand the role of the initial condition in shock-driven, variable-density flows. In order to achieve this goal, we have implemented two sets of initial conditions which vary in their modal composition. The first case is an inclined interface (tube angle of 80° relative to the ground) which is a predominantly single-mode interface. The predominantly single-mode (S) interface is created by flow

of light and heavy gases from the top of the driven section and the bottom of the test section, respectively. The gases form an interface that is parallel to the ground and they exit the test section via slots connected to a vacuum pump. Thus, the angle between the inclined interface and the incident shock wave is about 10° (Reilly *et al.*, 2015; McFarland *et al.*, 2014). It was determined that this method creates a relatively flat interface with a diffusion thickness $\approx$ 0.96 cm. For insight into the mathematical representation of the inclined interface, which is effectively half of a period of a triangular wave, Mikaelian (2016) suggested that the inclined interface can be closely represented by half of a cosine wave which has a Fourier coefficient carrying 81% of the Fourier expansion. The 'V' pattern can be Fourier expanded as

$$cos_2(x) = cos_4(x) = \frac{8}{\pi^2}\{cos(x) + \frac{cos(3x)}{3^2} + \frac{cos(5x)}{5^2} + \frac{cos(7x)}{7^2} + \frac{cos(9x)}{9^2} + ...\}. \quad (2.1)$$

The fundamental mode contains $(8/\pi^2)$ 81% of the Fourier expansion, and the remaining terms carry almost 19%. The multi-mode (M) interface is created by injecting light gas into the heavy gas just below the interface creation plane and by injecting heavy gas into the light gas just above the interface creation plane. The light gas then rises from its injection point in the heavy gas section while the heavy gas falls from its injection point in the light gas section to create a multi-mode interface between the two larger sections of gas. This configuration, combined with the suction of a vacuum pump at the interface outflow slots, creates a counter flow condition with a combination of shear and buoyancy instabilities along the interface. A sample multi-mode initial condition PLIF image corrected for variations in laser intensity and background noise effects is shown in Figures 2.2 (a) and 2.4 (a), where the intensity of the image concentration corresponds to the mole fraction of the light gas (white), and the multi-mode interface creation is described in Figures 2.2 and 2.3.

The initial condition characterization is done by taking 200 PLIF images of the multi-

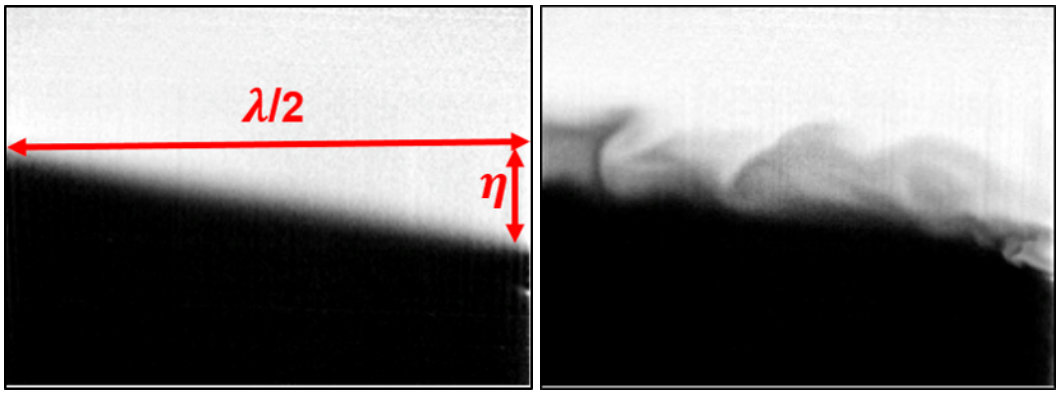

(a) Sample single-mode initial condition

(b) Sample multi-mode initial condition

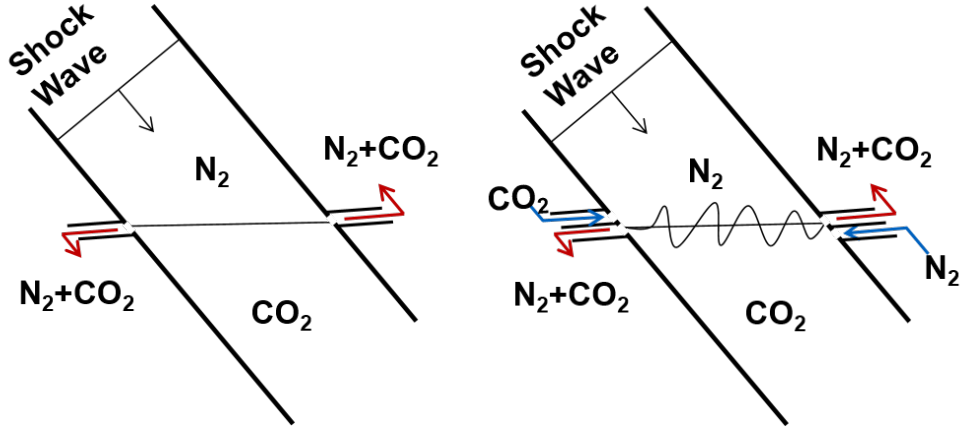

(c) Schematic of single-mode initial condition creation

(d) Schematic of multi-mode initial condition creation

Figure 2.2: Single- and multi-mode initial condition creation: (a,b) Sample corrected single- and multi-mode initial condition images where nitrogen is light and carbon dioxide is dark (c,d) Simplified schematics showing the general methods of interface creation. Red arrows indicate outflow of mixed gas, and blue arrows indicate inflow of pure gas. In the schematic, the angle of the interface is slightly exaggerated for clarity. In both depictions gravity acts normal to the interface. The actual inlets and outlets consist of small perforations to prevent disturbance of the shock.

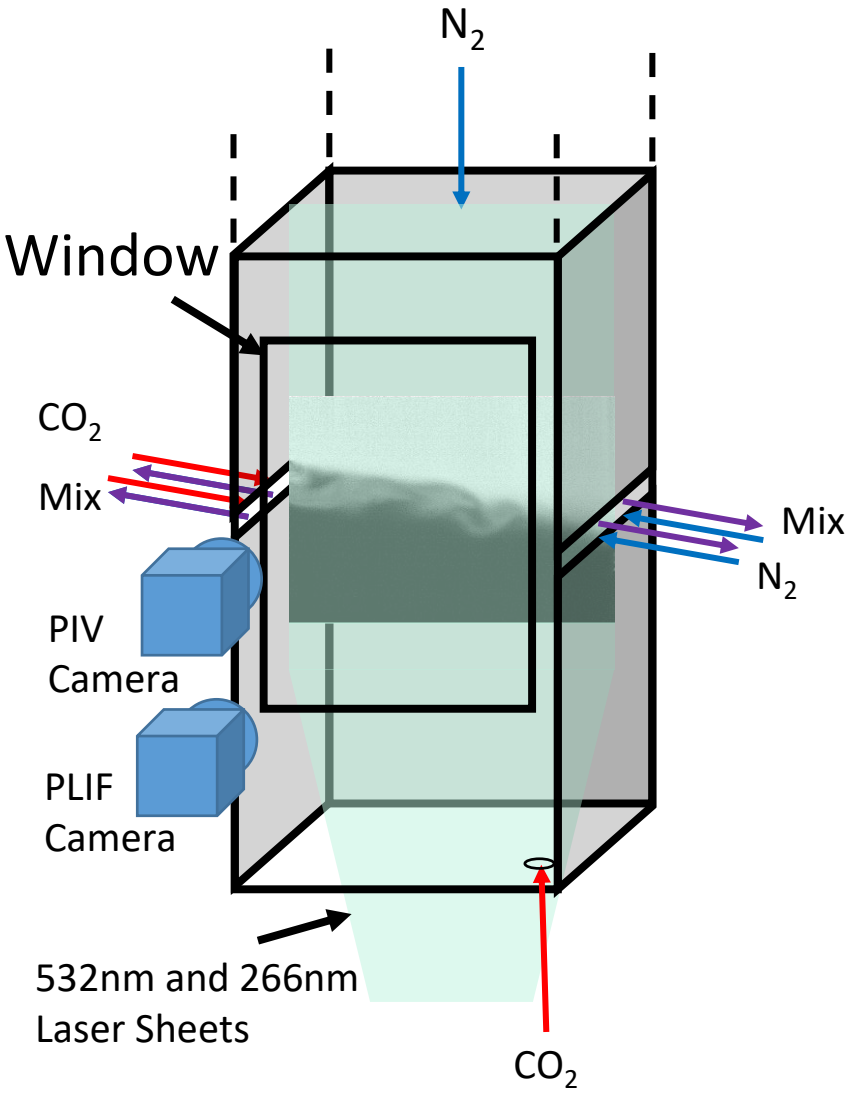

Figure 2.3: 3D diagram of multi-mode initial condition which shows the laser sheet, camera configuration and the window.

mode interface and then using energy spectra of density and Proper Orthogonal Decomposition (POD) to provide a statistical analysis of the interface.

Figures 2.4 (b) and (c) show the ensemble average and standard deviation, respectively, of the nitrogen mole fraction for 200 PLIF images. As seen in Figure 2.4 (c), the largest fluctuation occurred near the bottom surface (the left side of the shock tube) where the mole fraction standard deviation is 1.2%, which shows the repeatability of our initial condition. In order to isolate the effect of the secondary modes from the large wavelength inclined perturbation on the energy spectra, images of the inclined multi-mode interface are rotated 10°. One such rotated interface sample is shown in Figure 2.4 (d). In a method similar to Weber *et al.* (2014), The energy spectrum is calculated along the perturbed region within the concentration between 0.18 and 0.3 (small to mid-range scales), then averaged in the streamwise direction for each realization and then ensemble averaged for the total number of realizations. Figure 2.5 (a) shows the ensemble average of density energy spectra for an increasing number of interface images, and indicates that the spectrum converges after ≈20 images.

The ensemble average of energy spectra in the perturbed region for 100 images is shown in Figure 2.5 (b). Three ranges of different slopes can be distinguished from the analysis of the rotated image in Figure 2.5 (b). According to Figure 2.5 (b), the primary peak wavenumber is $k \approx 40$ m^{-1}, and the spectral range that has the highest energy ($k < 40$ m^{-1}) is related to the shock tube dimension. The spectra undergo a change in slope at $k \approx 200$ m^{-1}, highlighting an intermediate range from 40 m$^{-1} < k < 200$ m^{-1}. The scales in this range relate to shear and buoyancy effects in the initial condition. Finally, the smallest scales, which are related to the diffusion thickness, are seen in a third range ($k > 200$ m^{-1}), which has the steepest slope of the spectra. Rather than a fit to the data, the figure shows fiducials for the three ranges.

To compute the POD of the initial condition, the same set of 200 PLIF realizations used in the density energy spectra investigation were utilized. In POD, each mode represents a

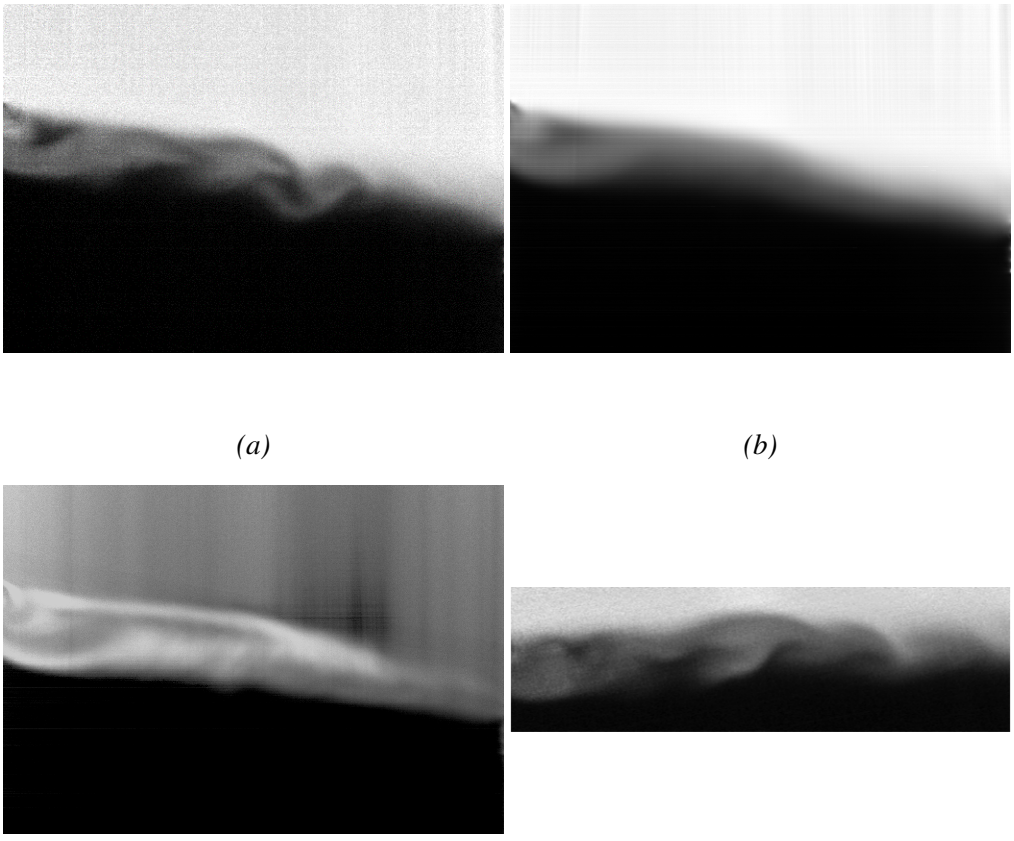

(a) *(b)*

(c) *(d)*

Figure 2.4: Initial condition characterization: (a) Sample multi-mode IC (image intensity corresponds to mole fraction of nitrogen). (b) Ensemble average of mole fraction for 200 multi-mode IC images. (c) Standard deviation of the same 200 images. (d) Multi-mode IC after 10° rotation with respect to the inclined shock tube (80°).

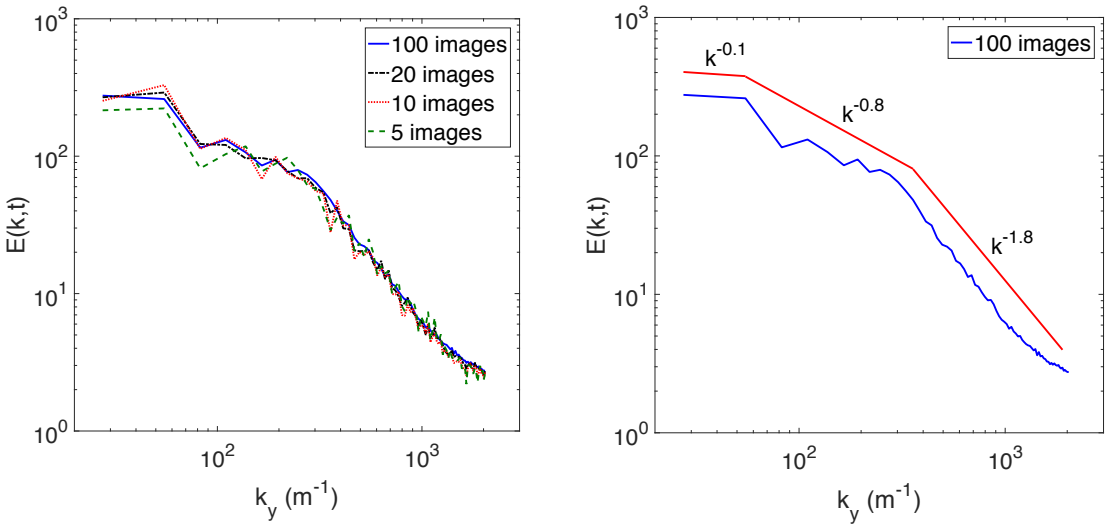

Figure 2.5: Initial condition characterization: (a) Average energy spectra for an increasing number of ensemble averaged images for the rotated IC. (b) Energy spectra calculated from a rotated IC in Figure 2.4 within a concentration between 0.18 and 0.3. Different slopes are shown by red lines.

coherent flow structure based on its reoccurrence in all images. Furthermore, to find the fraction of a particular mode, one must look at the associated eigenvalue (Berkooz, Holmes, and Lumley, 1993). In the POD analysis, mode 0 represents the ensemble average of the 200 density fields, as shown in Figure 2.6 (a). Additionally, when comparing Figure 2.6 (a) with Figure 2.4 (b), it can be shown that the images are similar and thus this indicates the accuracy of the POD code used (both of them show the ensemble average of flow fields). The modal fraction and cumulative fraction of modes are shown in Figure 2.6 (d). Figures 2.6 (b) and 2.6 (c), respectively, represent modes 1 and 2 of the decomposition containing 4.4% and 4.1% of the total concentration field, respectively. There is a strong similarity between the spatial modes 2 and 3, with similar sizes and positions of the flow structures which corresponds to additional scales from counter flow configuration. Figure 2.6 (d) shows that the first 18 modes contain 50% of the perturbations' concentration field, which suggests multi-mode perturbations are occurring on the interface. To further clarify this point, the modal fraction of concentration fields is shown in Figure 2.6 (e), which illustrates that the first 18 modes comprise a majority of the flow perturbations' kinetic energy. The

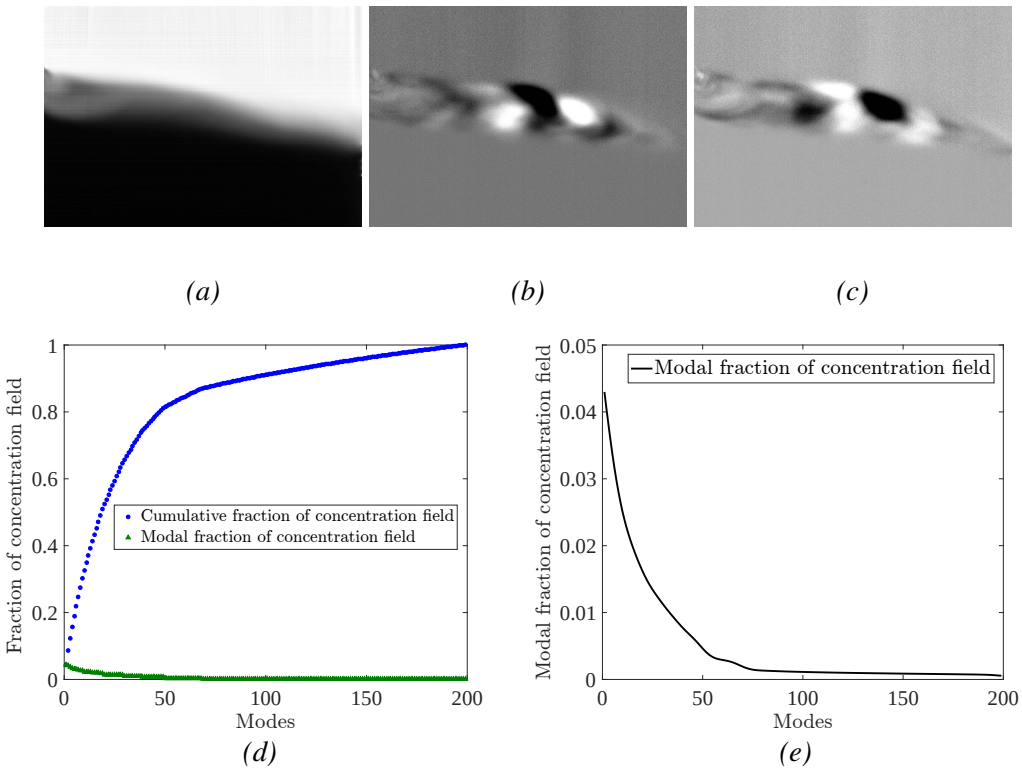

Figure 2.6: Dominant modes of the POD for 200 ensemble averaged multi-mode initial condition concentration fields, and their respective fraction of concentration field: a) Mode 0 (Ensemble average) b) Mode 1 (4.4% of total concentration field), c) Mode 2 (4.1% of total concentration field), d) The modal and cumulative fraction of concentration field e) Modal fraction of concentration field for all 200 modes.

connection between POD and energy spectra of density can be observed by considering the mid-range scales in modes 1 and 2 of the POD analysis which are $\approx$ 2-5 cm and are in good agreement with the scales of the intermediate range of energy spectra.

In addition to the POD of concentration fields, the POD of 200 realizations of kinetic energy which is calculated from PIV data is computed. The result of the POD of concentration and kinetic energy fields are compared. Figure 2.7 (a), (b) and (c) show the first three modes which contain 38%, 16% and 7% of total kinetic energy of the multi-mode interface. Mode 1 and mode 2 in the POD analysis of kinetic energy, indicate shear between light and heavy gases. They highlight kinetic energy in the light gas side and heavy gas side. The alternating behavior (positive and negative) in mode 3 and higher modes of the POD analysis indicates buoyancy contribution. According to the POD of kinetic energy,

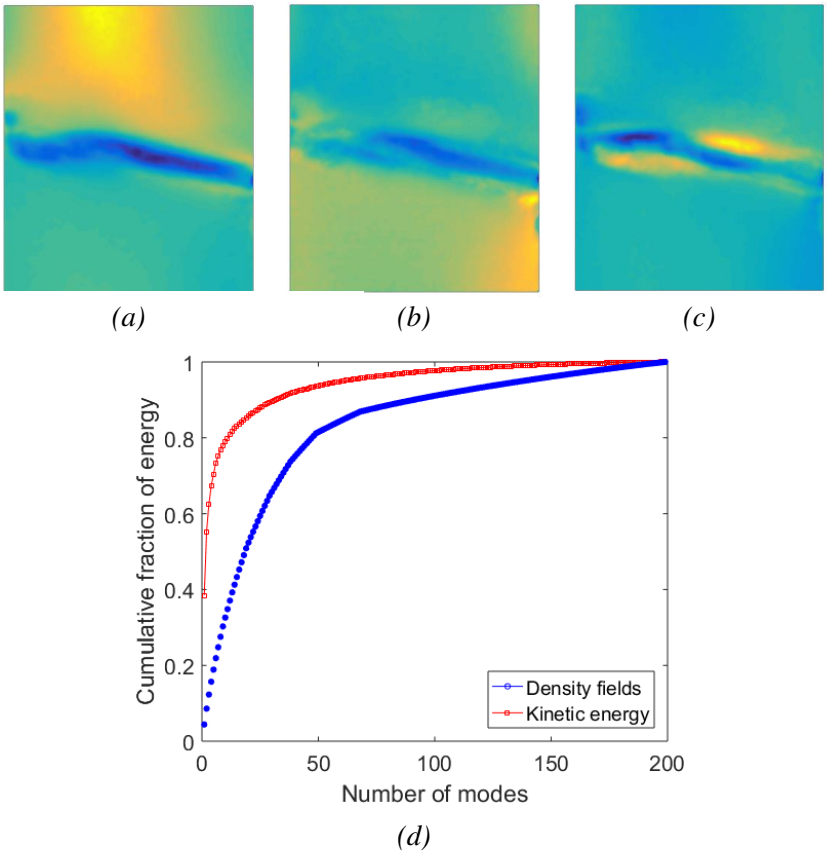

Figure 2.7: Dominant modes of the POD for 200 kinetic energy fields of multi-mode initial conditions and their cumulative fraction: a) Mode 1 (38% of total kinetic energy), b) Mode 2 (16% of total kinetic energy), c) Mode 3 (7% of total kinetic energy), d) A comparison of the cumulative fraction of kinetic energy and density (concentration) field

shear effects are more dominant than buoyancy effects. Also, the structures with shorter length scales are dominant in higher modes. Figure 2.7 (d) shows that the POD of kinetic energy converges faster than that of the concentration fields, where 11 modes are needed to reconstruct 80% of the total kinetic energy compared to 47 modes for a similar reconstruction of the concentration (density) field of initial condition. This can also be due to a resolution effect, where the vector spacing resolution (372 μm) is almost five times bigger than the resolution of PLIF images (72 μm).

Finally, in order to look at interface behavior along the out of plane dimension, a three dimensional reconstruction is performed. For this analysis, 20 PLIF images are taken at each of 9 locations evenly spaced within the range of 2 cm before and 2 cm behind the

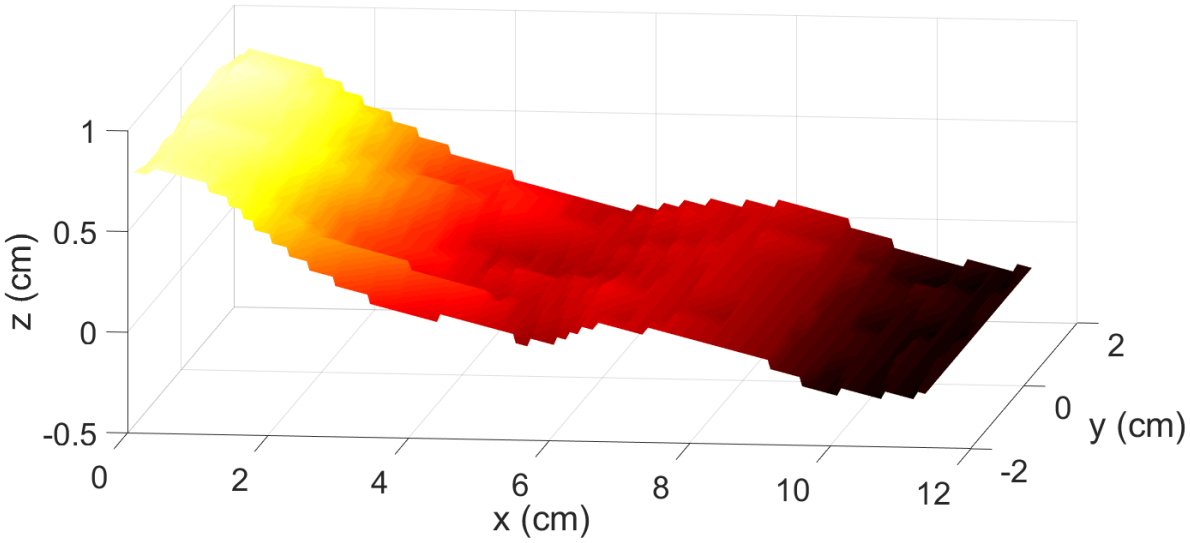

Figure 2.8: A 3D reconstruction of the interface based on interface location found using Canny edge detection method. The result for each location is based on an ensemble average of 20 PLIF images. 9 planes of realizations are spaced evenly spanning 4 cm of depth.

centered laser sheet. The maximum laser sheet angle is $\sim 4^{\circ}$ which results in a measurement error of less than 1%. The results for each location are first ensemble averaged over the 20 realizations, and then the interface is detected at each laser sheet location using the Canny edge detection method described in chapter 4. Therefore, Figure 2.8 reports these statistically averaged results to generate a characteristic interface profile in the out of plane direction. The statistical average perturbation appears uniform along the out of plane, third dimension.

2.3 Experimental Configuration and Imaging Diagnostics

For the current work, nitrogen is passed through an acetone bubbler, heated to a controlled saturation temperature, and then diluted with pure nitrogen at a controlled ratio. This mixture is used as the light gas, and carbon dioxide is used as the heavy gas. This results in an effective Atwood number ($A = \frac{\rho_2 - \rho_1}{\rho_2 + \rho_1} = 0.22$, where ρ_2 and ρ_1 are heavy and light gas densities). A separate stream of nitrogen was used as driving gas to pressurize and rupture the diaphragm. Two types of materials for diaphragms are used for different Mach

Table 2.1: Properties of gases for two different Mach number cases. i is after incident shock, r indicates after reshock and t is an indicator of transmitted shock. 1 and 2 indicate light and heavy gases respectively.

M_i	1.55	1.9
M_t	1.61	2.01
M_r	1.53	1.8
W_i (m/s)	548	671
W_t (m/s)	492	663
V_0 (m/s)	257	392
Acetone(% Vol.)	8.3	8.3
ρ_1 (kg/m^3)	1.16	1.16
ρ_2 (kg/m^3)	1.84	1.84
ρ_1^i (kg/m^3)	2.45	3.27
ρ_2^i (kg/m^3)	3.97	5.38
ρ_1^r (kg/m^3)	4.39	7.12
ρ_2^r (kg/m^3)	7.37	12.22
T_1^i (K)	403	477
T_2^i (K)	386	450
T_1^r (K)	510	671
T_2^r (K)	471	606
A	0.22	0.22
A^i	0.23	0.24
A^r	0.25	0.26

numbers: Aluminum 1100 sheet with a thickness of 0.05" for $M \sim 1.9$, and polycarbonate film with a thickness of 0.03" for $M \sim 1.55$. The light gas is bubbled through acetone and then diluted to serve as a fluorescent marker to measure the concentration of the light gas, and thus the density. A schematic detailing the complete experimental configuration used for the present studies is shown in Figure 2.9. The tube in this figure is at 80 degrees with respect to the horizon, and the schematic shows lasers, plumbing, the setups for the acetone bubbler and seeding, and then their connection to mixing chambers and finally to the tube. Additionally, a summary of important gas properties (including post-shock interface velocities, wave speeds, temperatures, densities, and Atwood numbers) calculated from 1D gas dynamics for the two Mach number cases considered in the present studies is given in Table 2.1.

The diaphragm is pinched between the driver and driven sections. A collar slips over the

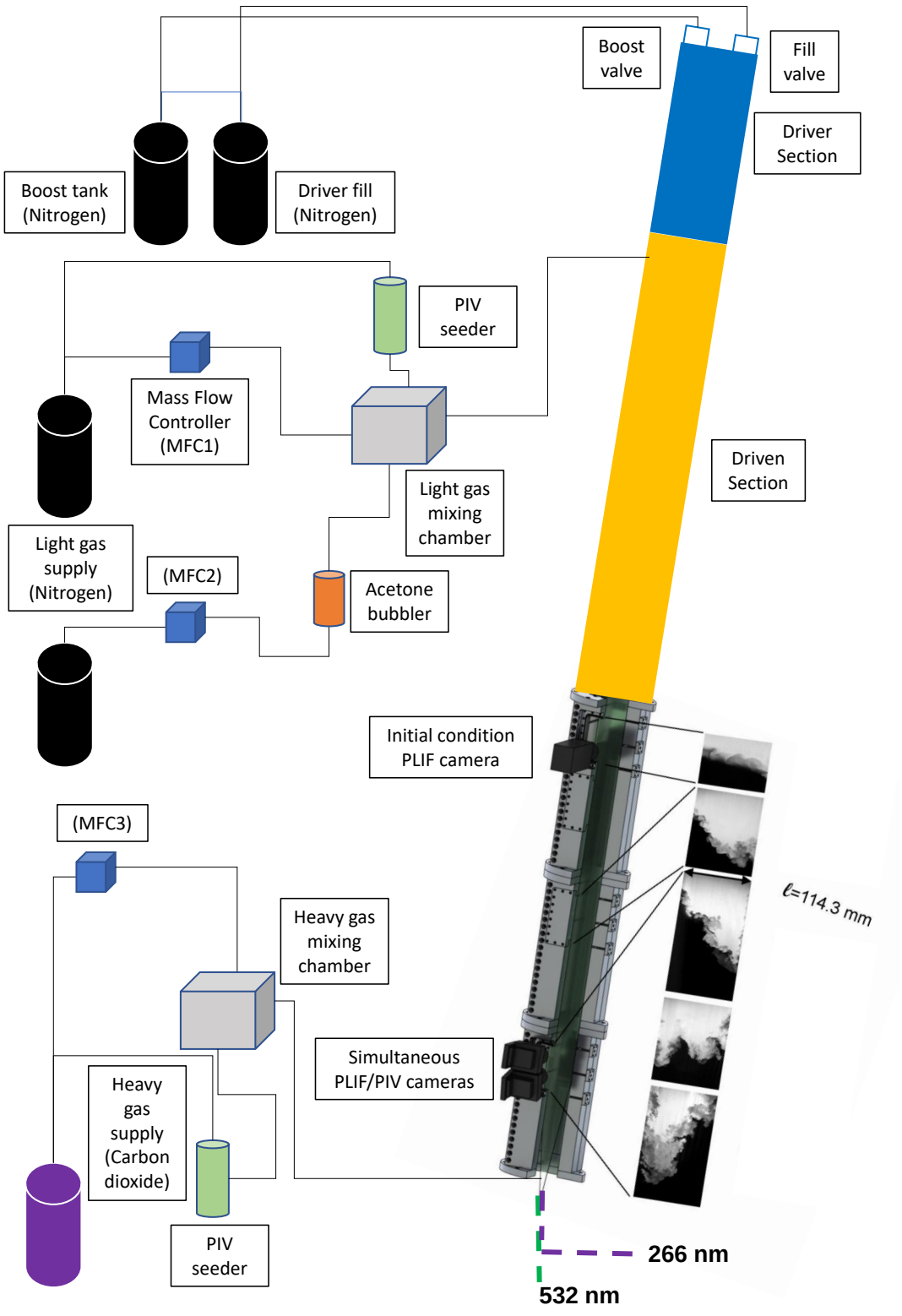

Figure 2.9: Experimental configuration showing cameras, lasers, plumbing, particle seeding setups and connection to mixing chambers used for simultaneous PLIF and PIV experiments.

flanges of the driver and driven sections to hold the diaphragm in place. The driver section and collar are changed and modified based on the experimental campaign. Previously, the collar was lifted and removed by hand, in order to replace the diaphragm between different experimental runs (Reilly *et al.*, 2015; McFarland *et al.*, 2014). However, since the collar weighs on the order of 30 lbs., to increase the safety and also to run experiments faster and increase productivity, the previous collar has been modified. In the modified design shown in Figure 2.10, the two halves of the collar are connected by hinges to a plate which is mounted to the shock tube's I-beam support structure. In this way, after each run, the collar can be opened and closed without removal, which is safer and faster.

In order to have adequate experimental time after reshock, before expansion fans hit the interface in the higher Mach and higher atwood number cases, a new tube for the driver was designed and manufactured. This issue will be explained in detail using $x - T$ diagrams. The new driver shown in Figure 2.11, is 2 meters in length; 0.5 m longer than the previous driver. It has an outer diameter of 7.25" and inner diameter of 6.25" and is made of A513 type 5 DOM carbon steel.

To investigate the shock induced mixing between the two gases, a two-camera system was used to perform simultaneous PIV and PLIF measurements over an overlapping field of view. The simultaneous measurements were performed by viewing the mixing layer from the same side of the laser plane, which required tilting one of the cameras. It has been verified that one can still obtain a strong PLIF signal even when the camera is tilted and that the perspective calibration preserves the information of the scalar field. A Scheimpflug mount was used with the PLIF camera in order to focus on the off-axis laser plane which is shown in Figure 2.12. This was corrected using calibration images of a dual-plane calibration target and a de-warping algorithm available with Insight 4G^{TM}. The details of the correction are explained in chapter 3.

PLIF measurements are performed by seeding only the light gas with acetone. In the current study, a Litron laser capable of 120 mJ per pulse at 266 nm is used to illumi-

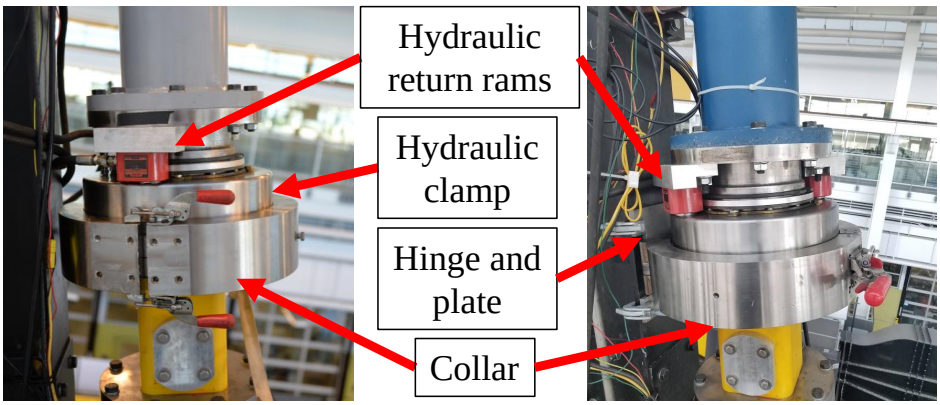

Previous collar & Hydraulic diaphragm loader

Modified collar & Hydraulic diaphragm loader

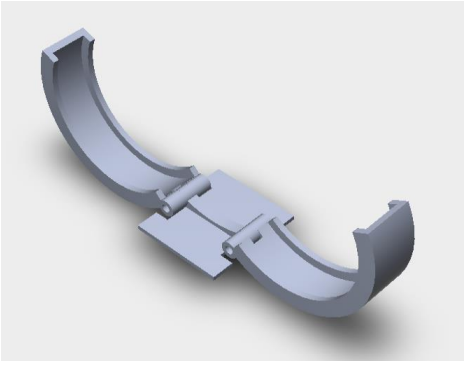

Modified collar model

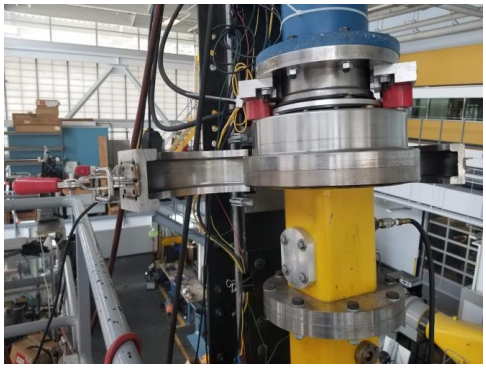

Opened modified collar

Figure 2.10: Modified collar and hydraulic diaphragm loader assembly.

Model of new driver with a length of 2 m

New driver after painting

New driver mounted on the tube

Figure 2.11: The new tube for the driver section with a length of 2 m (80”), to run the high Mach ($M \sim 1.9$) experimental campaign, mounted on the shock tube.

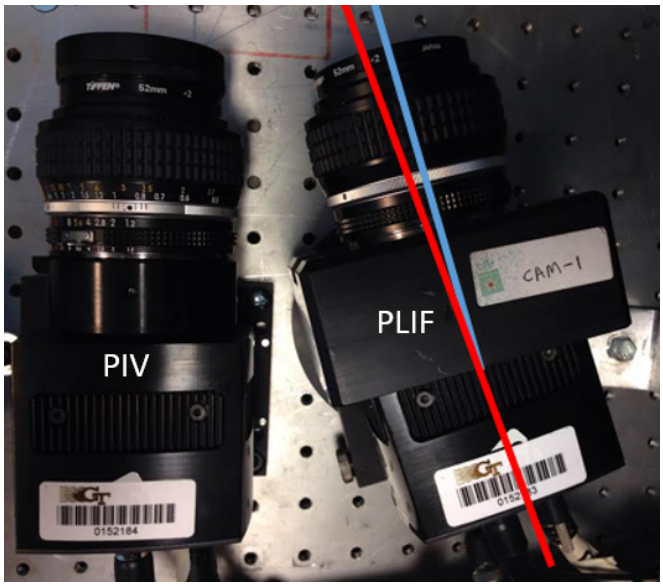

Figure 2.12: 29 MP CCD cameras used for simultaneous PIV/PLIF measurements. The PLIF camera utilizes a scheimpflug mount. The centerline of the CCD is shown in red, and that of the lens is shown in blue.

nate the seeded gas from below, causing the acetone vapor to fluoresce. Pure nitrogen is passed through a bubbler held at constant temperature to ensure consistent saturation concentration. The saturated nitrogen is mixed in a large mixing volume with pure nitrogen to achieve a constant concentration of acetone which yields an Atwood number of 0.22 (pure nitrogen/carbon dioxide yields $A = 0.23$). The fluorescence emission is captured using an un-intensified TSI PowerView 29 MP CCD camera equipped with a 50 mm f/1.2 Nikon lens with an additional 2+ close up lens. In order to capture only fluorescence emitted by acetone, the camera is equipped with a notch filter to remove the 532 nm wavelength light due to the PIV signal. The 2 by 2 binning is used to increase the signal to noise ratio, yielding a spatial resolution of 73 μm/pixel.

For PIV measurements, both gases were seeded with titanium dioxide particles with an average particle size of 0.3–1 microns. Based on the relaxation time of the particles in either gas, they should fall no more than 1% of the current pixel resolution upon shock acceleration, which is much less than the 10% subpixel accuracy achieved by the Gaussian subpixel interpolation method (McFarland *et al.*, 2014). The seeded particles were illuminated using a dual-cavity New Wave Research Gemini PIV laser at 200 mJ and a wavelength of 532 nm. The laser beam is diverged into a sheet just before entering the bottom of the tube. The location of the beam waist was adjusted for each image acquisition location, and through a knife-edging technique it was estimated that the laser light sheet thickness at each location was $\approx$0.65$\pm$0.05 mm. Acquisition was performed using a TSI PowerView 29-MP CCD camera with a 532 nm bandpass filter and a 2+ close up lens. The laser beams are combined using beam-combining optics, passed through a spherical lens to produce a beam waist at the imaging location, then through a sheet-generating cylindrical lens, and directed into the shock tube through a quartz window at the bottom of the shock tube. The sheet is aligned normal to the shock propagation and slicing the inclined interface. The laser sheet thickness was selected based on the camera depth of field (Stanislas

and Monnier, 1997).

$$\delta z \simeq \pm 2.4 \left(\frac{1 - Mag}{Mag} \right)^2 \left(\frac{f}{2\sigma} \right)^2 \lambda \tag{2.2}$$

In the present work, $f\text{-}number = 4, Mag \backsim 0.2, \lambda = 532nm$, so $\delta z \simeq \pm 0.33$. The illumination of particles outside the depth of field is minimized by keeping the laser sheet thickness approximately equal to the depth of filed. Because out-of-plane gradients are present, especially after reshock, the laser sheet thickness and interrogation window are also required to be small in order to mitigate error in the small scales due to the volume-averaging effects associated with PIV (Lavoie *et al.*, 2007).

The detailed evolution of the velocity and density fields as the interface translates with time is captured from an ensemble of experiments at the various interface locations by controlling the delay between shock detection and the PIV-PLIF acquisition. The location of images are schematically shown in Figure 2.9. A calibration image is taken with both cameras each time the cameras are moved so as to register the PIV and PLIF measurements to each other.

Two sets of measurements are performed for each Mach 1.55 and 1.9. First, an initial sweep through experimental times of only PLIF measurements is done to characterize the instability growth for both the single- (S) and multi-mode (M) interface conditions. A second, more detailed (and larger ensemble) measurement set follows, using simultaneous PIV and PLIF techniques at two instances after the incident shock, but prior to reshock, and two times post-reshock. The number of realizations selected for each experimental time (t), and associated dimensionless time (τ) are given in Table 2.2. Dimensionless times are calculated using

$$\tau_i = k\dot{h}_0(t - t^*). \tag{2.3}$$

The method is described in McFarland, Greenough, and Ranjan (2011) and McFarland,

Greenough, and Ranjan (2014). After the incident shock, $\dot{h}_0$ is the initial growth rate which is measured based on the 5%-95% method of computing the mixing width, t is the experimental time, and $t^* = \frac{\lambda}{2w_i \tan\theta}$ is the time required for the shock wave to traverse the inclined interface. $k = 2\pi/\lambda$ is wave number, w_i and w_r are the incident shock and reshock speeds. After reshock, a similar equation is used,

$$\tau_r = k\dot{h}_0'(t - t'^*), \tag{2.4}$$

where $\dot{h}_0'$ m/s is the mixing width growth rate after reshock, $t'^* = \frac{h_{(pre-reshock)}}{w_r}$ the time it takes for the reshock wave to traverse the interface immediately before reshock, $t = t_{exp} - t_{(reshock-interface-interaction)}$, where t_{exp} is the actual experimental time. In order to have a continuous non-dimensional time (τ), τ_r (non-dimensional time after reshock) is added to the latest τ_i (non-dimensional time after incident shock). The latest non-dimensional time after incident shock (τ_i) is approximately 2.4 for both low and high Mach. Therefore, $\tau = \tau_i$ before reshock, and $\tau = \tau_r + 2.4$ after reshock. Table 2.2 summarizes the list of experimental times and ensemble sizes used for the current work for single and multi-mode initial conditions. The observations from the time-swept evolution experiments and those from the more detailed experiments are discussed in chapter 4.

2.4 Mach Number Variability

To study the effects of Mach number on RMI evolution, experiments are performed at two different Mach numbers. The Mach number can be changed by changing the driver gas pressure or species. Mach number can be computed using

$$M = \sqrt{\frac{\gamma_1 - 1 + (\gamma_1 + 1)(P_2/P_1)}{2\gamma_1}}, \tag{2.5}$$

where γ is the ratio of specific heats, and P_1 and P_2 are the pressures ahead of and behind

Table 2.2: Summary of experiments

Label	Experimental time	Nondimensional time	Single-mode Ensemble	Multi-mode Ensemble
$M \sim 1.55$				
S1.21, M1.21	2.64 ms	1.21	5	5
S2.34, M2.34	5 ms	2.34	6	30
S3.06, M3.06	6.4 ms	3.06	33	30
S4.6, M4.6	9 ms	4.6	31	32
$M \sim 1.9$				
S1.18, M1.18	2 ms	1.18	10	20
S2.27, M2.27	3.75 ms	2.27	20	34
S3.05, M3.05	4.6 ms	3.05	30	32
S4.35, M4.35	6 ms	4.35	32	34

the shock wave. This equation can be solved in terms of the pressure ratio

$$\frac{P_2}{P_1} = \frac{2\gamma_1 M^2 - \gamma_1 + 1}{\gamma_1 + 1}. \tag{2.6}$$

The required driver pressure for a given Mach number experiment can then be computed using (Anderson Jr, 2006):

$$P_4 = P_2 \left[1 - \frac{(\gamma_4 - 1)(a_1/a_4)(P_2/P_1 - 1)}{\sqrt{2\gamma_1[(\gamma_1 - 1) + (\gamma_1 + 1)(P_2/P_1)]}} \right]^{\frac{2\gamma_4}{\gamma_4 - 1}}, \tag{2.7}$$

where a_1 and a_4 are the speed of sound in the gas in the driven and driver section, respectively, which can be calculated as

$$a = \sqrt{\gamma RT/m}. \tag{2.8}$$

Here T is temperature, m is the molecular mass, and $R = 8.314$ J/(mol*K) is the gas constant, and in these equations, state 1 and 2 are ahead and behind of shock wave, and state 4 is related to driver properties. In the current work, nitrogen is used as the driver gas

for both Mach numbers. Experimentally, the Mach numbers are limited to the materials which can be used for diaphragm and shock tube capabilities. It was found experimentally that 107-110 psi and 330-340 psi are the driver pressures which generate $M \sim 1.55$ and $M \sim 1.9$ respectively. These values are very consistent with the theoretical required driver pressures computed from the equations above for these Mach numbers, which indicates that there are minimal mechanical/pressure losses between the driver and driven sections, and in the connections along the tube. The experiment duration is limited by interference from the initial expansion fan. An $x - t$ diagram is constructed to choose acceptable experimental times before the expansion fan reaches the test section. Figure 2.13 shows $x - t$ (position versus time) diagrams with shock waves, reflected shock waves, and expansion fans, for $M \sim 1.55$ and $M \sim 1.9$ generated using code developed at the University of Wisconsin and altered to the specifications of the experimental conditions in the current study. It is important to note that the driver length was increased from 1.5 m in the $M \sim 1.55$ case to 2 m for the $M \sim 1.9$ case.

To measure Mach number experimentally and quantify the variation in Mach numbers between different runs, dynamic pressure transducers are located along the tube. In addition, to check the rupture pressure of the diaphragm, one pressure transducer is located in the driver section. All of these data are recorded for each experimental run. Figure 2.14 shows traces from each of these 6 pressure transducers. PT1 and PT2 are mounted above the interface, 0.1 meter apart, and are used to calculate Mach number. RT1 and RT2 are mounted close to the endwall, and can be used to calculate reshock Mach number. Finally, there is another pressure transducer at the bottom wall (endwall) of tube which records one jump when the shock hits the bottom wall (endwall) followed by a gradual decrease. The Mach number is calculated using

$$M = \frac{\Delta x / (t_{PT_2^{jump}} - t_{PT_1^{jump}})}{\sqrt{\gamma R T}} \tag{2.9}$$

where Δx is 0.1, and T is recorded using thermocouples in the driven and driver sections.

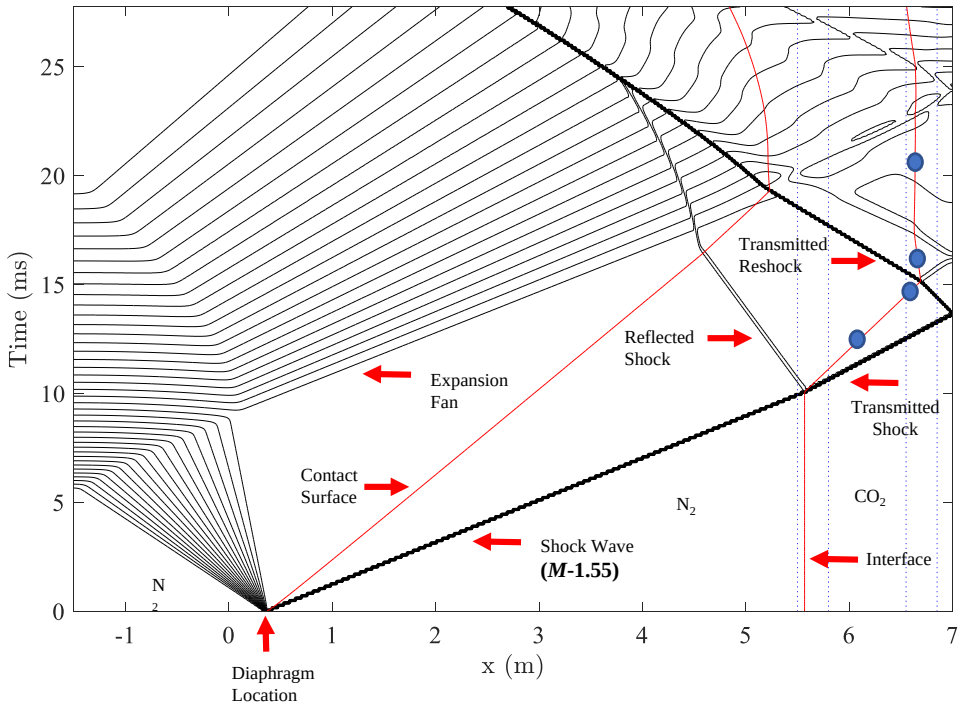

(a)

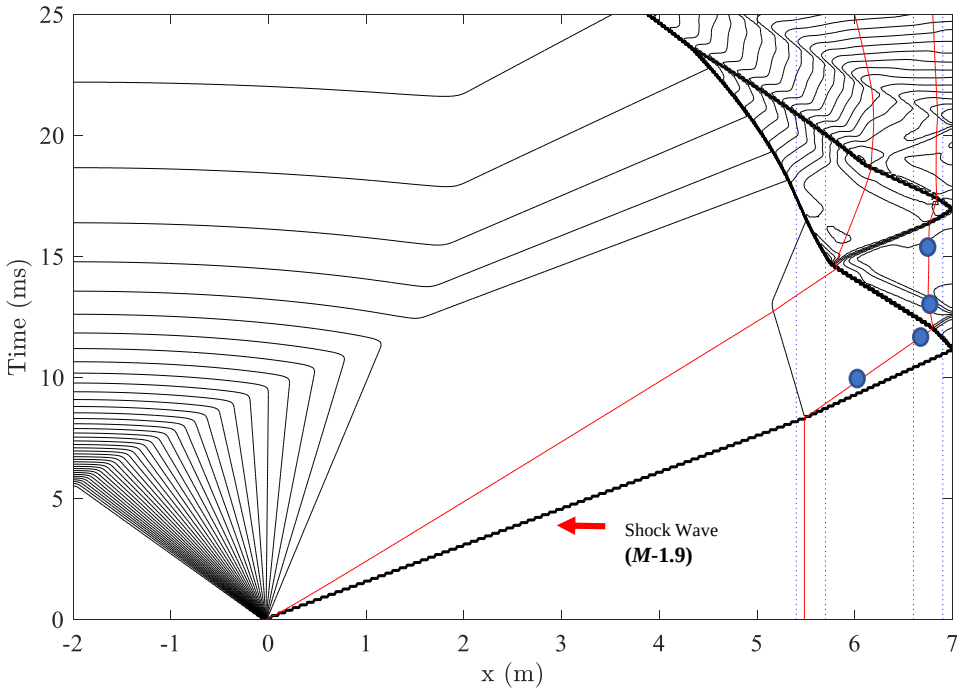

(b)

Figure 2.13: $x-t$ diagrams for the (a) $M \sim 1.55$ and (b) $M \sim 1.9$ experiments. Different waves, interface and diaphragm location are shown in the figure. Blue markers indicate times chosen to collect data.

t_{PTjump} is the time of the first jump in the data which corresponds to the shock interaction with pressure transducers. The gradual decrease in pressure corresponds to the times that the expansion fan passes the pressure transducer. These measurements are in good agreement with those predicted by the $x - t$ diagram. The rupture pressure of the diaphragm also can be calculated using the data which is shown in Figure 2.14 (a).

Finally, run to run variations in Mach number and driver pressure when the diaphragm ruptures are calculated based on data extracted from experiments that can be used for data extraction. Figure 2.15 shows the Mach number and rupture pressure in different experiments and the average value. Since Mach number is calculated based on Δt between pressure transducers, it is limited to the resolution (200 kHz), and the difference between variations are constant. However, although the resolution is a limiting factor, the Mach number is pretty consistent between different experiments. The standard deviation of Mach numbers at $M \sim 1.9$ and $M \sim 1.55$ are 0.0285 and 0.0211. The standard error is also calculated using

$$stderr = \frac{std(data)}{\sqrt{N(data)}} \tag{2.10}$$

where $N(data)$ is the number of that specific data. The average Mach numbers are 1.5676 and 1.9113, and the standard errors ($stderr$) are 0.0016 and 0.002 for $M \sim 1.55$ and $M \sim 1.9$, respectively. The average of break pressures are 341.86 and 108.14, the standard deviation of break pressures are 10.79 and 1.45, and the standard errors ($stderr$) are 0.7428 and 0.1074 for $M \sim 1.9$ and $M \sim 1.55$, respectively.

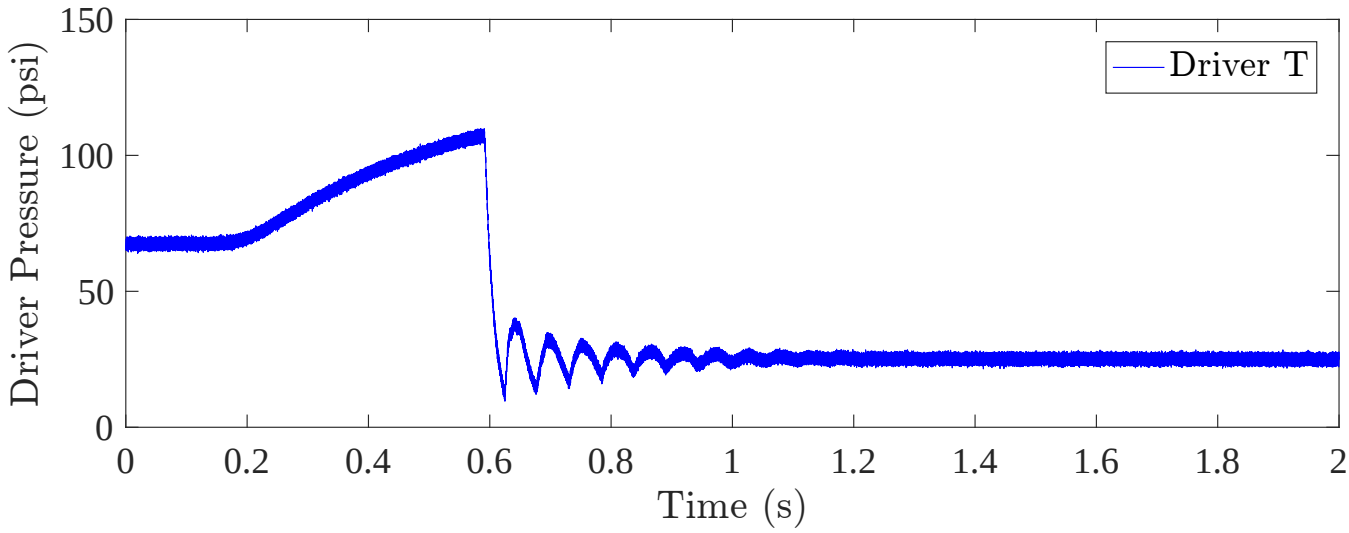

(a)

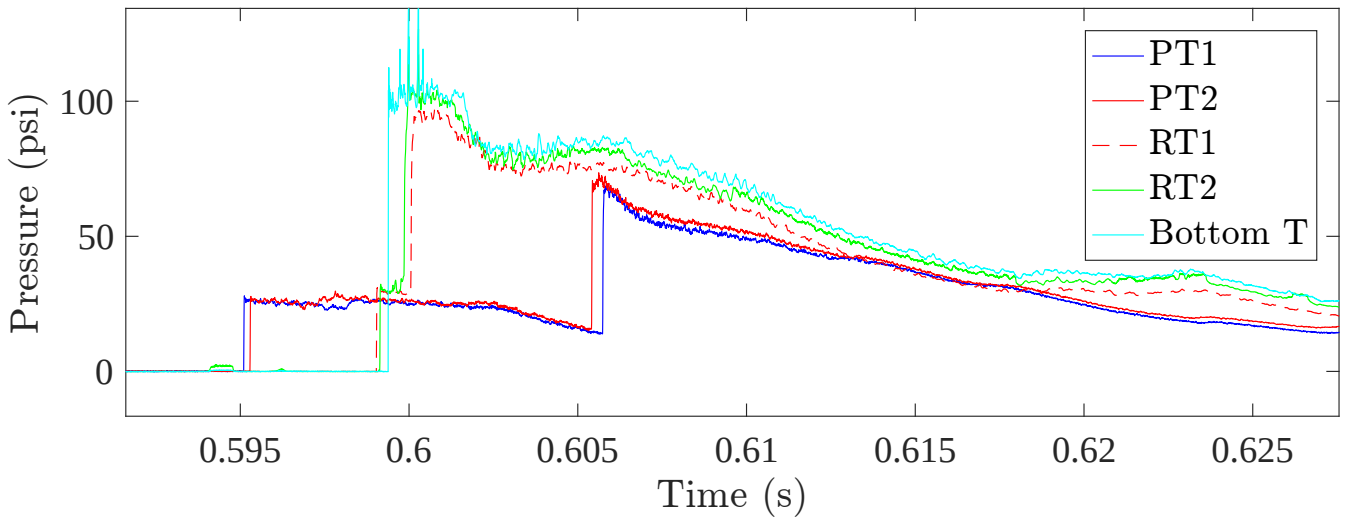

(b)

Figure 2.14: Pressure recorded by transducers during an experiment at Mach 1.55, (a) above the interface, near the wall (endwall) and on the bottom wall (endwall), and (b) driver pressure transducer.

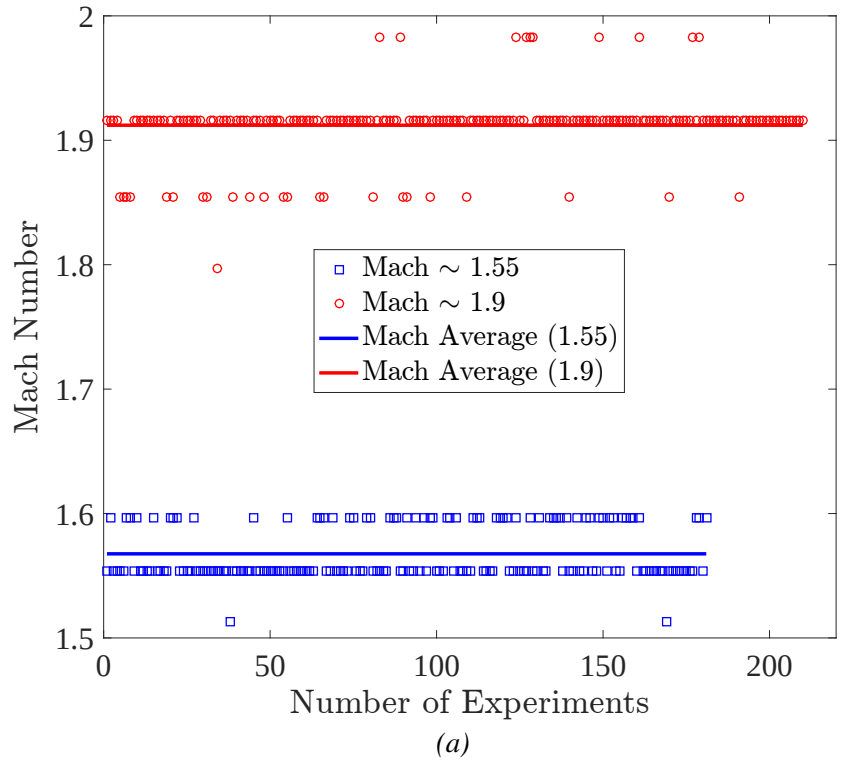

(a)

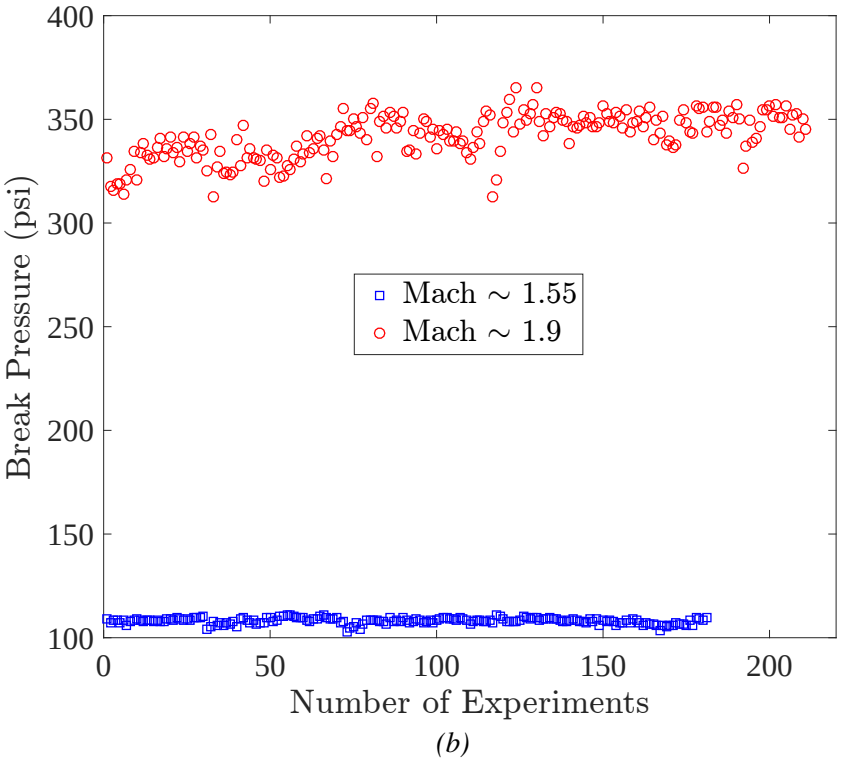

(b)

Figure 2.15: Experiment Mach number consistency. (a) Mach number, and (b) break pressure. Values are computed using pressure transducer data.

CHAPTER 3

DATA PROCESSING AND UNCERTAINTY ANALYSIS

3.1 Quantitative PLIF Processing

The PLIF image correction is based off of Weber *et al.* (2012) and Weber *et al.* (2014). However, the summary of different steps with some examples from this work are included in this chapter. There are several steps associated with the processing of the image, to correct for the variation in laser-intensity variations, attenuation and laser striations. As mentioned in the previous chapter, in order to capture the same field of view and maintain resolution, it is necessary that at least one of the cameras be angled. It was found that if a configuration is chosen such that the PIV camera was angled in relation to the laser sheet using a scheimpflug mount (with the PLIF camera remaining perpendicular) the velocity statistics, especially vorticity, yielded a high error due to out-of-plane motion which can not be distinguished from in-plane-motion using only one offset PIV camera. A comparison of the resulting density profiles from the PLIF camera in the angled and the perpendicular orientation resulted in difference of less than 2%. For this reason, the PLIF camera is mounted with a perspective view of the laser sheet, while the PIV camera views normal to it. This requires additional correction for this perspective by dewarping the PLIF images. The image de-warping is provided in Insight 4G^{TM}, where the calibration plate is used to remove the perspective distortion in images. The next step is to subtract the background image (signal) without any acetone from each raw PLIF image. Subsequently, the average intensity of a region on the heavy gas side (region without acetone) is subtracted from each image, in order to ensure that the average intensity of the heavy gas side is equal to zero (Figure 3.1).

The PLIF image processing is finished by correcting for laser intensity variations, stri-

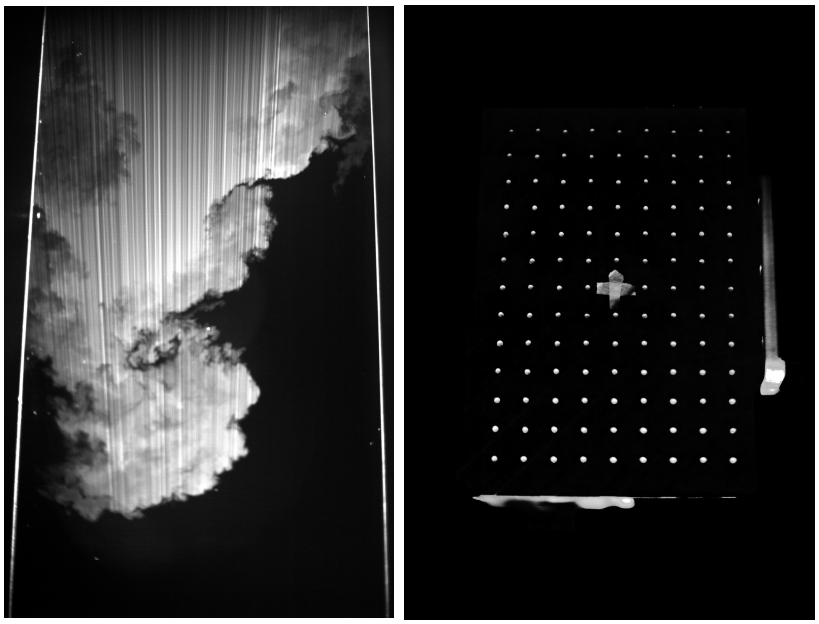

(a) Raw PLIF Image

(b) Calibration plate image

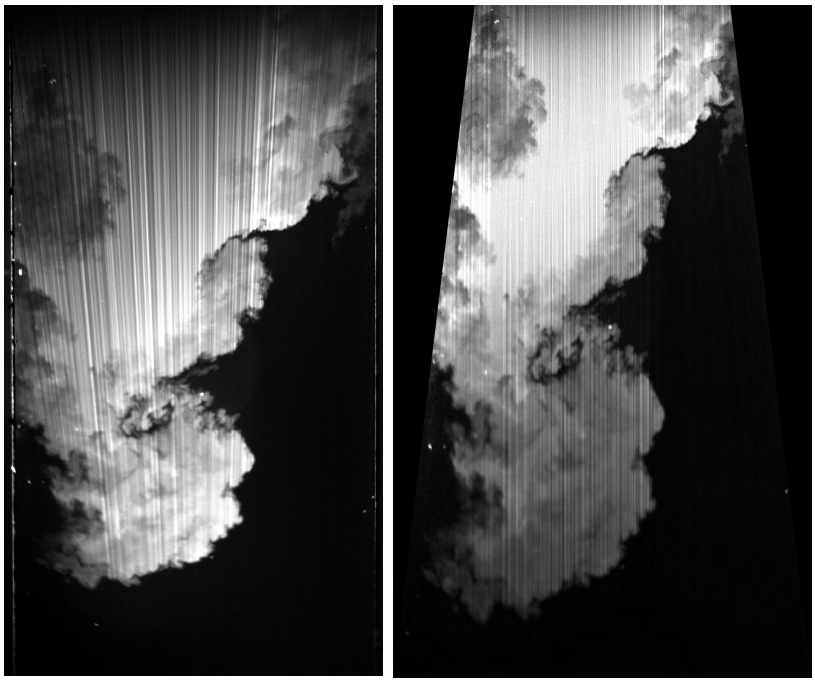

(c) Dewarped image

(d) Divergence and Beer–Lambert corrected image

Figure 3.1: (a) A sample PLIF image at latest time after reshock for $M \sim 1.55$. (b) Image of the two-plane calibration plate which is used to correct for lens and perspective effects and to align the PLIF image to the PIV vector field. (c) PLIF image after background subtraction, and dewarping is performed to correct lens and perspective effects.(d) PLIF image after correction for decrease in intensity at radial locations farther from the cylindrical lens due to divergence and for Beer–Lambert attenuation due to absorption.

ations, and Beer's law attenuation. The first step, before correcting for image intensity, is to reshape the PLIF image to correct for the divergence of the laser sheet, caused by the plano-concave lens. The image intensity is transformed to straighten the laser striations using

$$I_{trans} = I\frac{y_{int} - 1}{y_{int} - y} \tag{3.1}$$

where I_{trans} is the intensity of the straightened image, I is the intensity of de-warped image, y is the vertical location of each row of the image relative to the top of the image, and y_{int} is the vertical location of plano-concave cylindrical lens relative to the top of image ($y = 1$ is the top row of the image intensity) (Weber *et al.*, 2012; Weber *et al.*, 2014; Weber, 2012). Before this step, in order to maintain the original resolution of image, the original image is resized by a factor of $\frac{1}{1-(\Delta x_L + \Delta x_R)}$, where Δx_L and Δx_R are the distances from left and right side of the top row of the original image.

The next step is to correct intensity differences in the image due to attenuation. The pixel intensity which is recorded by the CCD camera can be computed using

$$I = gC_0\zeta J, \tag{3.2}$$

where g is the collection efficiency of camera, C_0 is the pure light gas concentration, $\zeta = C/C_0$ is the normalized concentration in distance s along the light ray, and J is the pixel intensity along the light ray. This equation should be implemented in the differential form of Beer-Lambert law which is

$$\frac{dJ}{ds} = -\varepsilon C_0\zeta I, \tag{3.3}$$

when correcting the intensity of PLIF images. ε is the attenuation coefficient. Implement-

ing Equation 3.2 into Equation 3.3 and integrating yields

$$\frac{I_2}{gC_0\zeta_2} - \frac{I_1}{gC_0\zeta_1} = -\varepsilon/g \int_1^2 Ids, \tag{3.4}$$

where state 1 is a reference profile chosen in the pure light gas region where $C = C_0$ and therefore $\zeta = 1$, and state 2 is all other points in the image. Finally, Equation 3.4 can be rewritten to calculate concentration in the whole field using

$$\zeta = \frac{I(x,y)}{I_0(x) - \varepsilon C_0 \int_1^y I(x,y)dy}. \tag{3.5}$$

Since the reference profile is chosen in the pure light gas region, to find intensity of reference profile region I_0, Equation 3.4 can be used which yields

$$I_0(x) - I(x,y) = -\varepsilon/C_0 \int_1^y I(x,y)dy, \tag{3.6}$$

and since the concentration in the pure region should be constant along the reference profile, I_0 can be computed using

$$I_0(x) = (\overline{I(x,y)e^{-\varepsilon/C_0 y}})_y. \tag{3.7}$$

The example of PLIF image corrected for the decrease in the intensity due to radial divergence and attenuation using Beer–Lambert law is shown in Figure 3.1 (d).

The last step is to remove laser striations by notch filtering the spectrum in which index of refraction artifacts appear in the attenuated images. First, the image is zero padded to create a periodic square array of intensities. Then, to compute the 2D Fourier transform, the image is mirrored on all 4 sides to create a 3×3 array which highlights the vertical striations in $k_y = 0$. The spectrum is filtered by replacing wave numbers along horizontal bands with the created mask by multiplying the mask with the FFT magnitude of image. The size of the created mask is computed similar to that explained in appendix A.3 of PhD thesis written

by Weber (2012). Finally, the corrected image is obtained by taking the inverse Fourier transform of the corrected spectrum, cropping additional mirrored portions of the image, transforming the image to its original size and removing black regions. Different steps of the notch-filtering method, and a final image is shown in Figure 3.2. The final resolution of PLIF images is 72 μm/pix and 68 μm/pix for $M \sim 1.55$ and $M \sim 1.9$, respectively.

3.2 PIV Processing

The first step to produce velocity field is similar to PLIF processing which is de-warping raw PIV images using a calibration plate image. It is necessary to capture calibration plate images using both PLIF and PIV cameras with identical plate location to register density and velocity fields accurately. For PIV processing, a combination of grid methodologies are used, a Rectangular Grid engine (pre-reshock) and a recursive Nyquist grid (post-reshock). For the pre-reshock cases, a Rectangular Grid engine is used to enable more control of the grid settings. In addition, in the pre-reshock case, due to the high mean velocity of the flow, an offset of 20 pixels was used to more accurately capture the velocity fluctuations in the moving frame. The image pairs were processed with Insight 4G^{TM} software using a 24$\times$24 pixel final spot size with 50% overlap. This final spot size is the smallest window processing size that did not produce more than $\sim$5% "bad" vectors in the whole PIV field. In PIV post-processing, smoothing and interpolation were used. Vectors that did not pass a universal median test over a 3$\times$3 neighborhood were replaced by secondary correlation peaks. In order to remove the effect of the boundary layers, a mask is used in processing and they are not included in the results, which reduced the interpolated vectors to about 1% in both experimental cases. In order to reduce the effect of small-scale spurious noise on PIV results, a 5$\times$5 Gaussian filter with a standard deviation of 0.8 was used, as it was found to have an acceptably low effect on the small-scale velocity statistics. Concerning the laser synchronization for PIV image capturing, laser pulse time delays of 2.5 μs and 2.2 μs are used for $M \sim 1.55$ in the post-reschock and pre-reshock cases, respectively, whereas for

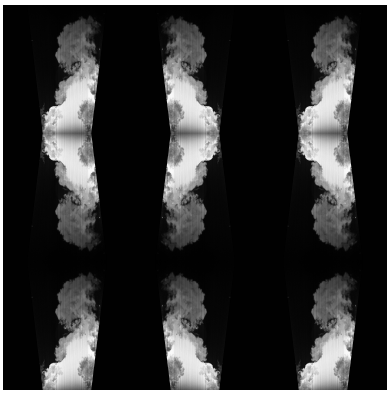

(a) Mirrored and padded image

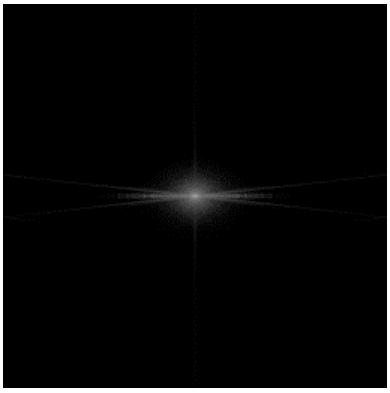

(b) Fourier transform of padded image

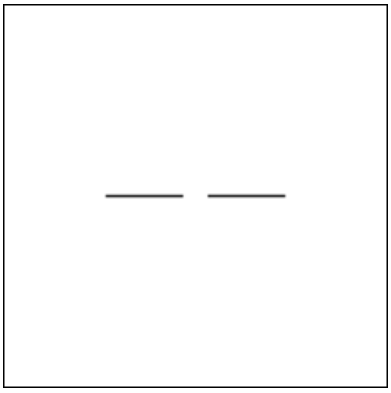

(c) Created mask

(d) Final corrected image

Figure 3.2: Notch filtering steps (a) Mirrored and padded attenuated image (note that the image has been transformed in a way that does not decrease resolution in order to make rays parallel so that streaks appear as high frequency content in only one direction and low frequency content in the other), (b) Fourier transform of padded image, (c) Created mask, (d) Final processed PLIF image after filtering of high frequency streaks due to index of refraction mismatch across the interface and reversing the aforementioned transformation.

$M \sim 1.9$, the time delays for laser pulse are 2 μs before reshock, 4 μs at early time after reshock and 7 μs at late time after reshock. The final in-plane vector spacing is 372 μm and 358 μm for $M \sim 1.55$ and $M \sim 1.9$, respectively.

3.3 Registering PIV Data with PLIF Fields

To register the results and images from each of these cameras, the calibration plate seen in Figure 3.1b was used. The plate was made at Georgia Tech so that each white dot is separated precisely by 10 mm in the X and Y directions, with a depth of 1 mm in the Z direction. To complete the calibration process, the plate was aligned with the laser light-sheet and illuminated with an external light source so each dot was clearly visible and focused. The plate was positioned such that each camera was able to capture its entirety. After capturing calibration images, a third order polynomial mapping function was used, as in Soloff, Adrian, and Liu (1997), to map the white dot locations on the image plane to their true measurement locations on the calibration plate in order to correct lens effect. After calibrating the images for both PLIF and PIV cameras separately, the two images are registered to the same coordinate plane by first shifting the fiducial point and using the corner dots to determine the scaling between the two images. Then the spatial region, which is not common to both velocity and density fields, is cropped. The result is that the two fields represent the same spatial region, but maintain the original resolution for calculations. This means that all independent statistics are calculated using the original resolution. However, cross statistics are calculated by resizing the concentration fields based on the stretching (making concentration and velocity fields the same size), which limits these statistics to the resolution of the velocity fields.

Figures 3.3 and 3.4 show examples of registered PIV vectors with the corresponding PLIF field for both single and multi-mode cases at the latest time after reshock for $M \sim 1.55$ and $M \sim 1.9$, respectively, indicating the fidelity of the measurements made. This visualization shows the connection between the velocity field and the density field, and

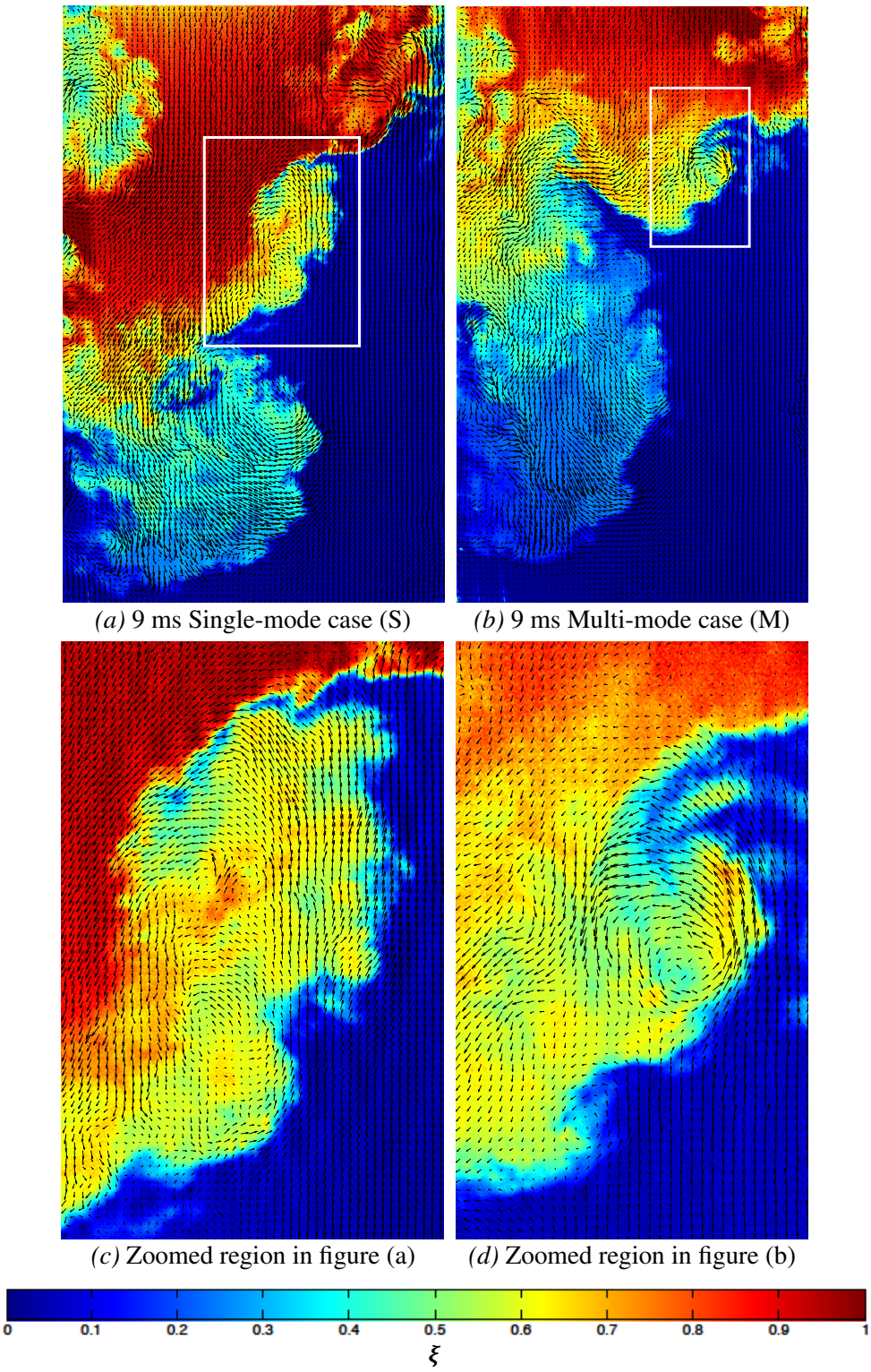

(a) 9 ms Single-mode case (S)

(b) 9 ms Multi-mode case (M)

(c) Zoomed region in figure (a)

(d) Zoomed region in figure (b)

Figure 3.3: Simultaneous PLIF/PIV field showing velocity vectors over pseudocolor concentration fields at the latest time after reshock ($\tau = 4.6$) at $M \sim 1.55$. Figures (a) and (b) include 1/4 of velocity field resolution and indicate the regions to be zoomed in Figures (c) and (d), which show 1/2 of velocity field resolution for clarity.

highlights that there is a velocity gradient across the density gradients, especially at the edge of the mixing layer where the density gradient is strong. However, a comparatively more chaotic state is present in the bubble region at $M \sim 1.55$, while both bubble and spike regions for $M \sim 1.9$ are generally more chaotic and mixed, but still contain a level of local inhomogeneity. The alignment of vorticity with concentration gradients is just one example of the utility gained by registering the simultaneous density and velocity fields. Density-velocity statistics are critical to the validation of turbulence models for variable-density flows and give insight into the physics of multi-component mixing in the developing RMI flow. The data is analyzed thoroughly in chapter 4.

3.4 Uncertainty Analysis

In the PLIF measurements, there are several factors to be considered which may affect uncertainty. These include the dynamic range or signal-to-noise ratio, absorption of the laser sheet along light rays (corrected using the Beer-Lambert law), index of refraction effects on the light sheet (corrected using notch filtering), and shot-to-shot variations in maximum image intensity.

First, it is important to analyze the dynamic range in order to consider how discreetly the values of density will be distributed. The signal (pixel intensity) of PLIF images on the side which is seeded by acetone and captured by 29 MP cameras with a total bit depth of 14 is ~ 4000 on average out of 16384, while the noise of the CCD chip is found to be ~ 20, and therefore the signal to noise ratio is ~ 200. It should be noted that the signal ratio of the acetone seeded region to the background image (~ 50) is ~ 80, which indicates a $\sim 2\%$ difference in the measured intensity caused by the background intensity. To account for this, background images are recorded and subtracted from the raw PLIF images. This difference should be noted, but since it is corrected for, the arising uncertainty is minimized and effectively lowers the dynamic range by approximately 1%. The laser energy fluctuations measured by laser power meter also have a standard deviation of 6.4%,

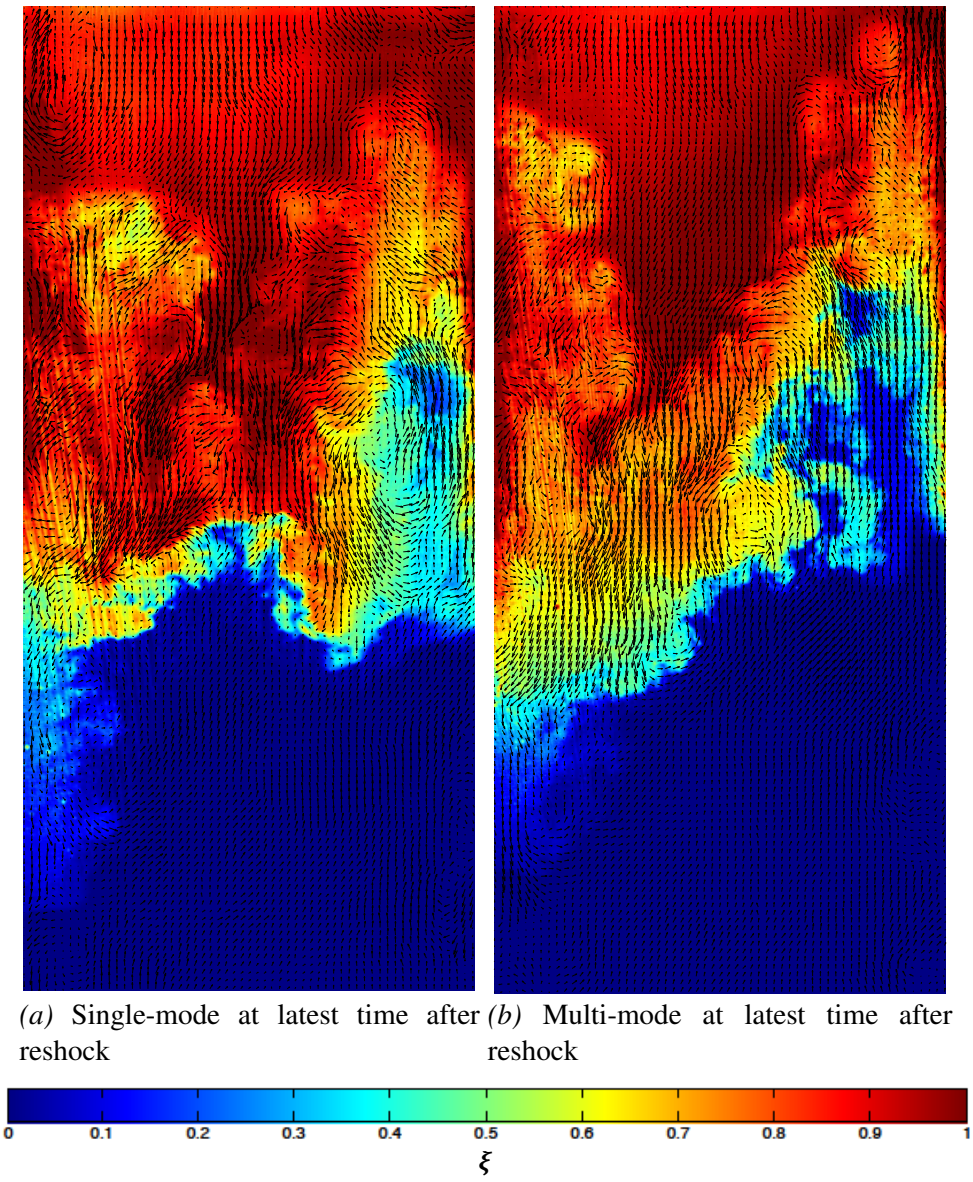

(a) Single-mode at latest time after reshock

(b) Multi-mode at latest time after reshock

Figure 3.4: Simultaneous PLIF/PIV field showing velocity vectors over pseudocolor concentration fields at the latest time after reshock ($\tau = 4.35$) at M $\sim$1.9, indicating several vortical structures in the flow, fidelity of measurements and accuracy of registry process. 1/5 of calculated vectors shown for clarity.

which yields a standard deviation of 0.9% in the maximum intensity of the PLIF images. So, considering the effect of these factors on dynamic range, a conservative estimate of 3900 for dynamic range can be made.

Attenuation due to absorption of the laser light by acetone effectively reduces the dynamic range as light travels along a light path, while bending of light by gradients in the index of refraction across the interface reduces the intensity of the whole path past that point. Both of these phenomena require corrections (explained earlier in chapter 3.1) to closely approximate the real concentration field. This results in types of interpolation in real space and Fourier space for the attenuation and index of refraction corrections, respectively. To understand the information deficit in the raw intensity data, and thus the level of interpolation, the raw image was subtracted from the attenuation-corrected image, which resulted in a difference of 4.6%. Then the attenuation-corrected image was subtracted from the notch-filtered image which resulted in a difference of 1.2%. These deviations are reported to provide insight into the uncertainty in the corrected measurements.

Regarding the uncertainty of 2D PIV measurements, first the systematic uncertainty due to the out of plane motion of particles should be considered. The actual displacement of particles between the laser pulses can be defined as D_x, D_y and D_z. Then the image displacement corresponding to a certain particle can be obtained by

$$x_i' - x_i = -Mag(D_x + D_z x_i'/z_0) \tag{3.8}$$

$$y_i' - y_i = -Mag(D_y + D_z y_i'/z_0) \tag{3.9}$$

where $(x, y)_i'$ and $(x, y)_i$ are particle position in the second and first image pairs, M is the magnification, D is a particle displacement and z_0 is the distance between recording plane and camera lens. It can be seen from these equations that the out-of-plane movement of particles (D_Z) affects the particle image displacement. Since this out-of-plane movement

of particles cannot be separated from the in-plane components of velocity, this effect introduces a systematic error. While this error can go up to 15% in PIV of three dimensional flow with high magnification at the edges of the image (Raffel *et al.*, 2018), the error is expected to be negligible in this study since the magnifications in the current work are $\ll 1$.

In addition to the systematic uncertainty, two approaches for the quantification of instantaneous uncertainty are assessed. The first method is the peak ratio (PPR) method, which assumes that the error on the measurement is related to the cross-correlation peak ratio (Charonko and Vlachos, 2013; Xue, Charonko, and Vlachos, 2014). Based on this method, errors related to the image quality and flow field can be assessed by computing the ratio between the largest detectable peak and the second highest peak in the correlation map. This uncertainty is calculated using the primary peak ratio in TSI Insight^{TM} 4G, and is defined by

$$|unc_{PPR}|^2 = A_1 exp(-1/2(\frac{PPR-1}{A_2})^2)^2 + (A_3.PPR^{\beta})^2 + A_4^2, \tag{3.10}$$

where A_1, A_2, A_3, β and A_4 are fitting coefficients. The percentage of relative uncertainty for both PPR and correlation statistics methods are calculated by

$$unc^{rel}_{PPR,Corr} = (\frac{|unc|}{\sqrt{U^2+V^2}}) * 100, \tag{3.11}$$

where U and V are measured streamwise and spanwise velocity. The absolute value and the percentage of relative PPR uncertainty are shown in Figure 3.5 before and after reshock. Before reshock, since flow velocity is much higher than uncertainty, the percentage of error is less than 1% on average, and the highest error occurs close to the interface (center of field). However, after reshock although the absolute uncertainty is lower, the percentage of relative uncertainty is $\sim 10\%$ on average and the maximum error is 18.7 % is much higher compared to pre-reshock cases, since the mean flow velocity is much slower after reshock.

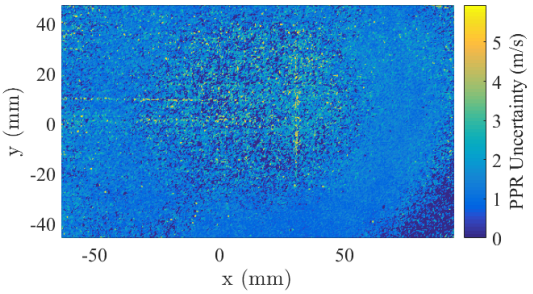

(a) Single-mode before reshock (absolute uncertainty value)

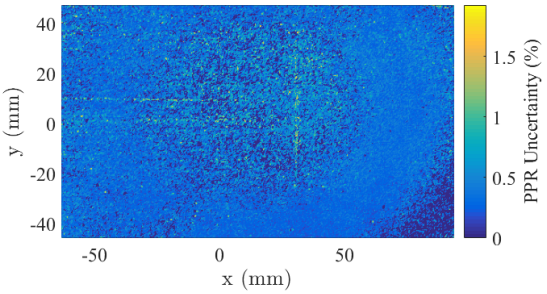

(b) Single-mode time before reshock (relative uncertainty value)

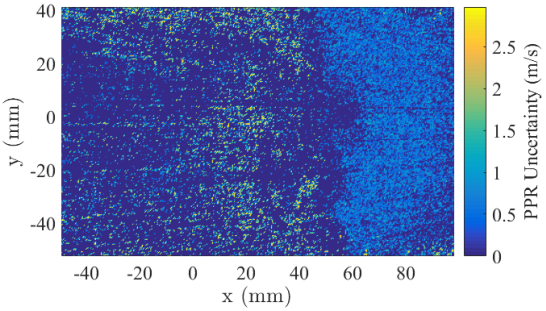

(c) Single-mode after reshock (absolute uncertainty value)

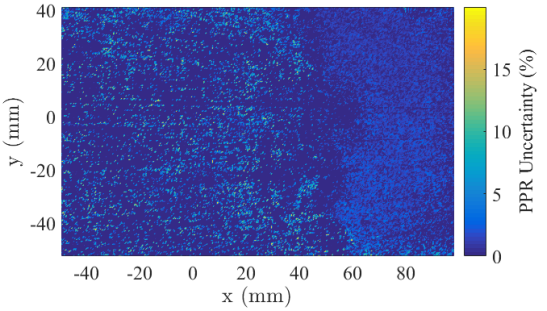

(d) Single-mode after reshock (relative uncertainty value)

Figure 3.5: (a,c) Absolute and (b,d) percentage of relative uncertainty using the peak ratio (PPR) method before (a,b) and after (c,d) reshock.

It is important to note that the uncertainty is higher in the light gas side and mixed regions.

The second approach which is used to quantify instantaneous uncertainty is correlation statistics method (Wieneke, 2015). This method estimates the contribution of all pixels in each interrogation window at one image pairs to the shape of the correlation peak, and quantifies the asymmetry of the correlation peak. This method assumes that uncertainty in the measurement is related to the shape of the correlation peak and it can include all errors such as background noise, out of plane particle motion, and particle disparities. In this work, this uncertainty is measured using LaVision DaVis, and similar to the previous method, both absolute and percentage of relative uncertainty are calculated. Additionally to investigate the effect of noise, the correlation maps before and after reshock at two interrogation windows in the light gas side, and two interrogation windows in the heavy gas side are shown in Figure 3.6. The size of distinguishable peaks in the correlation map

is related to the signal to noise ratio and the position of the peak in the map shows mean displacement of particles in that specific interrogation window. Note that correlation peaks shown in Figure 3.6 are a single-pass correlations without background subtraction, and the results presented here are expected to have more defined correlation peaks with a recursive processing. Before reshock, there is a well-defined peak in both light and heavy gas sides of the flow, however, after reshock in the light gas and mixed regions, the peak is not as sharp as it is on the heavy gas side. Also, the absolute and relative correlation uncertainty, shown in Figure 3.7, indicate higher error in the light gas side and mixed regions compared to the heavy gas side after reshock. The uncertainty magnitude from correlation statistics method before and after reshock is observed to be similar to the ones which are calculated using PPR method.

Furthermore, since velocity, density, and the corresponding derived statistics are random variables which are generally functions of space and time, statistical uncertainty should be estimated. Due to this, the central limit theorem suggests that the rate of statistical convergence is dependent upon the square root of the mean square error (MSE) or, alternatively, the standard deviation of the estimator (Bendat and Piersol, 2011),

$$\sqrt{var(\hat{\phi}(x))} = \sigma_{\hat{\phi}} = \sqrt{\frac{\sigma_{\phi}^2}{N_i}} \tag{3.12}$$

where $\hat{\phi}(x)$ is the estimator for any statistics of the random variable x and N_i is the total number of independent samples. For example, the sample mean $\bar{u}$ is an estimator for the population mean u-component velocity, μ_u. In this case $\hat{\phi} = \bar{u}$ and $\sigma_{\phi}^2 = \sigma_u^2$. N_i appears in the denominator, and hence convergence of any specific statistic is dependent on the number of realizations. Variances for the estimators of the statistics of interest were derived previously (Balakumar *et al.*, 2012; Benedict and Gould, 1996) and are shown in Table 3.1. For each of the statistics, confidence intervals may be formed following the method of

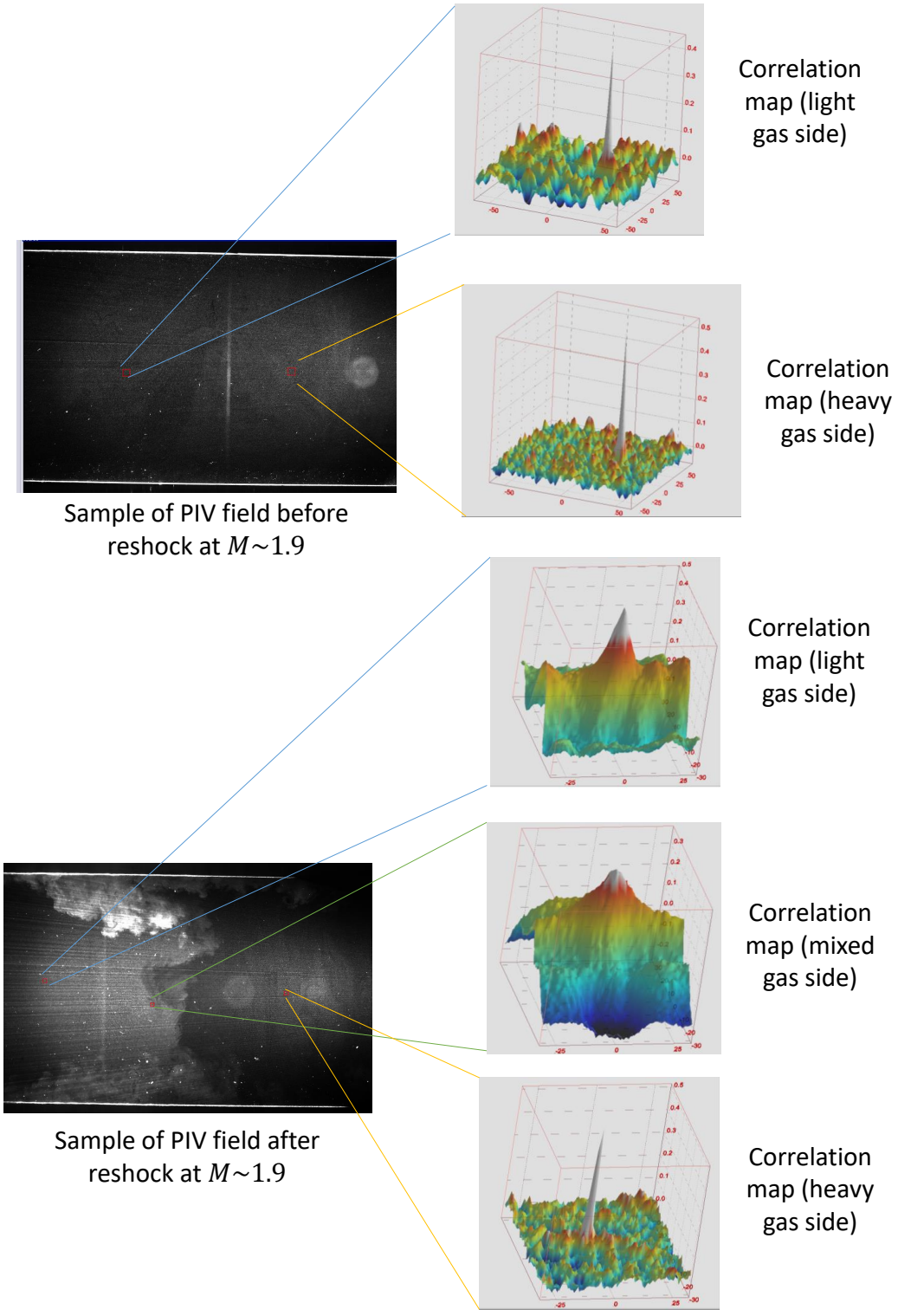

Figure 3.6: Cross correlation maps of the interrogation windows in different regions of the flow before and after reshock.

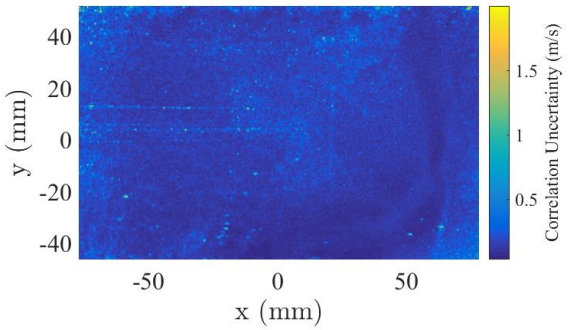

(a) Single-mode before reshock (absolute uncertainty value)

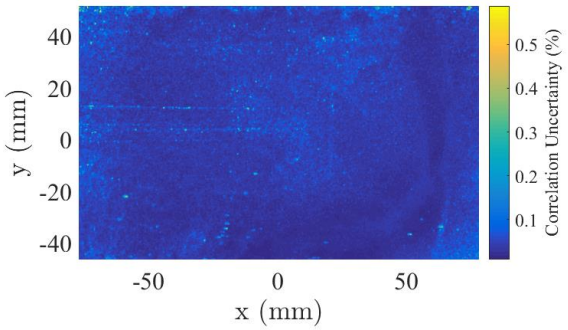

(b) Single-mode time before reshock (relative uncertainty value)

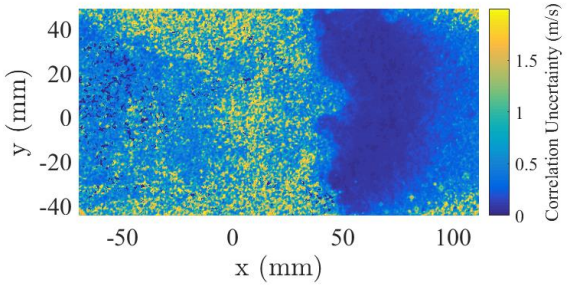

(c) Single-mode after reshock (absolute uncertainty value)

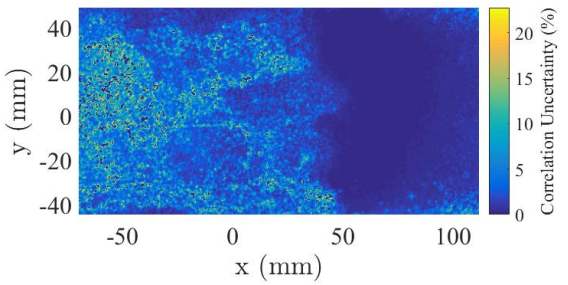

(d) Single-mode after reshock (relative uncertainty value)

Figure 3.7: (a,c) Absolute and (b,d) percentage of relative uncertainty using the correlation statistics method before (a,b) and after (c,d) reshock.

Benedict and Gould (1996),

$$\phi = \hat{\phi} \pm z_\alpha \sqrt{\frac{\sigma_\phi^2}{N_i}} \tag{3.13}$$

where z is the z-score for the normal distribution at the desired confidence interval (α), which was 95% for this study. Typical confidence intervals (CI) and one (σ) relative error (RE) level are shown in Table 3.1.

The experiment was repeated at fixed times after the arrival of the incident shock to produce independent ensembles. Small variations in particle and acetone density, shock velocity, image quality, and other experimental aspects make achieving identical conditions difficult. Although every effort was made to mitigate these variations, approximately 30 realizations were completed per test time for each initial condition, at most experimental times, in order to ensure minimal influence from these variations on the data set and to allow calculation of ensemble statistics. Approximations for the estimator variance and standard errors were calculated using $N_i \approx 30$. Furthermore, after averaging over the ensemble, many statistics are averaged in the spanwise direction to produce a profile against streamwise coordinates. This implies an assumption of spatial homogeneity across the layer. This assumption is typically accepted when a limited number of realizations are available (Shankar and Lele, 2014), and is necessary for comparison with many simulations and other experimental work. An initial calculation found the integral length scale (explained later in the length scale analysis), L, to be $L \approx 1.0$ cm, which was used to identify the length of independence in the spatial field. Therefore, the spanwise length, (≈ 10 cm), yields close to 10 independent samples per ensemble resulting in about 300 total for the spanwise-averaged calculations at most experimental times.

Table 3.1: Definitions, equations and convergence of statistical estimations.

Statistic, ϕ	Estimator, $\hat{\phi}$	$var(\hat{\phi}) \times N_i$	95% CI	One-σ RE(%)
u-velocity mean	$\bar{u}$	σ_u^2	$\pm\, 2.5\ m/s$	3.8
v-velocity mean	$\bar{v}$	σ_v^2	$\pm\, 2.1\ m/s$	10
density mean	$\bar{\rho}$	σ_ρ^2	$\pm\, 0.15\ kg/m^3$	1.2
u-velocity variance	s_u^2	$2(\sigma_u^2)^2$	$\pm\, 28.3\ m^2/s^2$	25.4
v-velocity variance	s_v^2	$2(\sigma_v^2)^2$	$\pm\, 19.0\ m^2/s^2$	25.6
density variance	s_ρ^2	$2(\sigma_\rho^2)^2$	$\pm\, 0.10\ kg^2/m^6$	27.5
Density self-correlation	b	$\frac{\sigma_\rho^2}{\bar{\rho}^2}\{\bar{\rho}^4\langle\frac{1}{\rho^4}\rangle + (1+b)^2 - 2(1+b)\langle\frac{1}{\rho^2}\rangle\bar{\rho}^2\}$	$\pm\, 0.0044$	21.8
Mass flux	$\frac{\overline{\rho' u'}}{\bar{\rho}}$	$\frac{2\sigma_u^2\sigma_\rho^2+2\sigma_{\rho u}^2}{\bar{\rho}^2} + \frac{\sigma_u^2\sigma_{\rho u}^2}{\bar{\rho}^4}$	$\pm\, 1.77\ m/s$	3.6
Reynolds Stress	$\bar{\rho}\overline{u'v'}$	$(\overline{uv})^2\sigma_\rho^2 + 2\bar{\rho}^2(\sigma_u^2\sigma_v^2 + \sigma_{uv}^4)$	$\pm\, 60.2\ kg\ m/s^2$	14.8

3.4.1 Statistical Convergence of Mean Statistics

Additional uncertainty in statistical quantities is due to finite number of samples n, which can yield lack of statistical convergence. In order to investigate statistical convergence of mean statistics, 112 realizations are collected at latest time after reshock for muti-mode initial condition. This time is chosen to collect large number of ensemble due to higher fluctuations in the flow and larger portion of mixed material. Based on the criterion of $< 5\%$ distance between the edge of the bubble for each realization and the average of the edge for all realizations, 75 realizations of PIV image pairs are chosen out of 112 realizations. The ensemble-averaged streamwise and spanwise velocity fields and the effect of the sample size on the accuracy of the statistical results is shown in Figure 3.8 at 5 different points in the flow. Four points are chosen in the mixed region and one point is chosen in the pure heavy gas side. Evidently, uncertainty of the mean velocity is initially large and decreases by increasing the number of samples. Table 3.2 shows the mean (μ) and variance (σ) of velocity at each point.

In addition, by assuming that μ is a true mean value at each point, to estimate the sample size which is needed to be $100(1-\alpha)$ percent confident that the error in estimating μ is less than a specified error percentage (E), the below equation could be solved (Montgomery and Runger, 2010)

$$n = (\frac{100 z_{\alpha/2} \sigma}{E\mu})^2. \tag{3.14}$$

Table 3.2 shows minimum sample size which is needed at each point chosen in the flow to be 92% confident (confidence interval or CI) for 20% desired error (E), 90% CI for 10% E, 95% CI for 5% and 25% E and finally 68.2% CI for 5% and 10% E. Based on these results, we can be 92% confident that the mean of statistics will not exceed 20% of total ensemble average when the sample size is around 30 to 35 (the number of ensemble which is chosen in the current work). However, it should be noted that data convergence

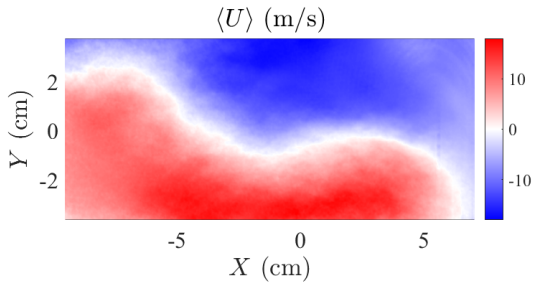

(a) ensemble-averaged streamwise velocity field at latest time after reshock for multi-mode case at $M \sim 1.55$

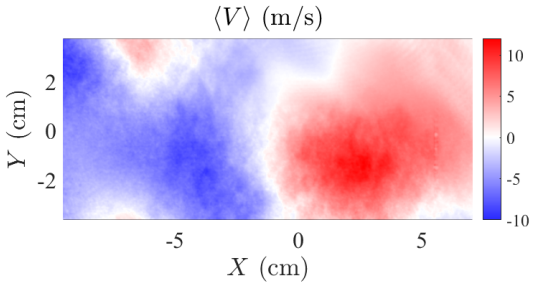

(b) ensemble-averaged spanwise velocity field at latest time after reshock for multi-mode case at $M \sim 1.55$

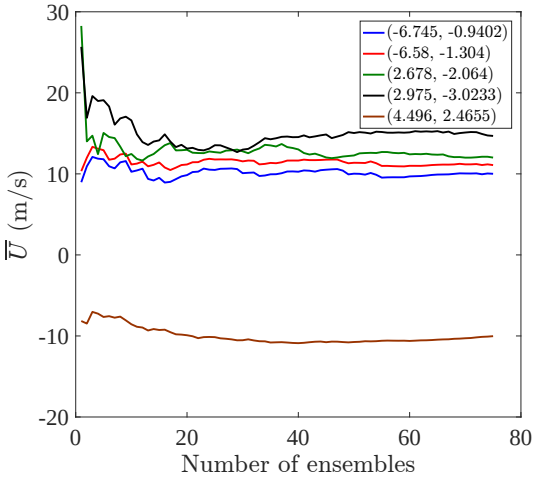

(c) Convergence of the mean streamwise velocity as a function of the sample size at 5 different points

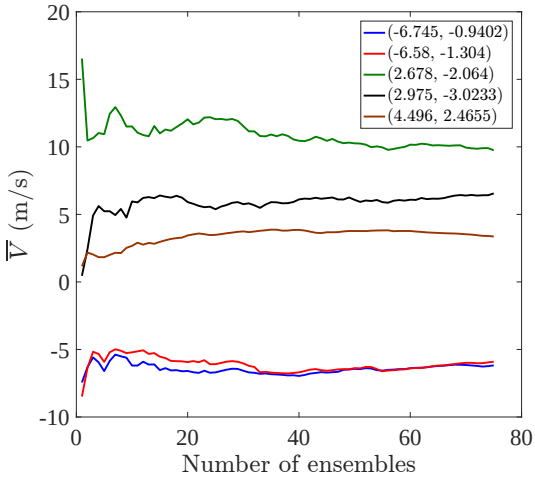

(d) Convergence of the mean spanwise velocity as a function of the sample size at 5 different points

Figure 3.8: (a,b) Ensemble-averaged streamwise and spanwise velocity fields at latest time after reshock for multi-mode case at $M \sim 1.55$. (c,d) Convergence of the mean streamwise and spanwise velocity as a function of the sample size at 5 different points.

Table 3.2: Estimation of minimum sample size needed to be $100(1-\alpha)$ percent confident that the error in estimating μ is less than a specified error percentage (E).

X **(cm)**	-6.58	2.678	-6.745	2.975	4.496
Y **(cm)**	-1.3038	-2.064	-0.9402	-3.0233	2.4655
$\mu_{\overline{U}}$	11.084	12.0121	10.0091	14.6828	-10.0272
$\mu_{\overline{V}}$	-5.9085	9.7443	-6.177	6.5537	3.3631
$var_{\overline{U}}$	27.968	52.558	40.982	72.715	6.9397
$var_{\overline{V}}$	11.157	33.075	7.197	20.315	2.912
$n_{\overline{U}}, n_{\overline{V}}$ **based on 92% CI** ($z = 1.75$)**, 20% error**	17 24	28 27	31 14	26 36	5 20
$n_{\overline{U}}, n_{\overline{V}}$ **based on 90% CI** ($z = 1.645$)**, 10% error**	62 86	99 94	111 51	91 128	19 70
$n_{\overline{U}}, n_{\overline{V}}$ **based on 95% CI** ($z = 1.96$)**, 25% error**	14 20	22 21	25 12	21 29	4 16
$n_{\overline{U}}, n_{\overline{V}}$ **based on 95% CI** ($z = 1.96$)**, 5% error**	350 491	560 535	629 290	518 727	106 396
$n_{\overline{U}}, n_{\overline{V}}$ **based on 68.2% CI** ($z = 1$)**, 10% error**	23 32	36 35	41 19	34 47	7 26
$n_{\overline{U}}, n_{\overline{V}}$ **based on 68.2% CI** ($z = 1$)**, 5% error**	91 128	146 139	164 75	135 189	28 103
Notes	Mixed region	Mixed region	Mixed region	Mixed region	Pure region

for higher level of confidence and less error, or higher order statistics requires much larger sample size. Therefore since collecting large ensemble of data in shock tube experiments is difficult due to the nature of these experiments, it should be noted that this uncertainty is inherent in the shock tube experimental works investigating turbulence statistics. This uncertainty is tried to be reduced in this work by choosing larger ensemble compare to other works in the literature, removing data with more than 3% deviation from mean of Mach number, the location of edge of bubble as discussed and by readjusting realizations based on their center of masses.

3.5 Methods of Variable Decomposition

In general, fluctuations should be calculated from averages over homogeneous dimensions (average fluctuating quantities are invariant in that dimension). In many turbulent flows there may be multiple spatial dimensions, and possibly the temporal dimension, which provide this necessary homogeneity (or stationarity, in temporal sense). However, in flows where there is dimensional dependence of a fluctuating quantity, averaging should not be performed over dimensions in which this inhomogeneity occurs. RMI is temporally evolving, which precludes temporal averaging. Furthermore, in most RMI flows there is significant spatial inhomogeneity throughout flow even after transition to turbulence. This spatial inhomogeneity can be due to the dependence on initial conditions, continued influx of pure fluid with a velocity preference at the edges of the mixing region, and documented conditional dependence (correlation) of velocity and density fluctuations. Several statistics like fields of density self-correlation, shown in figure 4.14, for late time before and after reshock indicate this spatial inhomogeneity in the flow.

Therefore, since different methods of averaging have been used in the RM field, it is necessary to clarify the difference between these methods and the physical meaning behind each one, and in order to reliably perform velocity field analysis, the velocity fluctuations must be calculated correctly, from spanwise, boxcar or ensemble averaging. First, comparison between spanwise and ensemble averaging is shown. To calculate velocity fluctuations using spanwise averaging, the bulk velocity u_b was defined as the streamwise and spanwise spatial average of the i-th component of the velocity. The relative velocity was then defined as the difference between the instantaneous and bulk velocities,

$$u_b = (\overline{u_i})_{x,y} \tag{3.15}$$

$$u_{rel} = u_i - u_b. \tag{3.16}$$

Next, the relative velocity was spatially averaged over the spanwise or y-direction. Then the velocity fluctuation, u'_{span} was defined as the relative velocity minus the spanwise-averaged velocity,

$$u'_{span} = u_{rel} - (\overline{u_{rel}})_y. \tag{3.17}$$

Velocity fluctuations found using ensemble averaging were obtained by taking the difference between the instantaneous velocity and an ensemble average which is defined by:

$$u' = u_{rel} - \langle u_{rel} \rangle. \tag{3.18}$$

The two methods yield notably different results. To highlight the effect of ensemble averaging versus the use of traditional spanwise averaging, Favre averaged Reynolds stresses for the multi-mode case at late time, post-reshock, for $M \sim 1.55$ are shown in Figure 3.9. For the Favre averaged Reynolds stress, velocity fluctuation components come from mass weighted average quantities: $\tilde{u_i} = \overline{\rho u_i}/\overline{\rho}$. Figure 3.9 shows that the most significant difference between the two methods is the magnitude of the $u''u''$ term, which is significantly higher when using spanwise averaging, due to the large fluctuations in the streamwise velocity across the interface. The $v''v''$ and $u''v''$ terms are similar in magnitude but show more variation across the interface in the ensemble-averaged case. In a statistically repeatable, homogeneous turbulent flow field it would be expected that the ensemble and spatial averages would yield the same result. However, the large difference in the streamwise direction highlights the need for ensemble averaging due to the inhomogeneity of the streamwise velocity across the interface.

In addition, a moving boxcar averaging method is used in the recent work by Reese *et al.* (2018), where the spatial filter window size was chosen as 1/20 of average mixing height. To compare these two methods of averaging (ensemble averaging and boxcar av-

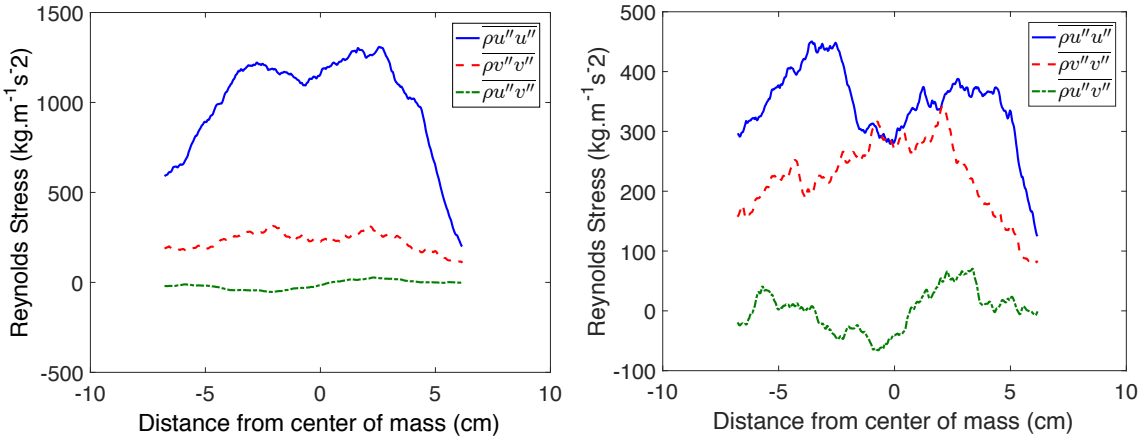

(a) Spatial averaged *(b)* Ensemble averaged

Figure 3.9: Comparison of Favre averaged Reynolds stress components in the multi-mode case at latest time after reshock for $M \sim 1.55$ based on two methods of velocity fluctuation calculation: spatial versus ensemble averaging.

eraging), relative velocity fluctuations (u'_{rel}) calculated using the boxcar averaging method are compared with velocity fluctuations from ensemble averaging (u') at the latest time after reshock for a velocity field sample and are shown in Figure 3.11. The velocity fluctuation for the ensemble averaging method, same as the previous comparison between ensemble and spanwise averaging, is defined as follows:

$$u_b = (\overline{u_i})_{x,y} \tag{3.19}$$

$$u_{rel} = u_i - u_b \tag{3.20}$$

$$u' = u_{rel} - \langle u_{rel} \rangle, \tag{3.21}$$

while for boxcar averaging method is calculated as

$$u'_{rel} = u_{rel} - (\overline{u_{rel}})_{boxcar}. \tag{3.22}$$

where the boxcar average is taken over the filter window.

To compare these two methods, both fields at the latest time before reshock and profiles at latest time after reshock at $M \sim 1.9$ are shown in Figures 3.10 and 3.11, respectively.

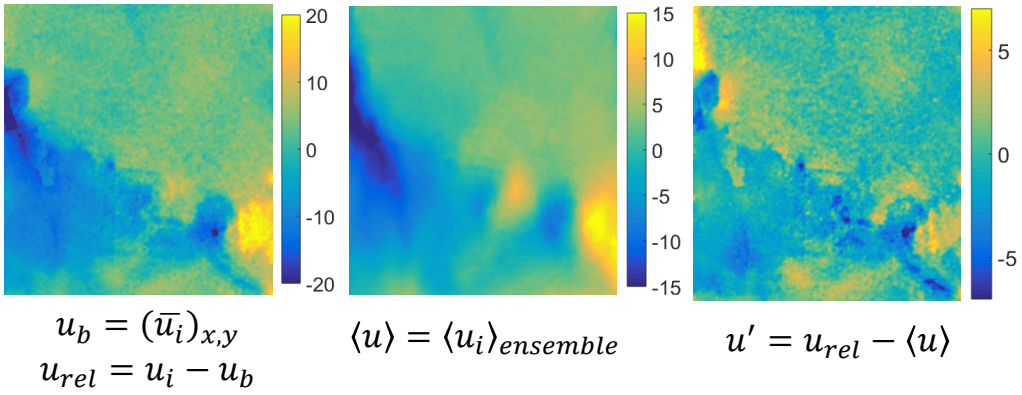

(a) Streamwise velocity field decomposition from ensemble averaging method

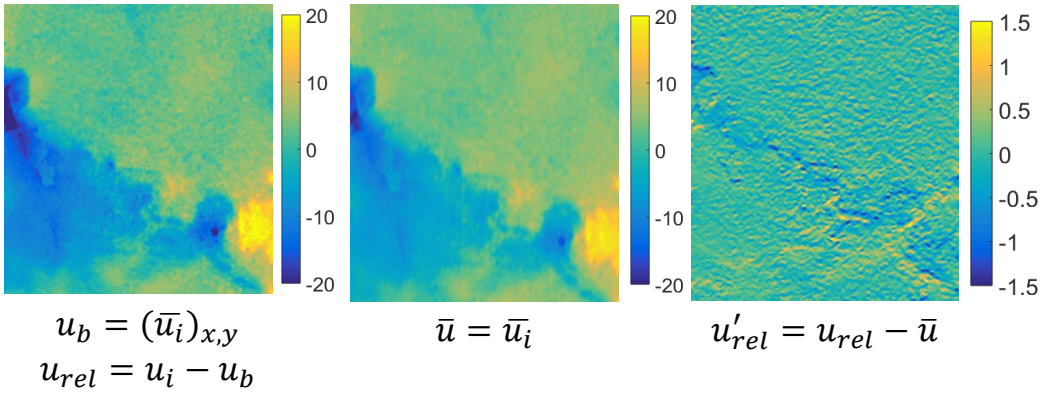

(b) Streamwise velocity field decomposition from boxcar averaging method

Figure 3.10: Decomposition of a sample velocity field at the latest time before reshock ($\tau = 2.27$) at $M \sim 1.9$: a) velocity relative to the bulk flow, its ensemble average, and its fluctuating component and b) velocity relative to the bulk flow, its boxcar average, and their difference.

The comparison between ensemble and boxcar averaging shows that fluctuations from boxcar averaging method indicate fine-scale features in each realization, based on local spatial variance rather than fluctuations from the ensemble dataset. Also, this method is very sensitive to the filter size. Therefore, in this thesis, fluctuations are calculated from ensemble averages, with the exception of calculations used to exemplify differences in averaging methods.

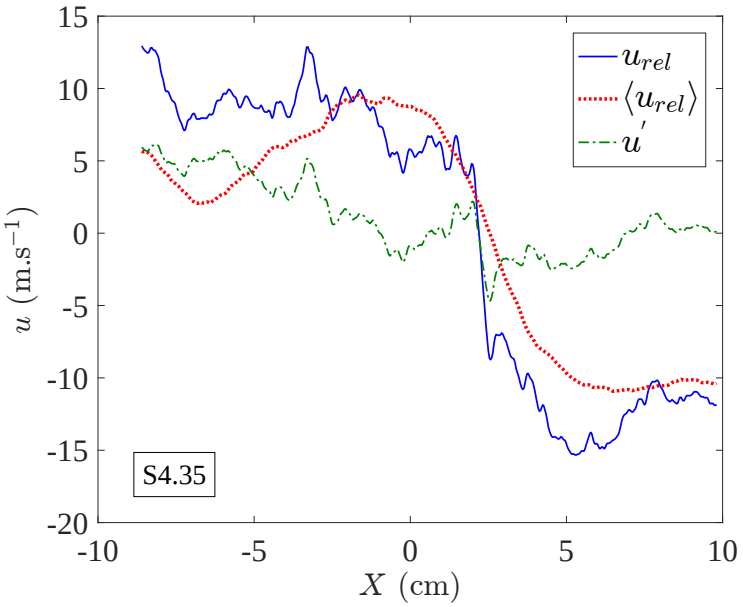

(a) Streamwise velocity field decomposition from ensemble averaging method

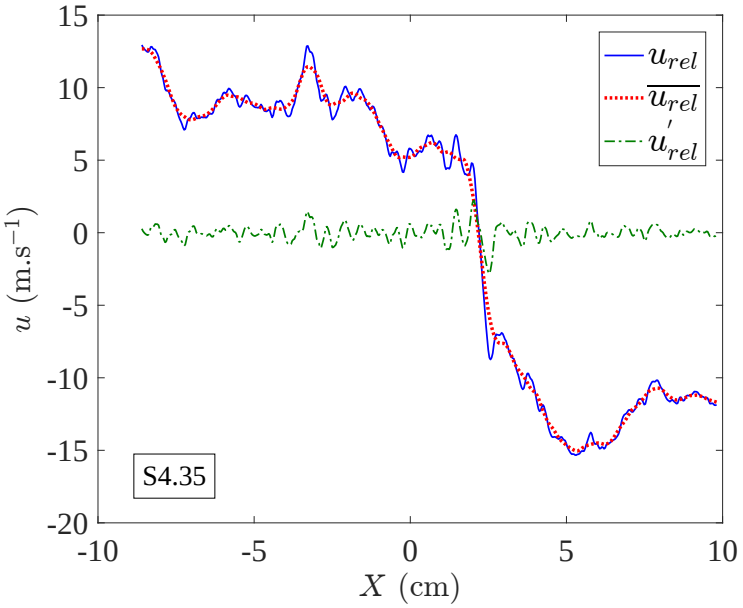

(b) Streamwise velocity field decomposition from boxcar averaging method

Figure 3.11: Decomposition of a sample velocity field at the latest time after reshock ($\tau = 4.35$) at $M \sim 1.9$: a) velocity relative to the bulk flow, its ensemble average, and its fluctuating component and b) velocity relative to the bulk flow, its boxcar average, and their difference. The results are averaged in the spanwise direction for clarity.

CHAPTER 4
RESULTS AND DISCUSSION

The results in this section is based on over 700 experimental runs. The PLIF and PIV images are then analyzed and classified based on the errors and run to run variations in the data, and finally around 400 simultaneous PLIF/PIV realizations are chosen to extract data. Some of the criteria which are investigated include: the Mach number deviation of less than 3% from the average, the signal to noise ratio of > 180 in the PLIF images, and $< 5\%$ distance between the edge of the bubble for each realization and the average of the edge for all realizations. It should be noted that to accurately compute turbulence statistics, the data which met the criteria had their center of masses readjusted before data extraction. In addition, to study RMI evolution, several runs at different times at each window locations are performed to capture PLIF images, and the highest quality ones are used to extract data. In this chapter, the effects of both initial conditions and Mach number on several statistics related to density, velocity, and density–velocity cross-statistics are calculated and analyzed using ensemble averaging.

4.1 Analysis of Flow Field Evolution

4.1.1 Qualitative Analysis of Evolution of Density Fields

Using several samples of corrected PLIF images, the current section provides a complete temporal evolution of the density fields for both experimental cases ($M \sim 1.55$ and $M \sim 1.9$). First, the lower Mach number case is discussed. The concentration field evolution for the single-mode at $M \sim 1.55$ is depicted in Figure 4.1, while the evolution for the multi-mode case is shown in Figure 4.2. Each individual realization is created from a single experimental run, meaning they are not truly subsequent images from the same experiment,

and thus the flow features will not match exactly from one time to the next. The images do, however, show general agreement between features from image to image. Proceeding from top-left to bottom-right, the initial interface is shown in the top left of each figure. The interface interaction with the incident shock marks the start time of the evolution of each field. The incident shock direction is from top to bottom in the images (from light to dark fluid), although the shock itself was not captured in the images. However, the next few images show the interaction of the reshock wave with the interface (moving from bottom to top), which appears as a sharp gradient in the light gas at 5.2 ms and 5.3 ms in both figures. Several realizations follow which show the post reshock development of the field through the latest time ($t = 9.0$ ms).

As can be seen by surveying Figures 4.1 and 4.2, the general orientation of the interface overturns and is linked to an overall interpenetration between the two gases, which is similar for both cases because it is mainly dependent on the longest wavelength mode of perturbation present in the initial condtion (i.e. the overall inclination). Both figures show that the flow field is becoming more turbulent and mixed, while the mixing layer is also growing, from the start of the evolution through the latest times. However, general differences do exist as the interpenetration and mixing of the single-mode case is characterized more by coherent vortices and large structures, whereas the multi-mode case displays more chaotic behavior and smaller features.

In each case the incident shock compresses the diffusion layer and intensifies the density gradients as can be seen in the first two images of Figures 4.1 and 4.2. As the incident shock pushes the interface closer to parallel with the streamwise direction, it stretches due to difference in velocity of two gases and consequently shear between them, thereby increasing the surface area and further sharpening the density gradient.

In the single-mode case, diffusion is the primary form of mixing at the surface of the interface. It is interesting to note that later (through mixing analysis) the rate of diffusion is less than the rate of sharpening since there is a net increase of the gradient. However,

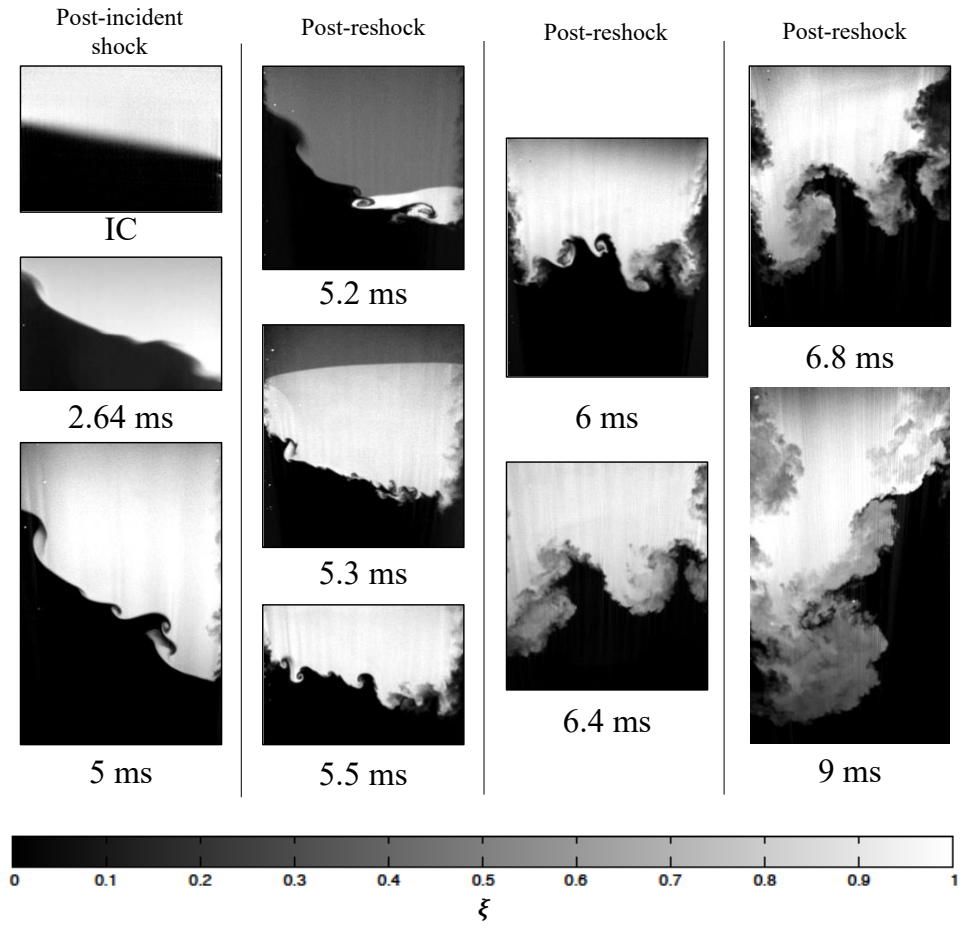

Figure 4.1: Concentration field evolution of single-mode initial condition at $M \sim 1.55$ with experimental times shown. Reshock hits the interface at $t \approx 5.2$ ms ($\tau \approx 2.4$).

in the multi-mode case, in addition to shear/diffusion effects, small-scale transport across the interface due to small, actively growing multi-mode secondary perturbations serves as a major mechanism of mixing even prior to reshock. The most noticeable observation before reshock is that the multi-mode secondary perturbations of the multi-mode case initially grow more rapidly due to the deposition of less-organized vorticity on the more complex initial condition, leading to greater mixing across the interface as their smaller scales break down earlier and contribute to increased mixing and a more irregular interface.

The latest time before reshock, 5 ms, is considered to be the initial condition for the reshock interaction at lower Mach number case [last images of Figures 4.1 and 4.2 before reshock]. The interface positioning for reshock is a key feature in the flow evolution as both

interfaces have a major inclined mode, yet also have significant coherent structures separate from the dominant inclined mode. Thus, the initial condition for reshock is multi-mode in both cases, however, the important difference between the two cases is the distribution of the wavelengths of these modes. The multi-mode case has structures with wavelengths and amplitudes extending over a wider, and relatively continuous range compared to single-mode case. One can also infer from the figures that the multi-mode case has more mixed-mass at the interface, yielding density gradients that are less sharp.

Reshock re-compresses the interface, intensifying the density gradients. After reshock, the interface begins to overturn counterclockwise, or in reverse of the direction of rotation caused by the incident shock interaction. The overturning pushes the interface past a perpendicular orientation relative to the streamwise direction just after 6.0 ms. This is often called a phase reversal, referring to the phase of the periodic interface. As was the case before reshock, the long wavelength perturbation once again has the strongest effect on the overturning motion and the overall extent of interpenetration of the two fluids. In contrast to the stretching that occurs pre-reshock, at early times post-reshock the interface is confined as it reverses direction, eventually becoming oriented perpendicular to the streamwise direction. Finally, once the interface proceeds past perpendicular, stretching begins anew to intensify the density gradients. The reshock wave, which is visible traveling from right to left in the images for 5.2 ms and 5.3 ms, is shaped by the interface but becomes smooth very quickly. A comparison of the two cases at 5.5 ms highlights the effect of the reshock initial condition. The single-mode case displays the growth of several distinct protrusions along the interface which appear to be inversions of similarly scaled structures existing prior to reshock. The multi-mode case is less organized, more diffuse, and has more small scale features scattered along the underlying long-wavelength perturbation. This contrast is due to shock interaction with a wider range of scales in the multi-mode case, including much smaller features, which have developed due to the faster break-down of the original mid-range-scale structures prior to reshock.

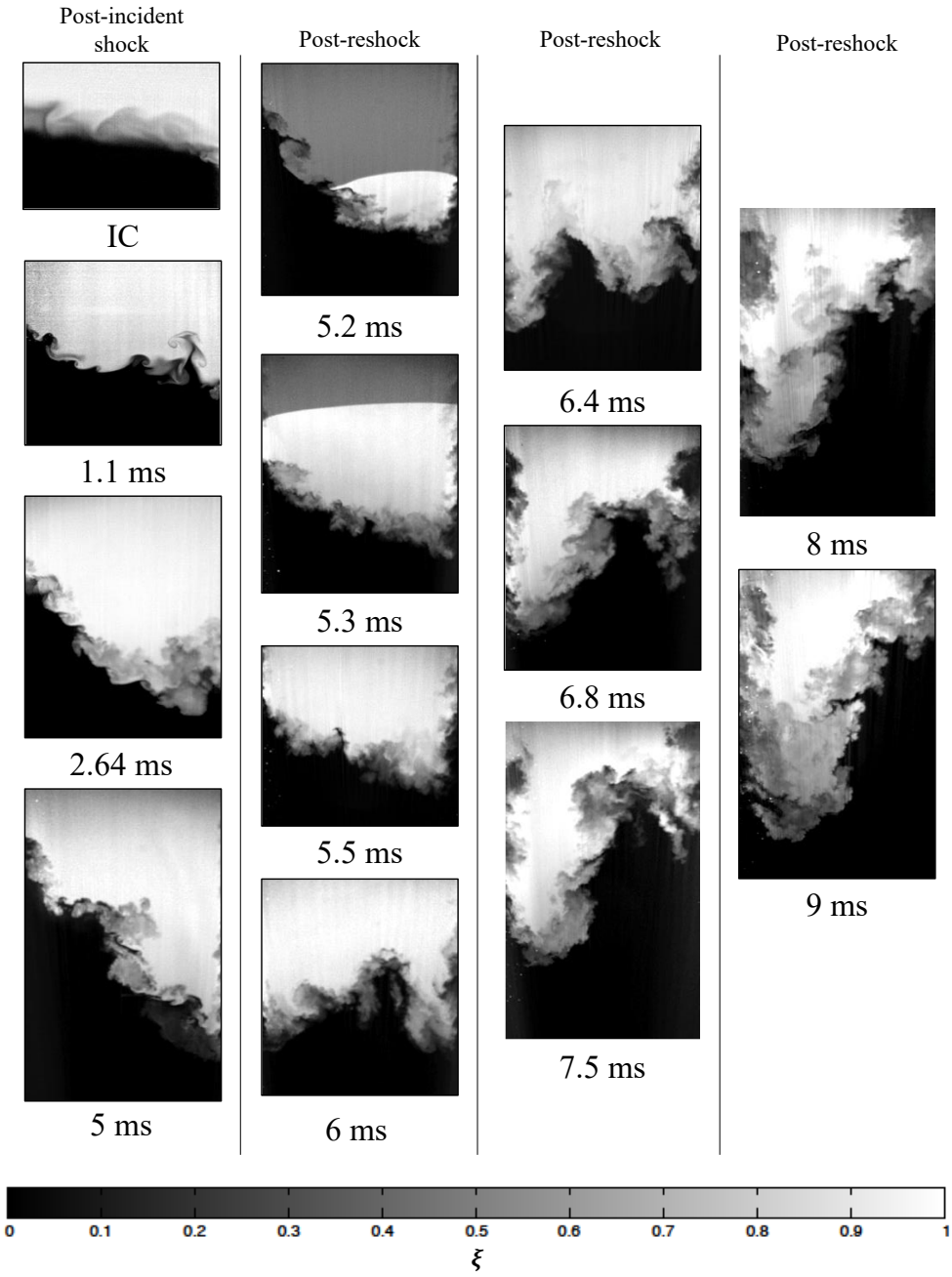

Figure 4.2: Concentration field evolution of multi-mode initial condition at $M \sim 1.55$ with experimental times shown. Reshock hits the interface at $t \approx 5.2$ ms ($\tau \approx 2.4$).

As the interface rotates counter-clockwise and the features are condensed, the interaction of modes becomes apparent. The smaller distinct structures in the single-mode case begin to merge and form a pair of large coherent features (spikes of dark carbon dioxide) which curl as the interface continues to overturn and stretch (6 ms - 6.8 ms). These general features persist to late time but are broken down as secondary instabilities distribute vorticity on the interface, increasing mixing and diffusion. Qualitatively, it appears from last image in Figure 4.1 that much of the mass previously contained in the spike has been stripped off and entrained in the strong bubble region at the bottom right of the image. In Figure 4.2, between 6.4 ms and 8 ms, the more chaotic large features of the multi-mode case form a shape which at 9 ms appears, qualitatively similar to the single-mode case. However, the two large structures [distinct vortical spikes near the center of images at 6.8 ms and 9 ms in Figure 4.1] that persist in the single-mode case are not recognizable in the multi-mode case, which is instead characterized by many smaller irregular features. These features might be remnants from the post-reshock initial growth state or could be newly developing features born from secondary instabilities. In the latter case, these instabilities may be induced by shear and large scale rotations of the entire interface, or even individual regions, which transport gradients and generate new vorticity through baroclinic torque as centripetal accelerations and density gradients interact. Overall, the general form of each case at 9 ms is similar. Both are dominated by a large bubble and spike combination that contains a mixing layer which appears to be in a turbulent state, as it contains a large range of scales and a considerable amount of mixing.

Furthermore, the evolution for the single- and multi-mode cases at high Mach ($M \sim 1.9$) is shown in figures 4.3 and 4.4. In the single-mode case (figure 4.3), the compression of the interface by the incident shock can be observed between $0 < t < 0.1$ ms, which results in intensification of the scalar gradient across the interface. Little other development is noticeable at the earliest times. A subtle, nearly-sinusoidal waveform can be observed at $t = 0.9$ ms at a wavelength approximately equal to the width of the tube. After this time,

the overall growth of the interface amplitude, and further intensification resulting from its stretching are noticeable. Additional features with shorter wavelengths develop, some of which eventually grow to significant amplitudes. More importantly, the complex topology of the interface is evident with two well-developed roll-up features between $3.7\,\text{ms} < t < 3.9$ ms, the late times before reshock. This forms the initial condition for reshock.

The main difference between the two Mach numbers before reshock, is the interface features at late times that are especially apparent in the single-mode case. While both the low and high Mach interfaces are fairly smooth and organized, the high Mach case contains additional small perturbations and a complete roll-up feature which is visually evident in the single-mode case. These features are largely due to the tendency of vorticity along the surface to concentrate and roll up via the Kelvin-Helmholtz instability. These differences will also be discussed quantitatively in the analysis of vortex sheet roll-ups.

At $t = 4$ ms the shock has been reflected off the bottom wall of the tube (reshock) and is traveling upwards, appearing as a sharp gradient in the PLIF image. The shock has been shaped by the interface and is beginning to replanarize at this time. The interface is compressed by reshock (as with the initial shock), and some small-amplitude, short-wavelength features can clearly be observed immediately after its traversal. As the long wavelength perturbation undergoes a phase inversion, the additional features are also observed to invert although their signature is much more subtle. Between images at 3.9 and 4.8 ms, the interface inverts, and the uppermost extent of heavy fluid before reshock becomes the lowest extent of light fluid. Additionally the two prominent roll-up features, where the heavy fluid penetrates into the light fluid before reshock are inverted and are observed as two regions of light fluid penetrating into heavy fluid after reshock. After 4.8 ms these features become indistinguishable, and the interface begins to look increasingly chaotic. As the phase inversion at the long wavelength continues, a breakdown of scales and consequent increase in mixed material is observed.

A similar sequence showing the RMI evolution resulting from the multi-mode initial

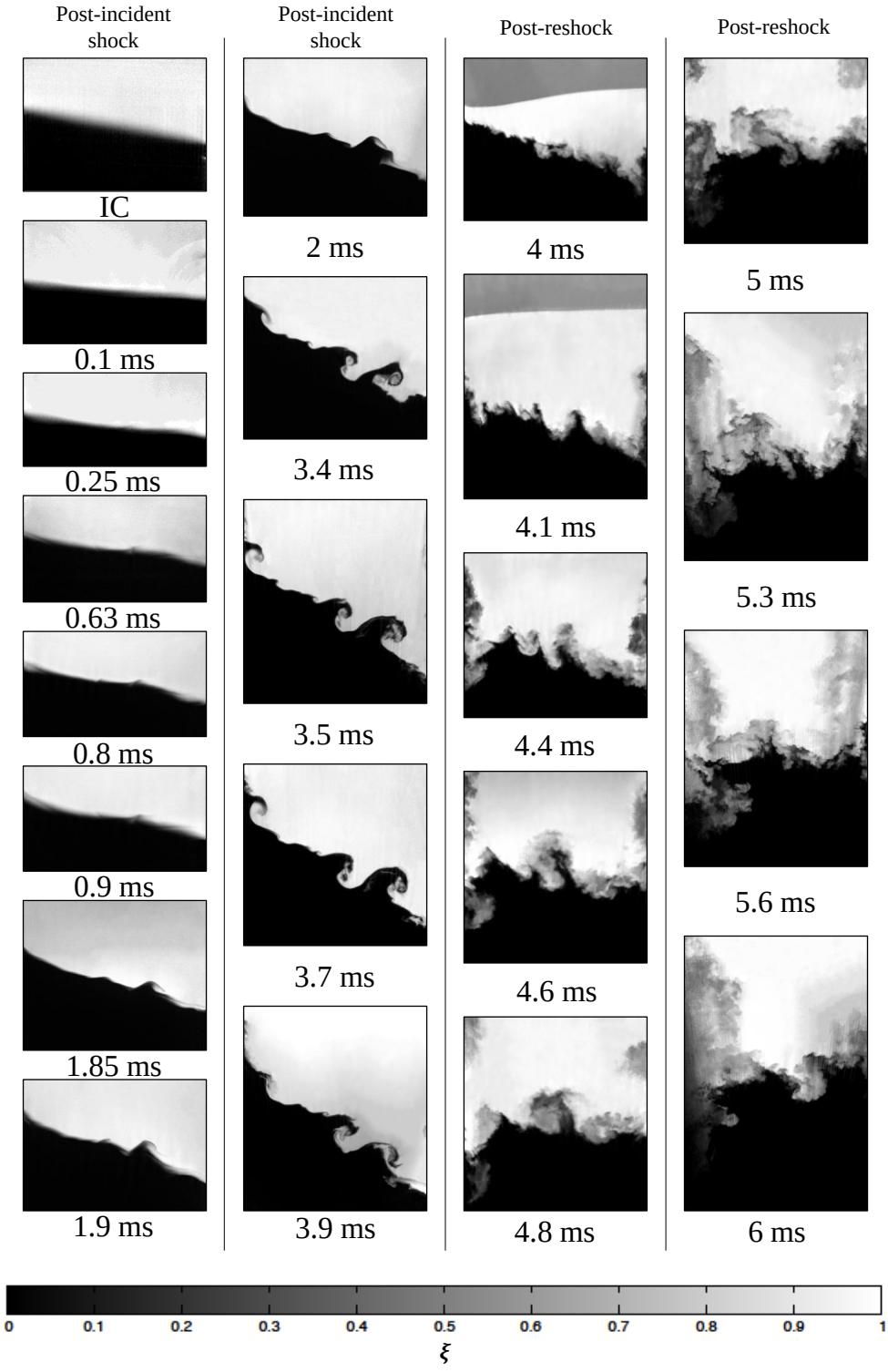

Figure 4.3: Concentration field evolution of single-mode initial condition at $M \sim 1.9$ with experimental times shown. Reshock hits the interface at $t \approx 4$ ms ($\tau \approx$2.4).

condition is presented in figure 4.4. Before reshock, the multi-mode case shows additional small-scale features throughout the evolution that were previously not seen with the single-mode interface. These observations are anticipated, owing to greater modal content in the initial condition, and are similar to those observed in the low Mach case. Also, due to a larger modal content in the features present in the multi-mode case at late times before reshock, the interface seems to have fewer large scale features immediately after reshock. This phenomenon is due to increased interaction of features which have different-signed vorticity, leading to a greater breakdown of coherent medium-sized features.

4.1.2 Mixing Width

The state of the flow in the following sections is analyzed through quantitative concentration fields. Values of density calculated from 1-D gas dynamics can be applied to the known values of concentration. From the density fields we can extract statistics that describe the state of mixing and begin to understand the flow field evolution.

With a qualitative understanding of the evolution of the single- and multi-mode interfaces, the current section discusses the quantitative aspects of the same using mixing width, mixing layer thickness and mixed-mass. Mixing width (h) is defined as the $5\% - 95\%$–extent (in the shock propagation direction) of spanwise-averaged nitrogen volume fraction (Olson and Jacobs, 2009; Weber *et al.*, 2012), and is a measure of the amplitude, or largest length-scale, of the instability. The growth of the mixing width is dependent on the velocity jump of the interface (proportional to the Mach number of the initial shock/reshock).

Figure 4.5 shows the evolution of the mixing width from the experiments at $M \sim 1.9$, alongside the $M \sim 1.55$ experiments for both the initial-condition configurations. The dependence of the mixing width growth on the Mach number is evident, as explained before, with the slope of $M \sim 1.9$ mixing-width consistently higher than the $M \sim 1.55$ cases before and after reshock. The single- and multi-mode interfaces, however, show identical growth behavior in the mixing-width. This independence of the smaller modal

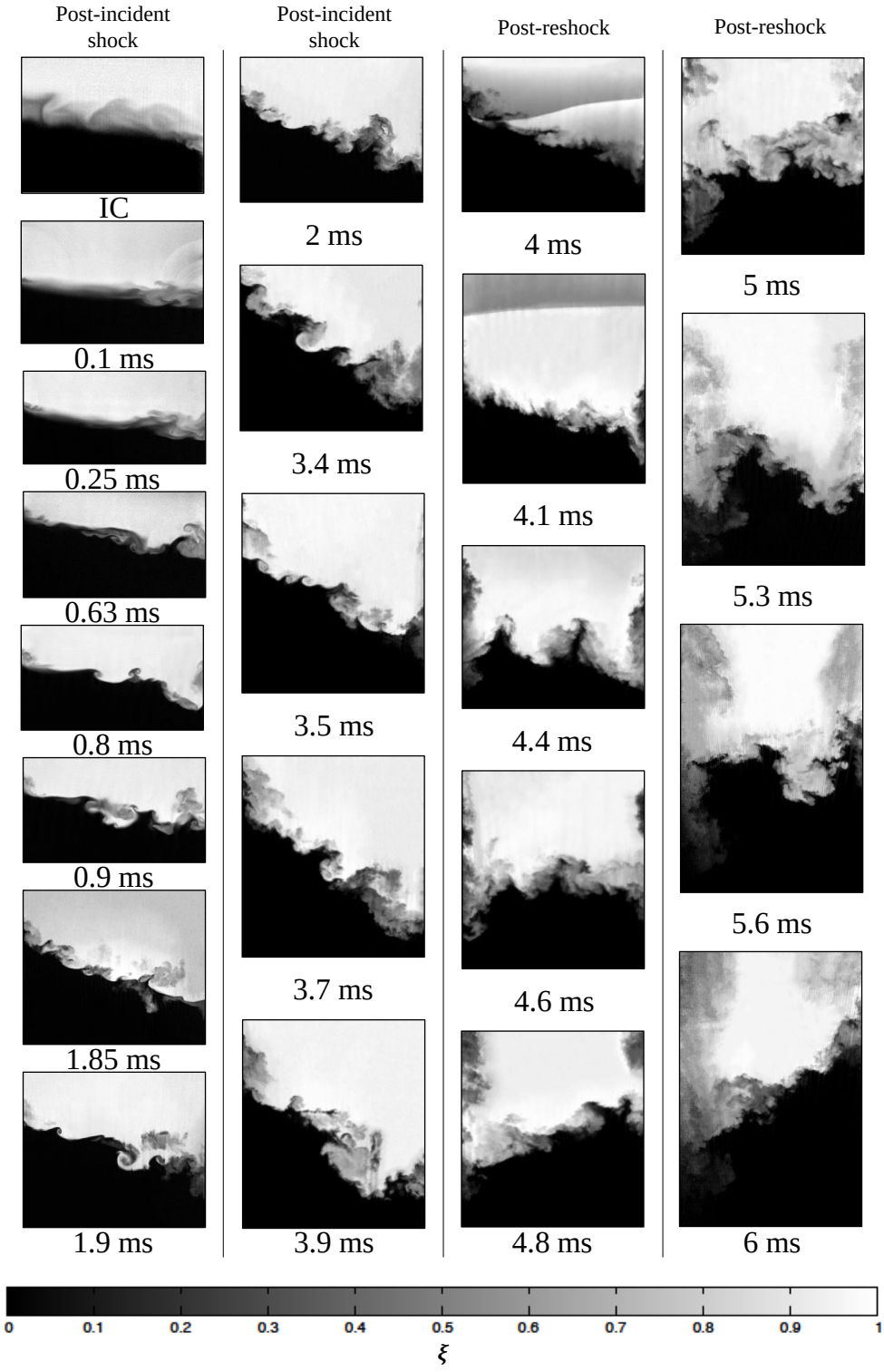

Figure 4.4: Concentration field evolution of multi-mode initial condition at $M \sim 1.9$ with experimental times shown. Reshock hits the interface at $t \approx 4$ ms ($\tau \approx$2.4).

content is anticipated as the growth in h is predominantly driven by the largest mode of the initial perturbation (inclined interface in both the interfaces).

The growth of the interface follows a fairly linear trend at the earliest times as expected for an amplitude-to-wavelength ratio of the inclined perturbation $\alpha = 0.088$, and maintains a trend which is fairly close to linear even until reshock. The linear growth corresponds to the strong penetration seen in the density fields. The overall growth rate of the mixing layer calculated from experiments can be compared to analytical results, which is computed for the case of $M \sim 1.55$. The growth rate calculated from experiments at $M \sim 1.55$ is approximately 17.2 m/s just after shock passage (initial growth rate is very similar for both cases), for which the linear theory of Richtmyer predicts a growth rate of 16.9 m/s (Richtmyer, 1960). Using the model of Weber, Cook, and Bonazza (2013) to extract the growth rate by modeling vorticity deposition and applying the Biot-Savart law yields a growth rate of 17.3 m/s at $M \sim 1.55$. As secondary instabilities begin to have larger effects, a change in growth rate from linear to non-linear is expected as the penetrating mass spreads through the mixing region more rapidly and homogeneously. Although a strongly nonlinear trend is not obvious, it is apparent that secondary instabilities play a role in the mixing process; we see significant spreading of mass throughout the mixing region in the multi-mode case before and after reshock. Additionally, the post-reshock, single-mode case appears to break up due to secondary instabilities, although the linear perturbation at the largest scale is somewhat separated from the scales at which this mixing is occurring.

Comparison between experimental data and amplitude growth model predictions

The Richtmyer's model which is suggested for the linear regime is discussed in chapter 1.2. Here, several nonlinear growth models are compared with experimental work of this study. Although at this low atwood number the dimensionless time scale ($\tau = kv_0t$, v_0 is the initial growth rate after shock hits the interface) is in the early nonlinear regime, measurements from these experiments can still be compared to nonlinear growth models. Figure 4.6 is a

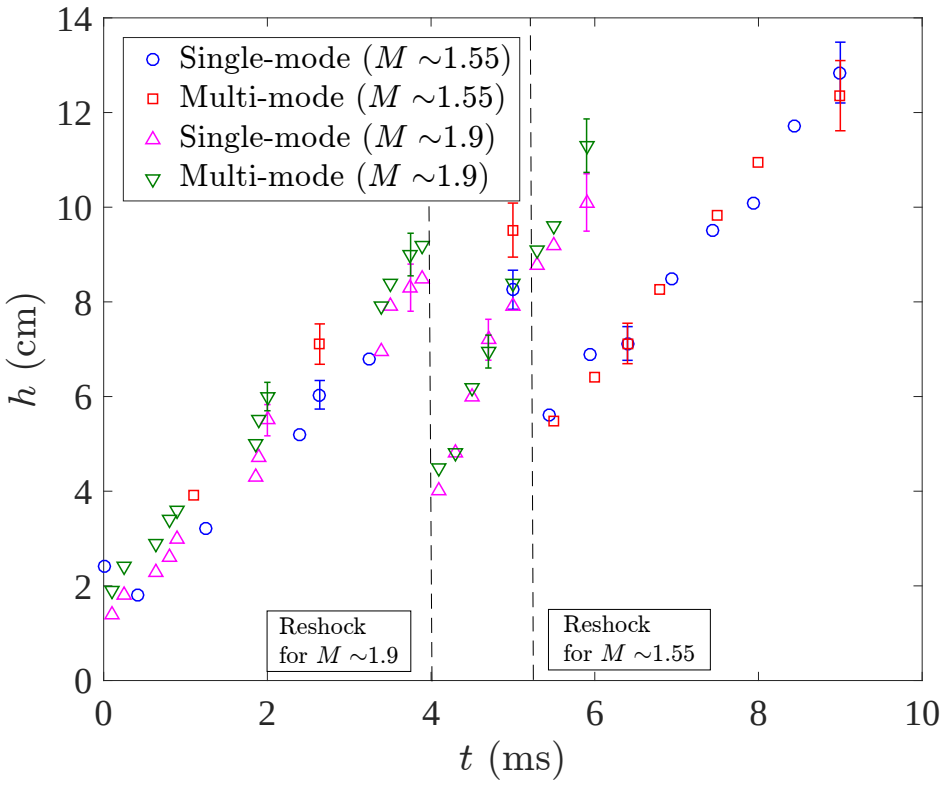

Figure 4.5: Comparison of overall mixing width (amplitude (h)) of the interface after incident shock and after reshock for single and multi-mode initial conditions at both $M \sim 1.55$ and $M \sim 1.9$. Error bars indicate the statistical error at times that larger ensembles of simultaneous PLIF/PIV were collected. Data without error bars are from single experiments.

plot of dimensionless amplitude, or mixing width (5%-95% of concentration) relative to its initial value versus a dimensionless time scale defined by the initial growth rate for both $M \sim 1.55$ and $M \sim 1.9$ experiments. The experimental results are compared with several models. Based on Richtmyer's model, amplitude grows linearly with time (Richtmyer, 1960). The straight dotted line in Figure 4.6 is a modified version of Richtmyer's model for inclined interface which was discussed in chapter 2.3 (Equations 2.2 and 2.3). As mentioned before, the instability is in the linear regime as long as $kh \ll 1$. Therefore, in these experimental campaigns the instability should grow linearly before $\tau \sim 1$ and then subsequently nonlinear growth begins and curvature is present in the amplitude plot. The results in the early nonlinear stage after incident shock ($\tau \sim 1 - 2.4$) are compared with models developed by Zhang and Sohn (1997) and Sadot *et al.* (1998). Zhang and Sohn (1997) proposed their analytic solution in two different forms: nonlinear asymptotic (power series) and a Padé approximation. The first two terms of the power series (second order) are used to evaluate the solution, which is shown by a red dash-dot line in the figure. This nonlinear power series is given as

$$v = v_0(1 - (h_0k)v_0kt + (A^2 - 1/2)v_0^2k^2t^2 + O(h_0k)^5), \tag{4.1}$$

where v is the overall growth rate. One can obtain a solution for mixing width by integrating this equation, which yields

$$h = v_0(t - 1/2h_0k^2t^2v_0 + 1/6(2A^2 - 1)k^2t^3v_0^2 + tO(h_0k)^5). \tag{4.2}$$

Since the power series is truncated at second order, this solution shows good agreement only at very early time. Similar behavior was observed by Collins and Jacobs (2002), who also compared their experimental results with the nonlinear second order form of this model.

The Padé approximation proposed by Zhang and Sohn (1997) for their power series can

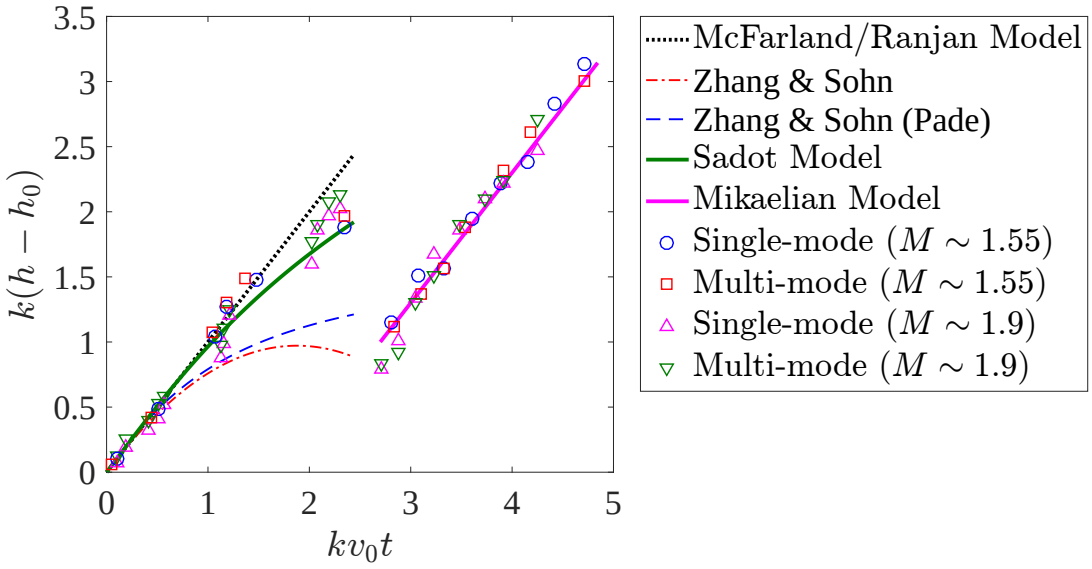

Figure 4.6: Nondimensional amplitude as a function of nondimensional time to compare analytical models with experimental data.

be computed as

$$v = \frac{v_0}{1 + v_0 h_0 k^2 t + max\{0, h_0^2 k^2 - A^2 + 1/2\} v_0^2 k^2 t^2}, \tag{4.3}$$

which again is integrated with respect to time to yield amplitude, which is given by

$$h = \frac{2tan^{-1}\left[\frac{k(2h_0^2k^2tv_0 + h_0 + (1-2A^2)tv_0)}{\sqrt{3h_0^2k^2 - 4A^2 + 2}}\right]}{k\sqrt{3h_0^2k^2 - 4A^2 + 2}}. \tag{4.4}$$

It should be noted that in the case of this experiment $h_0^2k^2 - A^2 + 1/2 > 0$ in the equation 4.3. This approximation, which is shown by a blue dashed line, shows better agreement with the experimental data than the truncated approximation of the power series, however it also diverges from the data at late time.

The last model which is compared with experimental data before reshock is Sadot's model (Sadot *et al.*, 1998), which is defined for small atwood numbers by

$$v_{b/s} = \frac{v_0(1 + v_0 kt)}{1 + (1 \pm A)v_0 kt + [(1 \pm A)/(1 + A)]v_0^2 k^2 t^2}. \tag{4.5}$$

where the upper (lower) sign ($\pm$) applies to bubbles (spikes) and $v = \frac{v_b+v_s}{2}$. Therefore, the amplitude of bubbles and spikes at low atwood number are computed from integration as

$$h_b = \frac{1}{2k}\left[log((A+1)\tau + \tau^2 + 1) - \frac{2(A-1)tan^{-1}[\frac{A+2\tau+1}{\sqrt{-A^2-2A+3}}]}{\sqrt{-A^2-2A+3}}\right], \tag{4.6}$$

$$h_s = \frac{1}{2k}(A+1)\left[-\frac{log(-A^2\tau - A\tau^2 + A + \tau^2 + \tau + 1)}{A-1} + \frac{2\sqrt{A-1}tan^{-1}[\frac{\sqrt{A-1}(A+2\tau+1)}{\sqrt{-A^3-A^2-3A-3}}]}{\sqrt{-A^3-A^2-3A-3}}\right], \tag{4.7}$$

where $\tau = kv_0t$. The solid green line in Figure 4.6 corresponds to Sadot's model ($h = \frac{h_b+h_s}{2}$), which yields the best fit to the experimental data before reshock.

After reshock the growth is compared to the model of Mikaelian (1989) intended for early stages of evolution after reshock passage. This model is given by

$$v_{rs} = C_M A \triangle u, \tag{4.8}$$

where C_M is found to be 0.28 for $M \sim 1.55$ and 0.3 for $M \sim 1.9$ to capture the experimental data. $\triangle u$ and A are jump velocity and atwood number after reshock. Growth of the interface is captured accurately by this model in the early evolution after reshock.

4.1.3 Mixing Layer Thickness, and Mixed-Mass

At any time, the mixing width only denotes the extent of the instability, and not the modal content or the scalar mixing. An additional length-scale, termed 'mixing layer thickness (δ)', is defined in order to highlight the mixing dynamics below the large scale in the flow and emphasize the effect of the initial condition. This definition considers the average streamwise thickness of the mixed material in the range $4Y_{N_2}Y_{CO_2} > 0.84$ (chosen to consider highly mixed material). Here, Y_{N_2} and Y_{CO_2} are mole fraction of light and heavy

gases at each spanwise location, and δ is calculated as

$$\delta = \frac{\int\int 4Y_{N_2}Y_{CO_2}dxdy}{\int dy}. \tag{4.9}$$

Figure 4.7 shows the evolution of δ with nondimensionalized time. It must be noted that the multi-mode interface starts with a higher initial δ than the single-mode interface. As expected from the observations in Figure 4.4, the δ of the multi-mode interface consistently grows faster than the single-mode case before reshock at both Mach numbers. Further, the $M \sim 1.9$ case has a slightly higher mixing layer thickness than the $M \sim 1.55$ case, owing to the stronger growth and mixing in the former. After reshock, this quantity is not sensitive to the additional modal content of the multi-mode interface, largely due to the interface compression from reshock, as all the cases continue to evolve similarly. Mixing layer thickness is also used in section 4 for the investigation of mixing transition, as this is considered by the authors to be a more accurate indicator of the mixing dynamics in the flow than the mixing width defined before.

Mixed-mass, which is a measure of how much mixed product exists in the flow, can also be considered to further quantify the actual mixing of the gases at each evolution time investigated. The calculation of mixed-mass assumes that material is distributed uniformly at sub-pixel scales. An important feature of this quantity is that it is a monotonically increasing quantity, and unlike mixing width and mixing layer thickness, does not decrease with the passage of reshock (Zhou, 2017; Zhou, Cabot, and Thornber, 2016). Also, the mixed-mass calculation does not include the entrained, but unmixed fluid. The mixed-mass ($\mathscr{M}$) is calculated as

$$\mathscr{M} = \int 4\rho Y_{N_2}Y_{CO_2}dV. \tag{4.10}$$

Mixed-mass is shown at various nondimensional times in Figure 4.8. A linear trend is observed for all cases before reshock, and, similar to mixing layer thickness, the multi-

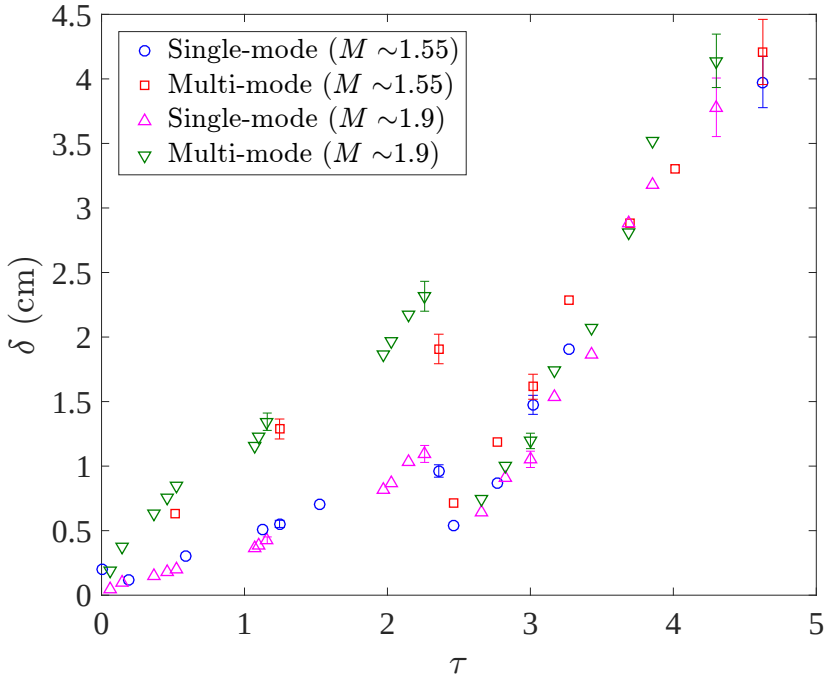

Figure 4.7: Evolution of integral mixing layer thickness (δ) in nondimensional time, τ for all cases.

mode case has a higher growth rate of mixed-mass compared to the single-mode case. The single- and multi-mode cases at high Mach have slightly higher mixed-mass compared to low Mach cases before reshock at the same nondimensional times. Post-reshock, however, unlike the trends in mixing layer thickness, mixed-mass is noticeably higher for the $M \sim 1.9$ case, due to the larger density jump, particularly with reshock. This observation (of similar mixing layer thickness but higher mixed-mass in the post-reshock $M \sim 1.9$ cases) implies that the rate of entrainment is similar between the two Mach numbers, while the rate of molecular mixing is higher in the high Mach case. This mixing paradigm will be further explored in the following section.

4.1.4 Mixedness

Mixedness profiles are a measure of how well entrained fluid is molecularly mixed. If none of the entrained fluid is mixed molecularly (immiscible case) the mixedness is zero, but if

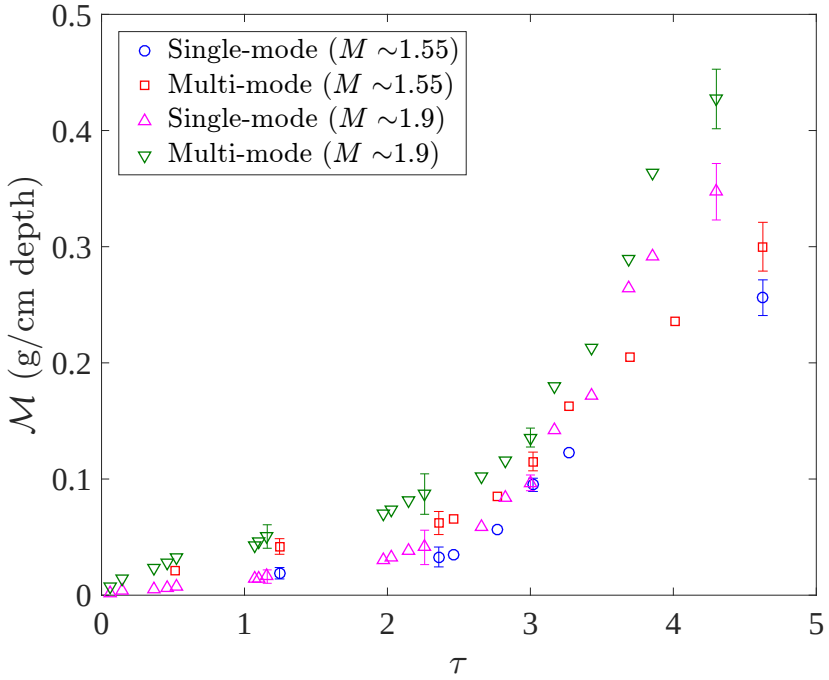

Figure 4.8: Evolution of integral mixed-mass ($\mathscr{M}$) in nondimensional time, τ for all cases.

all the entrained fluid is molecularly mixed (a pure substance, locally homogeneous) then mixedness is one. To compute the fraction of entrained material that is molecularly mixed, mixedness, θ is calculated as

$$\theta = \frac{\int \overline{X(1-X)}dx}{\int \overline{X}\,\overline{(1-X)}dx} \tag{4.11}$$

where heavy fluid has a mole fraction of

$$X = \frac{\rho - \rho_1}{\rho_2 - \rho_1}. \tag{4.12}$$

The evolution of this average mixedness in the mixed region at various nondimensional times is shown in Figure 4.9. The average mixedness initially decreases after the initial shock due to the stretching of the interface and the high rate of entrainment as the two fluids undergo penetration within each other. Before reshock, the difference in mixedness between single-mode and multi-mode interfaces is more pronounced at higher Mach number. Further, due to a higher amount of entrained (but unmixed) fluid, the mixedness is

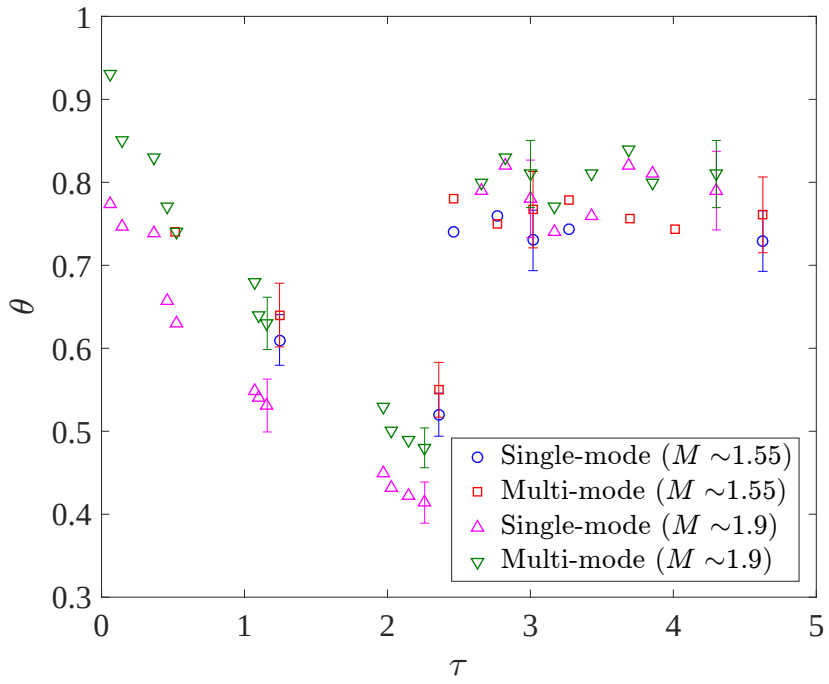

Figure 4.9: Evolution of integral mixedness (θ) in nondimensional time, τ for all cases.

observed to be lower for the high Mach number case than the low Mach number case, despite a higher amount of mixed material in the former. Similar behaviour was observed by Orlicz, Balasubramanian, and Prestridge (2013) in the gas curtain experiment at early time after incident shock. Weber *et al.* (2014) also observed similar behaviour for a higher Mach number at early time in a comparable metric to mixedness.

Contrarily, after reshock, higher mixedness is observed in the higher Mach case; which is consistent with the aforementioned observations that the overall growth (mixing width) and mixing layer thickness were similar between the two Mach numbers, but that the amount of mixed-mass was higher in the high Mach case after reshock. Mixedness is similar between the single and multi-mode cases after reshock, as was also seen with δ in figure 4.7.

There has been much discussion of how the entrainment (due to pure fluid entering the mixing zone on either end) and molecular mixing rates might balance as the interface approaches a nonlinear state. Asymptotic values at late time have been proposed. In

the current work, the interface at late time after reshock is beginning to display nonlinear behaviour and the value of mixedness is fairly constant. It appears that the interface is approaching an asymptotic value; and it is likely that the interface is approaching the asymptotic state. The late time value of mixedness for the low Mach number case is 0.76±0.04 and for the high Mach number case is 0.82±0.04. Zhou, Cabot, and Thornber (2016) found an asymptotic value (~ 0.8) for similar Atwood and Mach number, and Tritschler *et al.* (2014) found a similar asymptote value of 0.85 for $M = 1.5$ and higher Atwood number, which are in reasonable agreement with the current work. Orlicz, Balasubramanian, and Prestridge (2013) observed that the average asymptotic value increases with increasing Mach number, consistent with the findings of the current work, however, the final value was found to be $0.94 - 0.97$ for the different Mach numbers.

To investigate the effect of initial condition, it is useful to look at the profile of the spanwise-average of mixedness at various streamwise locations along the mixing region. Figure 4.10 shows this at two times before and two times after reshock for both $M \sim 1.55$ and $M \sim 1.9$ cases. While the overall trend is similar between the two interfaces, the multi-mode case shows much higher mixedness before reshock at both Mach numbers. Additionally, the spike side ($x < 0$) is more mixed after reshock while entrainment is outpacing molecular mixing on the bubble side ($x > 0$) at $M \sim 1.9$, while flow is more mixed on the bubble side at lower Mach number ($M \sim 1.55$) at latest time after reshock.

The effect of Mach number on the mixedness can be seen in figure 4.11. Before reshock, though the overall trend is similar, mixedness in the higher Mach case is slightly lower than the lower Mach case as was seen in the integral measurement in figure 4.9. After reshock there is a significantly higher amount of entrained and mixed fluid in the spike region ($x < 0$) of the high Mach case for both single and multi-mode conditions. This trend is reversed, however, in the $M \sim 1.55$ case where the bubble region ($x > 0$) shows higher θ. This behaviour is due to higher penetration of the spike to the core of the flow and subsequent breakdown of scales in the higher Mach case, where the core of the flow is more

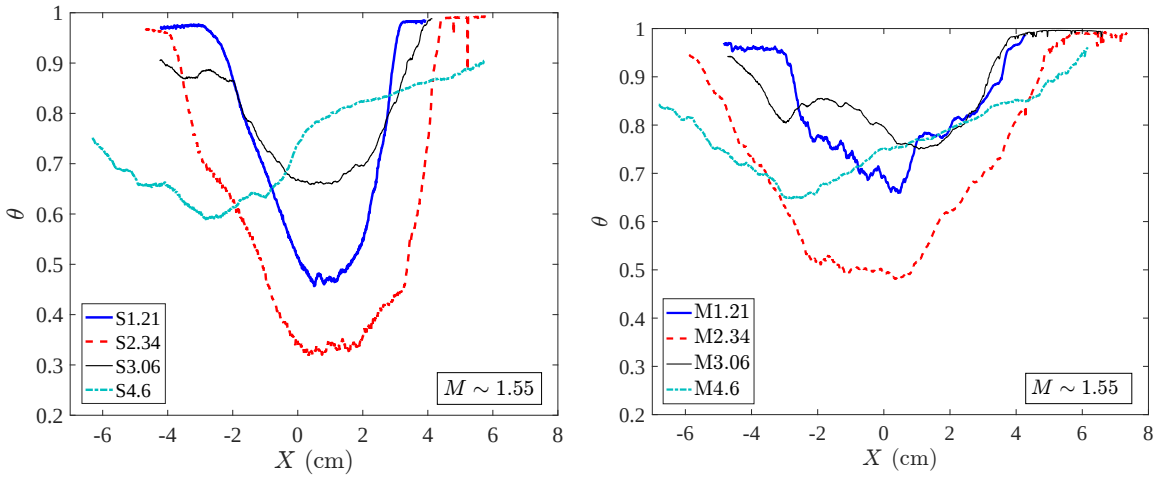

(a) Single-mode case at $M \sim 1.55$ *(b)* Multi-mode case at $M \sim 1.55$

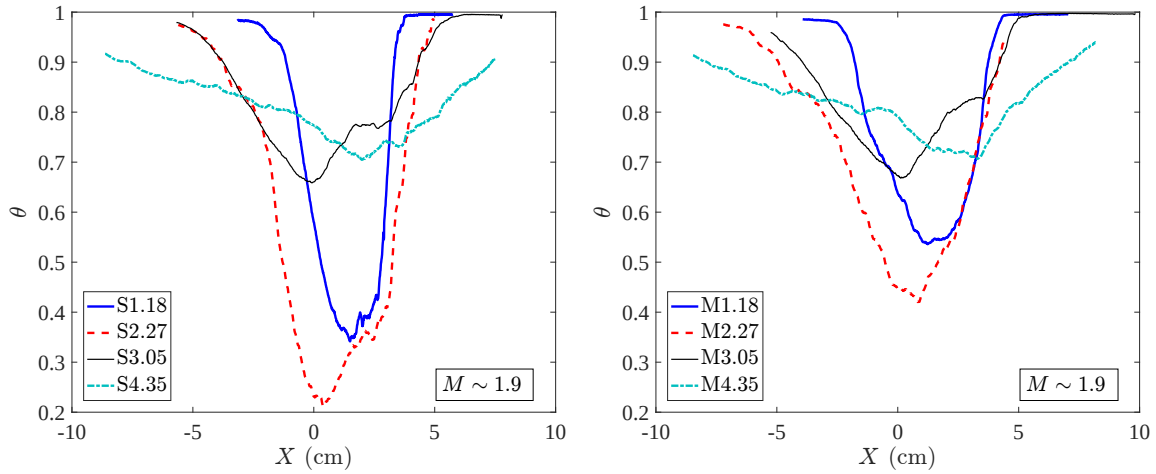

(c) Single-mode case at $M \sim 1.9$ *(d)* Multi-mode case at $M \sim 1.9$

Figure 4.10: Effect of initial condition on temporal evolution of Mixedness profiles in the streamwise direction before and after reshock at (a,b) $M \sim 1.55$ and (c,d) $M \sim 1.9$ for the (a,c) single-mode (S) and (b,d) multi-mode (M) cases. X is distance from centre of mass.

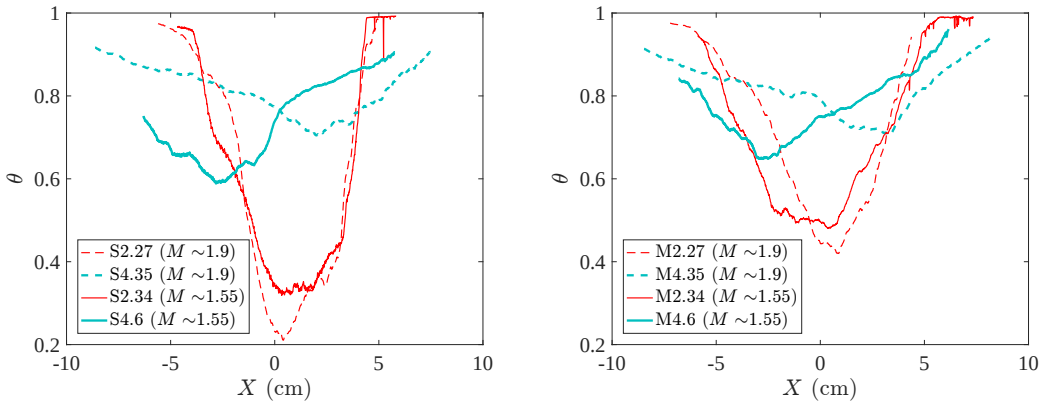

(a) Single-mode case *(b)* Multi-mode case

Figure 4.11: Effect of Mach number on temporal evolution of Mixedness profiles in the streamwise direction before and after reshock at for (a) single-mode (S) and (b) multi-mode (M) cases. X is distance from centre of mass.

mixed. Regarding the effect of Mach number on mixedness for different initial conditions, the spatial distribution of the mixedness is not changed by the additional perturbations of the multi-mode initial condition, but the magnitude is still noticeably larger before reshock and slightly larger after reshock for the multi-mode case. This suggests that the effects of Mach number and initial condition on this measurement could be independent of each other.

4.1.5 Density Self-Correlation

The density-specific volume correlation, also referred to as the density self-correlation (DSC), is the correlation between density fluctuations and specific volume fluctuations ($b = -\langle\rho'(1/\rho)'\rangle$). In the Boussinesq limit, it is very similar to the density variance. This is an important statistic in closure of many turbulence models, and is typically termed the b parameter in the Besnard *et al.* (1992), or BHR model. The parameter has been thoroughly investigated in previous studies such as Balakumar *et al.* (2012). These works can be referred to for a more thorough analysis of DSC and the effect of the averaging choice in computing the same. Particularly in spatially inhomogenous flows, specific volume fluctuations computed via spatial averaged quantities show an apparent increase in the DSC

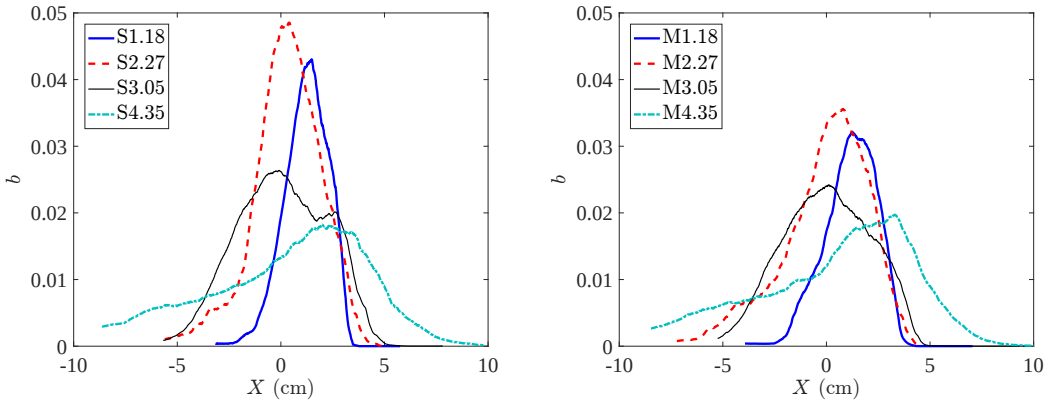

(a) Single-mode case *(b)* Multi-mode case

Figure 4.12: Temporal evolution of density self-correlation profile (DSC, b) along the streamwise direction before and after reshock with fluctuations computed from spanwise averaging method at $M \sim 1.9$ for the (a) single-mode (S) case and (b) multi-mode (M) case. X is distance from centre of mass.

values, when compared with the fluctuations with respect to the ensemble average. Furthermore, the information about the spatial variance of density is already contained within mixedness (Livescu and Ristorcelli, 2008), and the two variables embody similar information about the flow. Figure 4.12 highlights this similarity between trends of the profiles of mixedness and the DSC, when fluctuations are computed from spanwise averaged quantities. It shows that for both single- and multi-mode cases after incident shock, the DSC increases as the interface stretches, causing sharpening in the gradient of density. After reshock, the flow evolves to a more homogeneously mixed state, which is indicated by the decrease in DSC with time after reshock.

In the present work, the DSC is also calculated from the ensemble averaging method of calculating fluctuations. Because of the coupling between the density and velocity fields, density fluctuations are selected to the flux of mass (the velocity of the mass flux will be described in detail later) which drives the production of Reynolds stress in the BHR model. The production term of the Reynolds stress from the BHR model (Schwarzkopf *et al.*, 2016)

is:

$$[a_i\overline{P}_{,j} + a_j\overline{P}_{,i}] - \overline{\rho}[\widetilde{R}_{ik}\widetilde{u}_{j,k} + \widetilde{R}_{jk}\widetilde{u}_{i,k}] \tag{4.13}$$

where a is the mass flux. In this method, the DSC represents the mixing which is occurring in the flow, whereas mixedness indicates the portion of entrained fluid which has already mixed. This method results in a DSC field, which can then be spanwise averaged to yield a profile. Figures 4.13 and 4.14 show the profiles and ensemble averaged fields, respectively, of the DSC, with this method. In the low Mach number case ($M \sim 1.55$), the profiles of the DSC are similar at $\tau = 1.21$, because the interface has just been compressed by the incident shock. This compression confines the area over which the density can fluctuate while the interface stretching is sharpening the gradients. However, the mixing is slightly higher in the multi-mode case. At $\tau = 2.34$ the profiles are the most different, as the single-mode case shows localized peaks in mixing at shear-driven roll-ups, whereas the multi-mode case shows mixing throughout the mixing layer due to increased mode merging effects. Both cases show similarly high levels of mixing at $\tau = 3.06$ due to the recent forcing of the reshock wave. However, at $\tau = 4.6$, the DSC is higher for the multi-mode case in the spike tip and bubble regions, which is evidence that turbulent mixing mechanisms in those regions persist even after the forcing of reshock has ceased. The mixing intensity at $\tau = 4.6$ after reshock is commensurate with the asymptotic theory of mixedness in that as more fluid is injected into the mixing region which is growing nonlinearly, density fluctuations act in synergy with strong velocity fluctuations, which describes the motivation for equation 4.13.

For the high Mach number case ($M \sim 1.9$), the similarity between the single-mode and multi-mode cases is evident. A double-peak at $\tau = 2.27$ (late time before reshock) can be seen in the single-mode case and corresponds to the more organized structures in the spatial field. A slightly larger tail is also seen at $\tau = 4.3$ (late time after reshock) in the single-mode case due to a secondary spike that commonly occurs at the center of the field. As a result of the variability in the multi-mode case, this tail is slightly smaller.

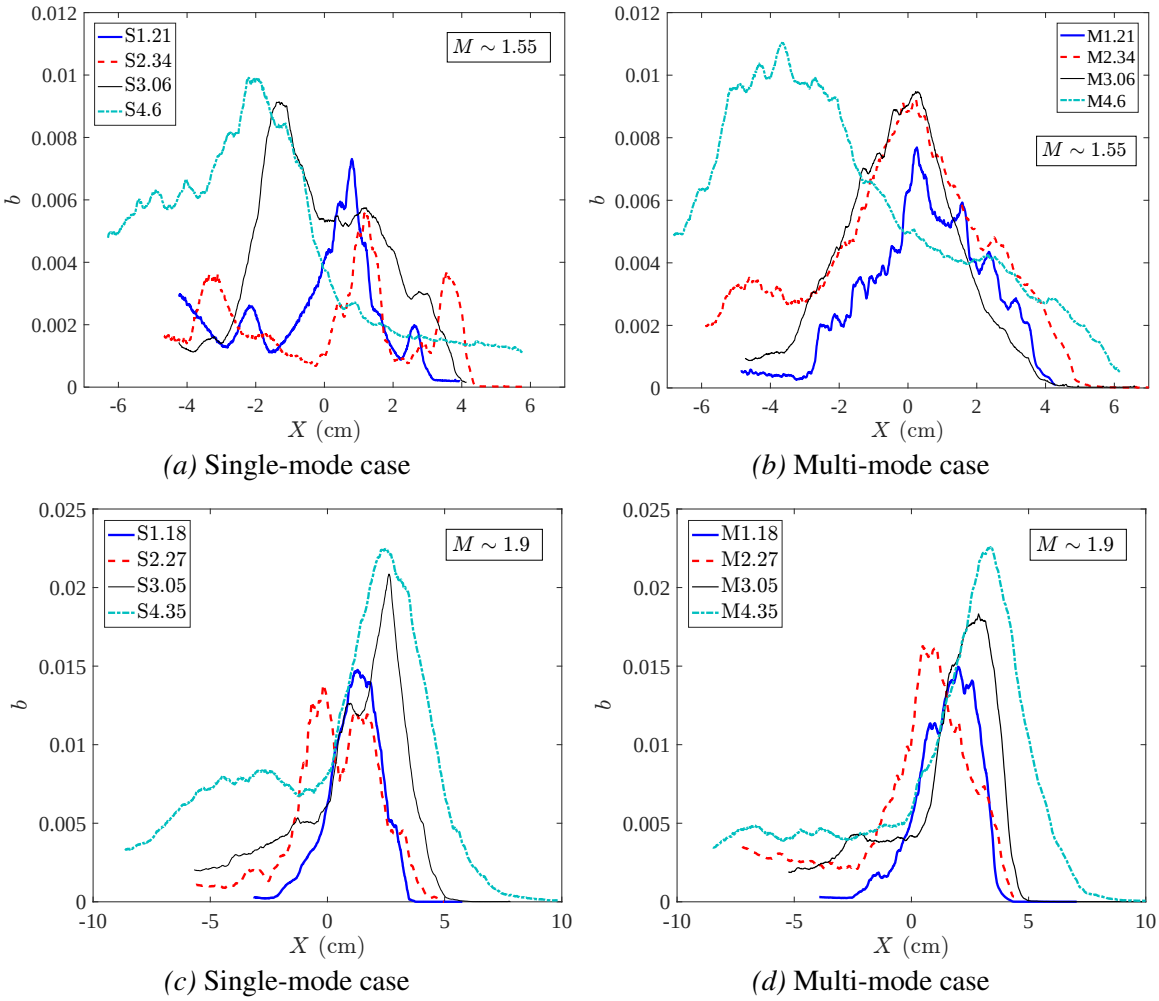

(a) Single-mode case *(b)* Multi-mode case

(c) Single-mode case *(d)* Multi-mode case

Figure 4.13: Effect of initial condition on temporal evolution of the density self-correlation profile along the streamwise direction before and after reshock where fluctuations are computed from the ensemble averaging method at (a,b) $M \sim 1.55$ and (c,d) $M \sim 1.9$ for the (a,c) single-mode (S) and (b,d) multi-mode (M) cases. X is distance from centre of mass.

Although the intensity observed in the fields is similar before and after reshock, the peak of the DSC profile increases after reshock because the active mixing region on the bubble side is oriented parallel to the spanwise direction.

Figure 4.14 shows the DSC fields from which the profiles in figure 4.13 are calculated. The value of this visualization method is emphasized, by first noting that although the spanwise-average of the DSC is nearly identical between the single-mode and multi-mode cases, the fields show striking differences in structures spatially. The variability of the multi-mode case results in larger areas of more diffuse fluctuation intensity, while the

consistency of the single-mode case yields small, concentrated regions where fluctuations display greater variance in the ensemble. This is true before and after reshock.

For a clearer comparison between Mach numbers, figure 4.15 shows just one time before reshock and one time after reshock of the $M \sim 1.55$ and $M \sim 1.9$ cases. There is a significantly greater DSC for the high Mach case before and after reshock, and there is a reversal in the side of the flow that contains the most mixing. This observation and trend-reversal was also seen in the mixedness profiles after reshock in figure 4.9. Furthermore, the difference between single and multi-mode is not very striking for the $M \sim 1.9$ case. The low Mach case is also very similar after reshock. Before reshock, however, there is a significant difference where the single-mode interface has three peaks which are much more distinct. Overall, the increase in Mach number increases the mixing before and after reshock, and smears regions of intense mixing into each other before reshock.

In addition to the DSC itself, analysis of each term of the DSC budget can yield insights into the mechanisms that are affecting the local rate of change of the variable (Tomkins *et al.*, 2013). The following is one form of the evolution equation (Besnard *et al.*, 1992), which shows this relationship and numerically identifies each term of interest.

$$\frac{\partial b}{\partial t} + \widetilde{U}_j b_{,j}[1] = 2a_j b_{,j}[2] - 2a_j(1+b)\frac{\overline{\rho}_{,j}}{\overline{\rho}}[3] + \overline{\rho}\left(\frac{\langle u_j'\rho'(1/\rho)'\rangle}{\overline{\rho}}\right)_{,j}[4] + 2\overline{\rho}\langle(1/\rho)'\nabla.u'\rangle[5] \tag{4.14}$$

The numbers in square brackets ($[1-5]$ refer to various terms in the equation. Of particular interest are terms two through four, since term 1 is advection and term 5 is negligible compared to the others. The individual terms were first measured experimentally by Tomkins *et al.* (2013), where the fluctuations were calculated from spanwise averaging method to compare with simulations. Contrarily, figure 4.16 shows the spanwise averaged profiles of the field calculated from ensemble averaged means for each term of interest $[2-4]$ at the latest time after reshock. The ensemble fields themselves are shown subse-

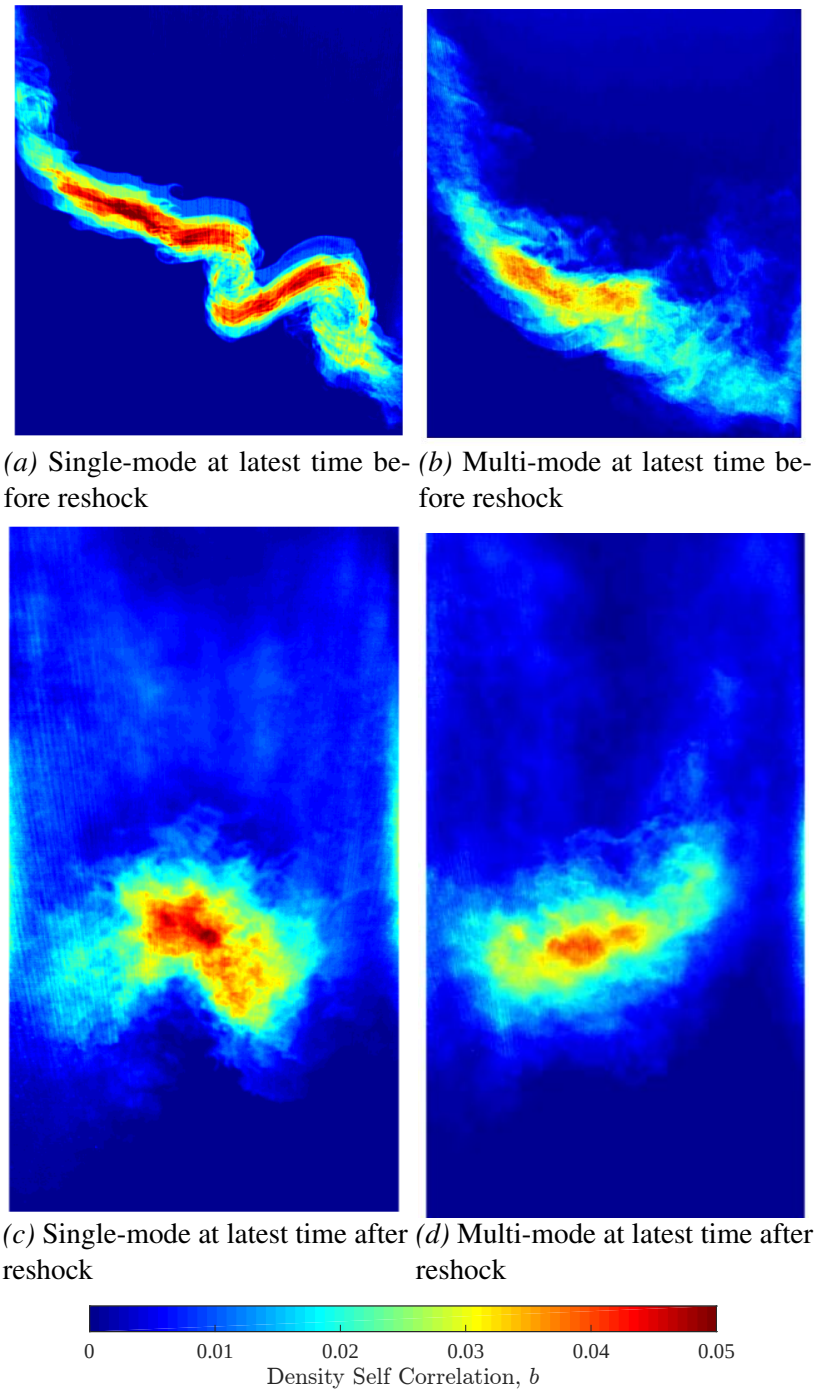

(a) Single-mode at latest time before reshock

(b) Multi-mode at latest time before reshock

(c) Single-mode at latest time after reshock

(d) Multi-mode at latest time after reshock

Figure 4.14: Fields of density self-correlation (a,b) before and (c,d) after reshock at $M \sim 1.9$ for the (a,c) single-mode (S) case and (b,d) multi-mode (M) case.

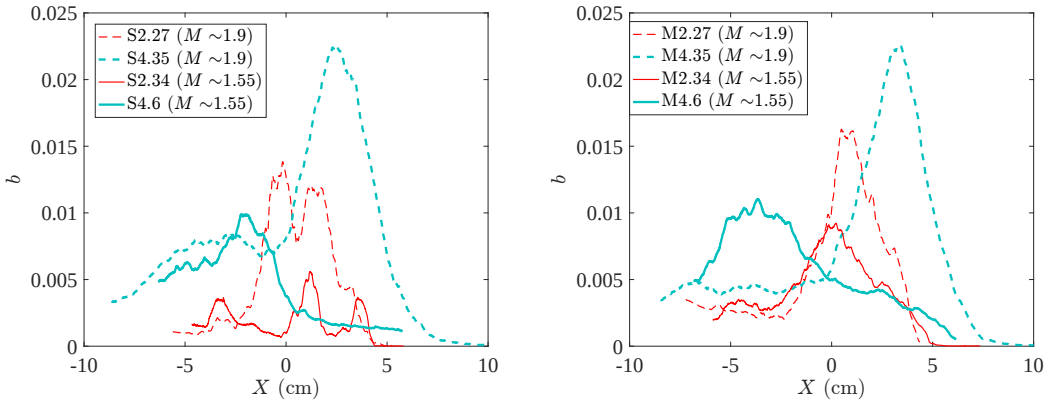

(a) Single-mode case *(b)* Multi-mode case

Figure 4.15: Effect of Mach number on temporal evolution of density self-correlation profile along the streamwise direction before and after reshock computed from ensemble averaging method for the (a) single-mode (S) case and (b) multi-mode (M) case. X is distance from centre of mass.

quently in figure 4.17. Comparing the two initial conditions, the single-mode case shows sharper profiles indicating greater gradients in certain areas of the flow, while the multi-mode case has smaller maxima and is more evenly distributed. Otherwise, the morphology of the profiles is similar between the two cases. Both cases have a peak in the sum of terms which closely represents the overall rate of change and additional local peaks throughout the mixing region. Terms 2 (convection) and 4 (transport) undergo changes in sign. The more relevant observation is that the transport term changes from positive, to negative, and back to positive, generally, with small undulations. This is more obvious in the multi-mode case. This implies that the transport term is working to increase the DSC near the edges of the mixed region and transporting it from its center. Term 3 shows that production is higher inside the mixing region with a bias towards the bubble side ($x > 0$).

Figure 4.17 provides further details on the mechanics of the DSC. While the main observable differences in spanwise-averaged profiles between the single- and multi-mode cases were in magnitude, the fields of DSC terms provide further illumination of physical behaviour of the flow. The fields in figure 4.17 highlight a difference in the shape of the spatial distribution more obviously. Also, the DSC term fields are observed to

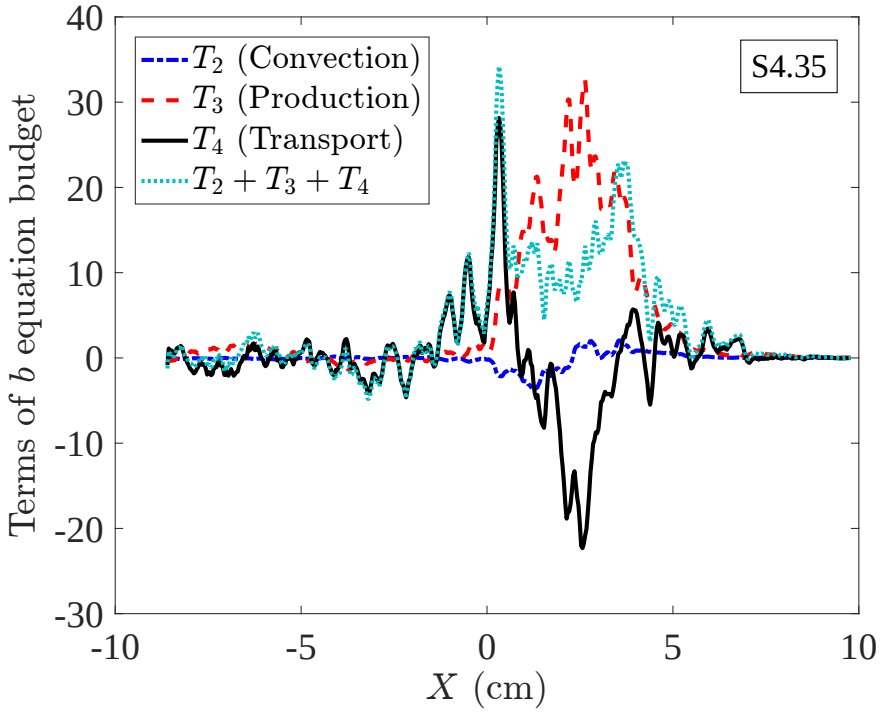

(a) Single-mode case

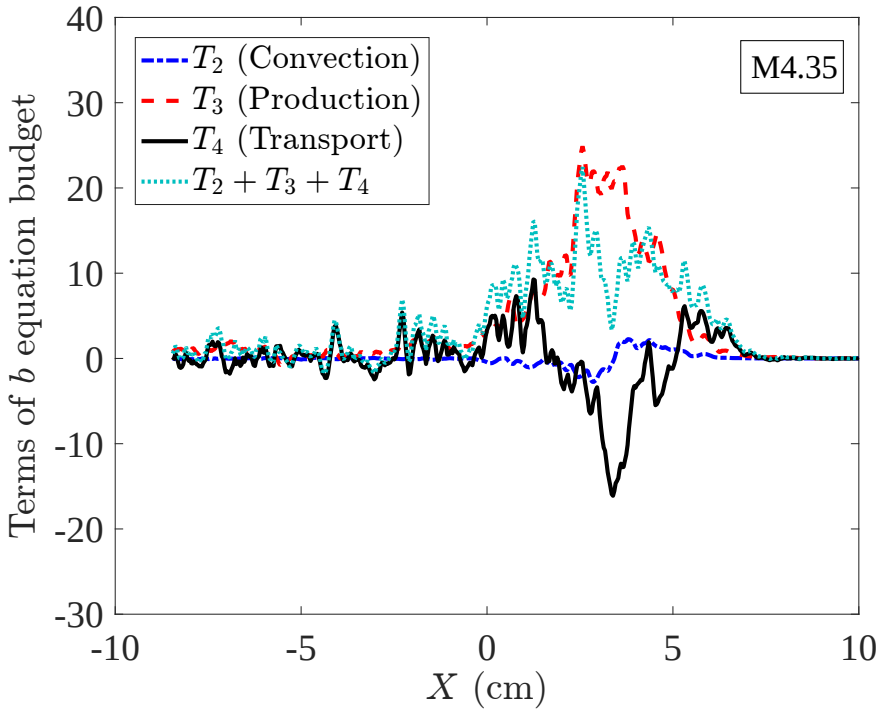

(b) Multi-mode case

Figure 4.16: Comparison of the relative magnitudes of term 2 (convection), term 3 (production) and term 4 (transport) in the DSC evolution equation at the latest time after reshock (τ = 4.35) for both (a) single-mode and (b) multi-mode cases at $M \sim 1.9$.

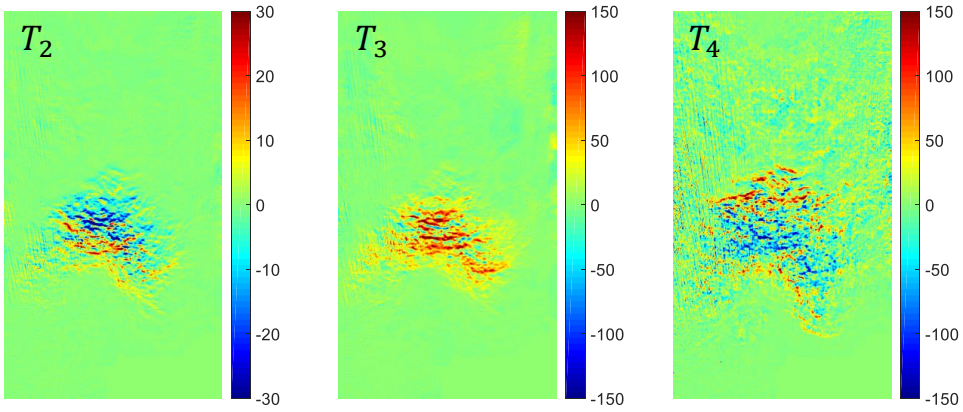

(a) Single-mode case at latest time after reshock

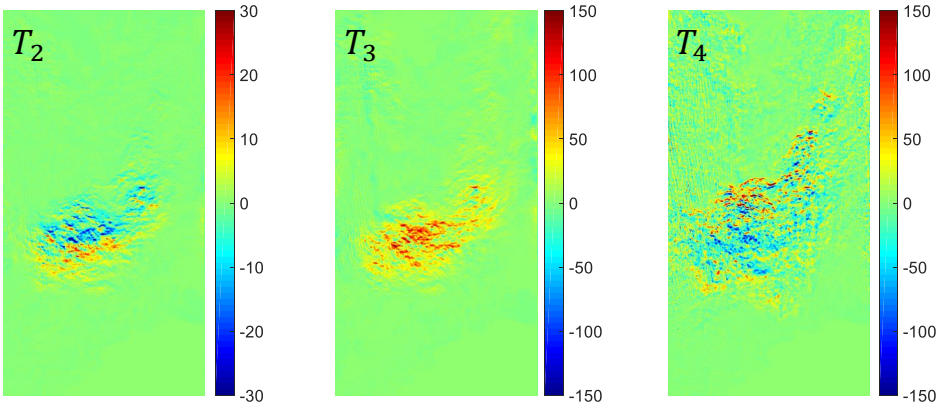

(b) Multi-mode case at latest time after reshock

Figure 4.17: Comparison between fields of different terms in the DSC evolution equation at the latest time after reshock ($\tau = 4.35$) for both (a) single-mode and (b) multi-mode cases at $M \sim 1.9$.

have slightly more intense regions and more variation in sign than was observable in the spanwise-averaged plots in which these features lead to lower values.

Between the single- and multi-mode cases, the consistently different morphology of the multi-mode interface is observable in all of the fields of these terms. All of the terms are observed to be slightly more intense in the single-mode case due to the higher level of consistency (low variance) of the interface shape, placing fluctuations in concentrated areas along the interface, while the multi-mode case terms are more diffuse due to higher variability/nonlinearity of the interface.

Regarding the relative contribution of each term to the total budget, term 2 (convection), which is characterized by turbulent mass-flux, a, is of much lower magnitude than the

production and transport terms. This term is observed to decrease the DSC on the light gas side, but to increase it on the heavy gas side of the mixing region.

It is observed that production term 3, primarily affects the interior of the mixing region. This term is mostly positive in both cases; however, the single-mode case is more intense and displays small pockets of negative production, which are likely to be damped out due to the more random interface of the multi-mode case. The transport term (4) is similar in magnitude to production, but the configuration of the two terms (3 and 4) is complementary; while the DSC is produced in the interior of the mixing region, it is transported out (negative values of term 4) of the center of the mixing region to the edges. This finding should be considered in light of current discussion of the asymptotic value of mixedness suggesting a connection between the mixing dynamics in the interior of the mixing region and the influx of pure fluid at the edges which propagates a balance between entrained and molecularly mixed fluid at late times.

4.1.6 Vorticity and Circulation

Resolving the vorticity field and flow circulation are two key aspects of a velocity field analysis. Using the PIV methods outlined earlier, the velocity fields were resolved using TSI INSIGHT 4G^{TM} in order to provide a quantitative analysis of the flow field. Any holes in the velocity fluctuation field were filled via interpolation using nearby values. The field was subsequently filtered using a median filter with a bin of 11-by-11 vectors in order to smooth spurious noise induced by small gradients in the fields and allow for a more accurate analysis.

Concerning vorticity and circulation, two separate methods were used in order to verify the procedures and results. First, vorticity was computed by taking the curl of the 2D velocity vector field ($\omega = \boldsymbol{\nabla} \times V$) at each point in the field. This method is identical to the process used in Reilly *et al.* (2015). Next, for comparison and verification, vorticity was back-calculated from circulation: a local circulation for each point in the velocity

fluctuation field was found using

$$\Gamma(t) = \int_C \vec{V} \cdot d\vec{r}, \tag{4.15}$$

where the velocity field is integrated around a closed interval C, which encompasses the entire cropped region of the velocity field. This method is similar to the one used in Schilling, Latini, and Don (2007) and Weber *et al.* (2014), which was shown to have good agreement with the Samtaney–Zabusky model, but the encompassing region of C is altered. The above integral was broken up into the sum of many small integrals with regions of C that encompass individual points in the velocity field. The velocity differences along each line segment making up the small area S (with a size of 2x2 vectors) result in a "local circulation" about the center of each region. The total circulation is then the sum of these "local circulations" calculated from individual points in the velocity fluctuation field. From this point the following relation is used to find the vorticity

$$\Gamma(t) = \int \int_S \vec{\omega} \cdot d\vec{S}. \tag{4.16}$$

Thus, by dividing each local circulation value by the area, dS, of the encompassing region C, a vorticity field is generated from the circulation of the flow field. Evaluating the integral in this way allows for the size and shape of the region C to be selected to achieve further smoothing in the vorticity field, if desired. The results of these two methods produce vorticity fields that are essentially identical.

In addition, the density gradients are analyzed in conjunction with vorticity. The PLIF resolution is not sufficient to show the exact scalar dissipation rate with $Sc \approx 1$; the Batchelor scale, $\lambda_b \approx \lambda_k$ ($resolution \approx 7\lambda_b$). An alternative method of visualizing density gradients is a simulated Schlieren technique (Quirk and Karni, 1996) which is shown in Figure 4.18 with the vorticity overlaid at $M \sim 1.55$. This result from simultaneous measurements provides a description of how well the small scale features of the flow (scalar

and velocity gradients) are connected. The simulated Schlieren field is derived from the density field by:

$$\Phi(x,y,t) = exp\Big\{ -\kappa \frac{|\Delta\rho|}{|\Delta\rho|_{max}} \Big\}, \qquad \kappa = \begin{cases} 100 & \xi < 0.75 \\ 20 & \xi > 0.75 \end{cases}, \tag{4.17}$$

where ξ is mole fraction. Sharper gradients appear darker in the images. Most of the mixing region in single-mode case has sharper gradients at each experimental time. The gradients appear sharper towards the spike side (light gas side, left) of the interface at all times as the pure heavy gas is injected into the light gas and the resultant shearing strips off mass as it mixes. The multi-mode case appears to break down to smaller scales much more quickly than the single-mode case, but both appear to have become much more disorganized at the latest time after reshock.

The evolution of the vorticity field at $M \sim 1.55$ is shown in Figure 4.18, red and blue represent positive and negative vorticity, respectively. Due to the misalignment of the pressure and density gradients, the baroclinic term results in vorticity deposition across the flow field, which in turn results in mixing and deformation of the interface. For the single-mode case, shown in the first column starting with Figure 4.18(a), the incident shock wave passing from light to heavy gas creates strong negative vorticity across the interface. The magnitude of the vorticity immediately after incident shock compares well with the analytical model of Weber, Cook, and Bonazza (2013) which gives approximately $0.9 \times 10^4 s^{-1}$. At $\tau = 2.34$ after incident shock, the vorticity deposited on the interface has caused the initial perturbations to grow in amplitude and form larger vortical structures, as seen in Figure 4.18(c). As the amplitude of the perturbation is larger than the IC and the density gradients are enhanced, it is expected that a larger amount of vorticity will be deposited as the reshock wave passes back from the heavy to light gas regions, leading to much higher levels of vorticity (Weber *et al.*, 2012). This can be seen in Figure 4.18(e), as the reshock wave passes through the interface, it deposits such a large amount of vorticity

that the majority of the field becomes positive. This reversal of the vorticity field is a result of the application of additional opposite-signed (now positive) baroclinic torque, and the interface itself begins to rotate in the opposite direction immediately after reshock. Furthermore, small pockets of negative vorticity are preserved even after reshock. The presence of positive and negative vorticities after reshock, seen in Figure 4.18(g), is a result of vorticity deposition on an interface with a much less unidirectional gradient. It is also apparent that, due to the more mixed state of the reshock initial condition ($\tau = 2.34$), there is a larger area of the flow over which vorticity is deposited.

For the multi-mode case, shown as a progression in the second column of Figure 4.18, the general physics is similar but key differences should be highlighted. In Figure 4.18(b), immediately following the incident shock wave, the complex nature of the multi-mode interface has already resulted in the deposition of positive vorticity even before reshock. In Figure 4.18(d), the vorticity has grown again, feeding the growth of the perturbations that serve as the initial conditions for the multi-mode reshock case. Figure 4.18(f) shows the vorticity field immediately prior to reshock and displays the anticipated deposition of positive vorticity due to the application of baroclinic torque. As expected, the deposition of vorticity in the multi-mode case results in higher amplitude positive vorticity post-reshock than in the single-mode case, due to the presence of positive vorticity pre-reshock. However, this figure displays a notable difference between the two cases, as although the amount of vorticity deposition is equivalent, its distribution is markedly different. In the single-mode case, the vorticity deposition occurs along the interface, as it closely follows its shape. Whereas, in the multi-mode case the distribution of vorticity deposited is broader and more diffuse. Lastly, it can again be seen from Figure 4.18(h) that by late time the vorticity becomes more widely deposited throughout the flow field, its amplitude grows, and the level of mixing increases.

Results from the circulation data can help to understand the vorticity field evolution, as the circulation is merely the result of vorticity deposition (Schilling, Latini, and Don,

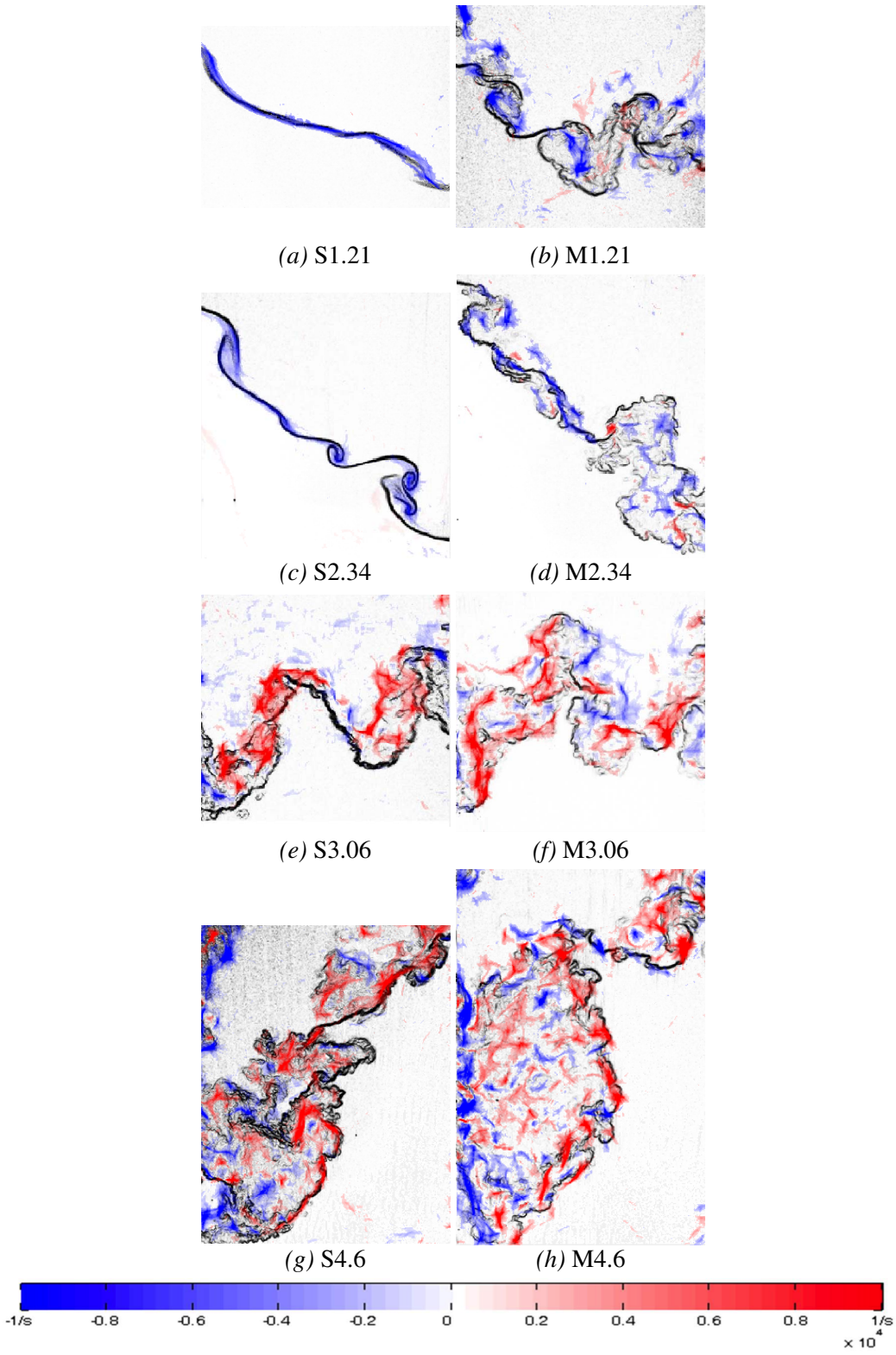

(a) S1.21 *(b)* M1.21

(c) S2.34 *(d)* M2.34

(e) S3.06 *(f)* M3.06

(g) S4.6 *(h)* M4.6

Figure 4.18: Vorticity evolution overlaid on simulated schlieren images for both cases at $M \sim 1.55$. S refers to single-mode case and M refers to multi-mode case.

2007). The positive, negative, and total circulation in the flow field at each time at $M \sim 1.55$ are displayed below in Figures 4.19(a–c). Due to the relation between vorticity and circulation, by comparing Figures 4.19(a) and 4.19(b), it can be confirmed that the negative vorticity components in the multi-mode and single-mode cases are of a greater amplitude than the positive components (for case S, positive circulation, and thus positive vorticity is essentially negligible). After the incident shock wave passes, both negative and positive circulation components can also be seen to increase very slightly, as was expected from the vorticity analysis. For both cases, the greatest increase in positive circulation comes immediately after reshock. This is to be expected as it corresponds to when the greatest amount of positive vorticity is deposited within the flow field. Comparatively, the greatest increase in negative circulation occurs as the reshocked interface perturbations grow. It should also be noted that the growth rate of vorticity and circulation (both positive and negative) post-reshock, between 5 ms and 6.4 ms, is greater in the single-mode case than in the multi-mode case, yet total circulation shares a very comparable trend for both.

4.1.7 Analysis of Vortex Sheet Roll-ups

In this section, the effect of different shock strengths on the distribution of vortex-roll-up features along the interface is investigated. This is an important topic, but has received limited attention thus far (Zabusky, 1999). The latest time before reshock for the single-mode interface at both Mach numbers was chosen to analyze the vorticity concentration and roll-up features. This case was chosen because the vortex roll-up features are repeatable and distinguishable.

In order to extract the location of the interface between the two gases, the gradient-based Canny edge detection method is applied to concentration fields. This method computes an approximate pixel by pixel gradient, and is thresholded locally or globally to distinguish steep gradients. This can be accomplished for the current work using a simple threshold (Canny, 1986). This method has been used widely in the combustion field for flame edge

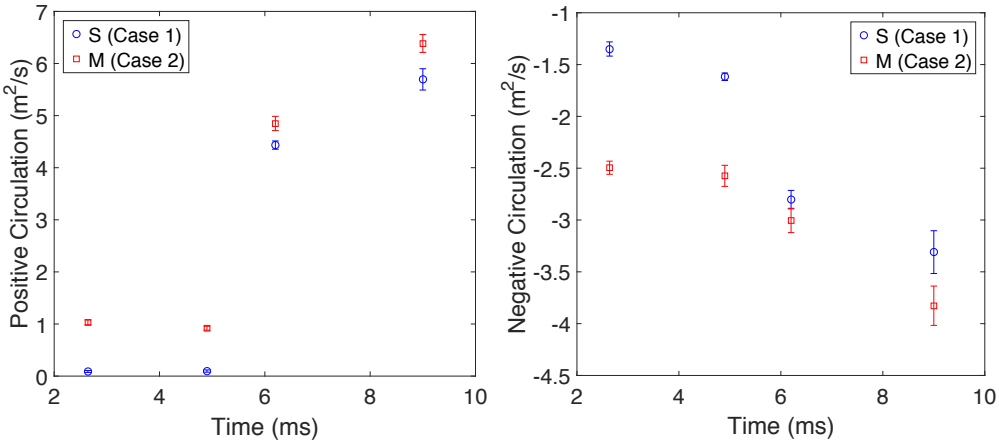

(a) Positive circulation

(b) Negative circulation

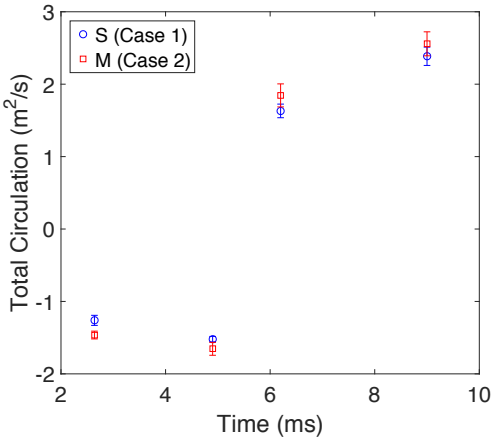

(c) Total circulation

Figure 4.19: Positive, negative and total circulation at $M \sim 1.55$. The error bar at each time represents $\pm$ one standard deviation.

detection (Slabaugh, Pratt, and Lucht, 2015; Sweeney and Hochgreb, 2009; Malm *et al.*, 2000; Reisenhofer, Kiefer, and King, 2016; Fries *et al.*, 2019). Because there is a sharp gradient between the two fluids in the case shown, this method gives an accurate interface location. Additionally, to increase the accuracy of the measurement and reduce error, corrected PLIF images are pre-processed with a 3×3 gaussian filtering to reduce the effect of noise in the interface region. The vorticity fields are obtained by taking the discrete curl of 2D velocity fields (Reilly *et al.*, 2015). Finally, to characterize and compare localized vorticity and roll-up locations, vorticity concentration fields are registered with the interface locations identified using edge detection. The results are shown in figure 4.20.

The interface crosses any streamwise line (vertical in figure 4.20) multiple times at any roll-up location. Therefore, roll-up locations are identified by calculating the total length of interface crossings ($N_{crossings} * dx$) at each streamwise line. This is ensemble averaged and shown along the spanwise direction in figure 4.20(a). Furthermore, to analyze regions of vorticity localized within the roll-ups, the vorticity fields are averaged in the streamwise direction (X) similarly, and shown in figure 4.20 (b). It is observed that there is a strong correlation between the peaks of the interface crossings and vorticity concentration, which indicates that regions of vorticity concentration coincide with roll-up locations.

Comparison between high and low Mach numbers suggests that there are 3 large and 3 small roll-ups and peaks in vorticity concentration in the high Mach case whereas there are 1 large and 2 small roll-ups and vorticity peaks in the low Mach number case. Finally, the total interface length is computed and averaged over the ensemble. The ratios of this quantity to ensemble average of mixing width for each case are also calculated, which are $39.72/8.56 = 4.64$ for high Mach ($M \sim 1.9$) compared to $24.12/8.26 = 2.92$ for $M \sim 1.55$. Overall, comparison of the number of roll-ups and arc-length to mixing-width ratio indicates that the high Mach number results in greater vorticity deposition which leads to more roll-ups (higher secondary perturbation wavenumber) and consequently more stretching of the interface.

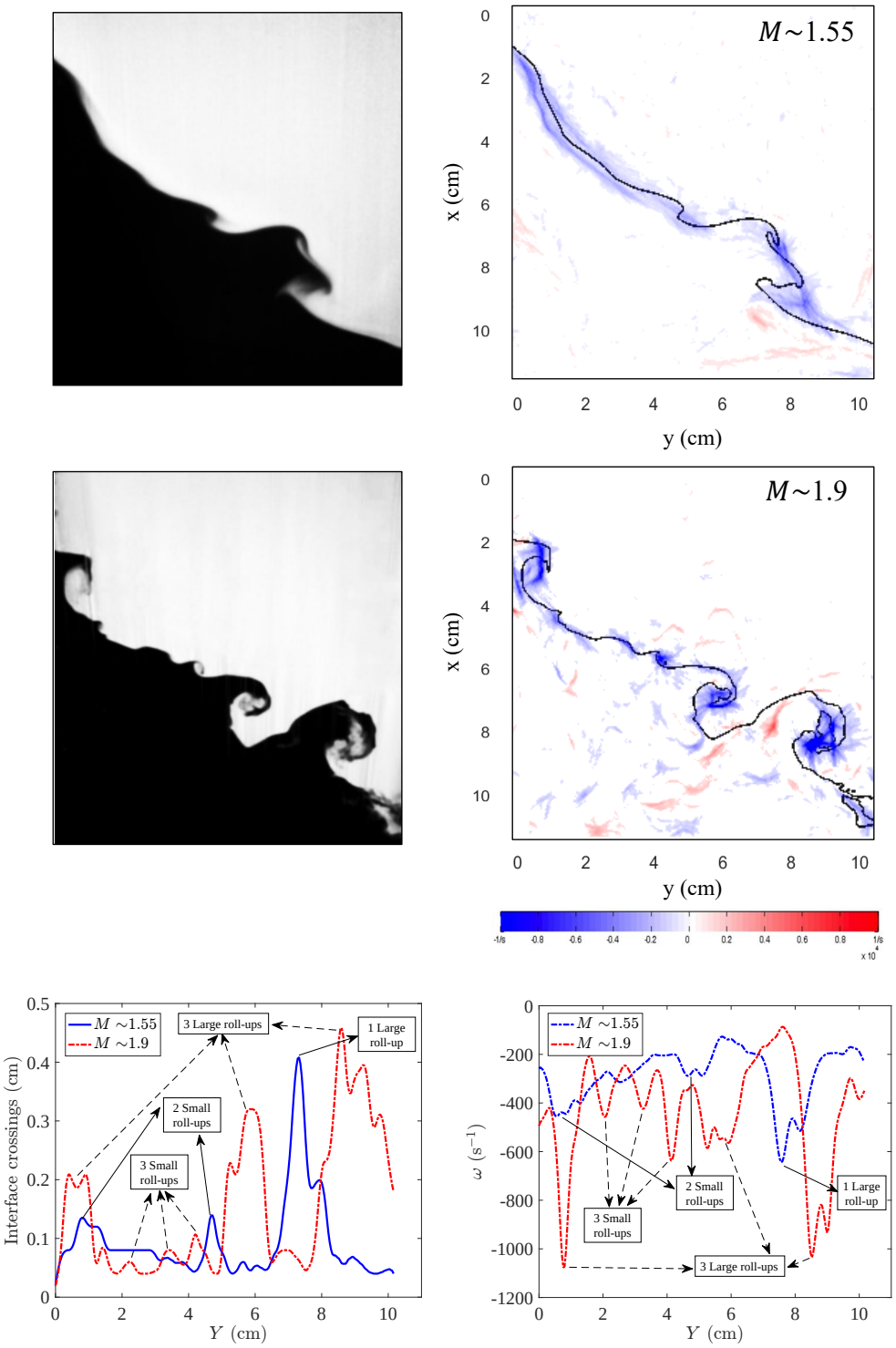

(a) Interface arc length in spanwise direction *(b)* streamwise average of vorticity magnitude in spanwise direction

Figure 4.20: Comparison of streamwise average of (a) vorticity profiles and (b) interface crossings (from canny edge detection) for $M \sim 1.55$ case (first row) and $M \sim 1.9$ case (second row) at latest time before reshock for the single-mode case. Also superimposed over vorticity fields are the interface edges.

4.2 Mixing Transition Analysis

In this section, turbulent mass-flux, Reynolds stress components and anisotropy in the flow are analyzed. Turbulent length scales derived from the density and velocity fluctuation fields are discussed. Taylor microscales and integral scales are calculated to estimate the inertial range, and the amount of decadal separation in different velocity and density spectra. Reynolds number is calculated and subsequently used to compute inner viscous and Liepmann–Taylor scales. Finally, transition to turbulence is discussed in regard to its relation to length scales and Reynolds number, and by analyzing different velocity and density spectra.

4.2.1 Turbulent Mass-Flux

The turbulent mass-flux velocity, $a(x,y)_i = \frac{\langle \rho' u_i' \rangle}{\langle \rho \rangle}$ is closely related to the b parameter (density self-correlation), since b appears in the production of turbulent mass-flux. Additionally, turbulent mass-flux appears in the primary production term of turbulent kinetic energy (Livescu and Ristorcelli, 2008; Tomkins *et al.*, 2013). It also appears in the second term of the Reynolds stress decomposition. The averaging performed over the ensemble yields one field of turbulent mass-flux for each case at each time. Then to obtain a profile, these fields are averaged in the spanwise direction similar to the presentation of b fields and profiles. The results for fields are shown for the high Mach case in figure 4.22 in addition to spanwise-averaged profiles (figure 4.21) to have a better understanding of the physics of the flow.

The turbulent mass-flux indicates intense penetration of the gases within each other driven by turbulent fluctuations. Where lighter than average fluid moves with higher than average velocity (causing negative density fluctuations coupled with a positive streamwise velocity fluctuation), it leads to a negative turbulent mass-flux. On average, this phenomenon is seen throughout most of the flow.

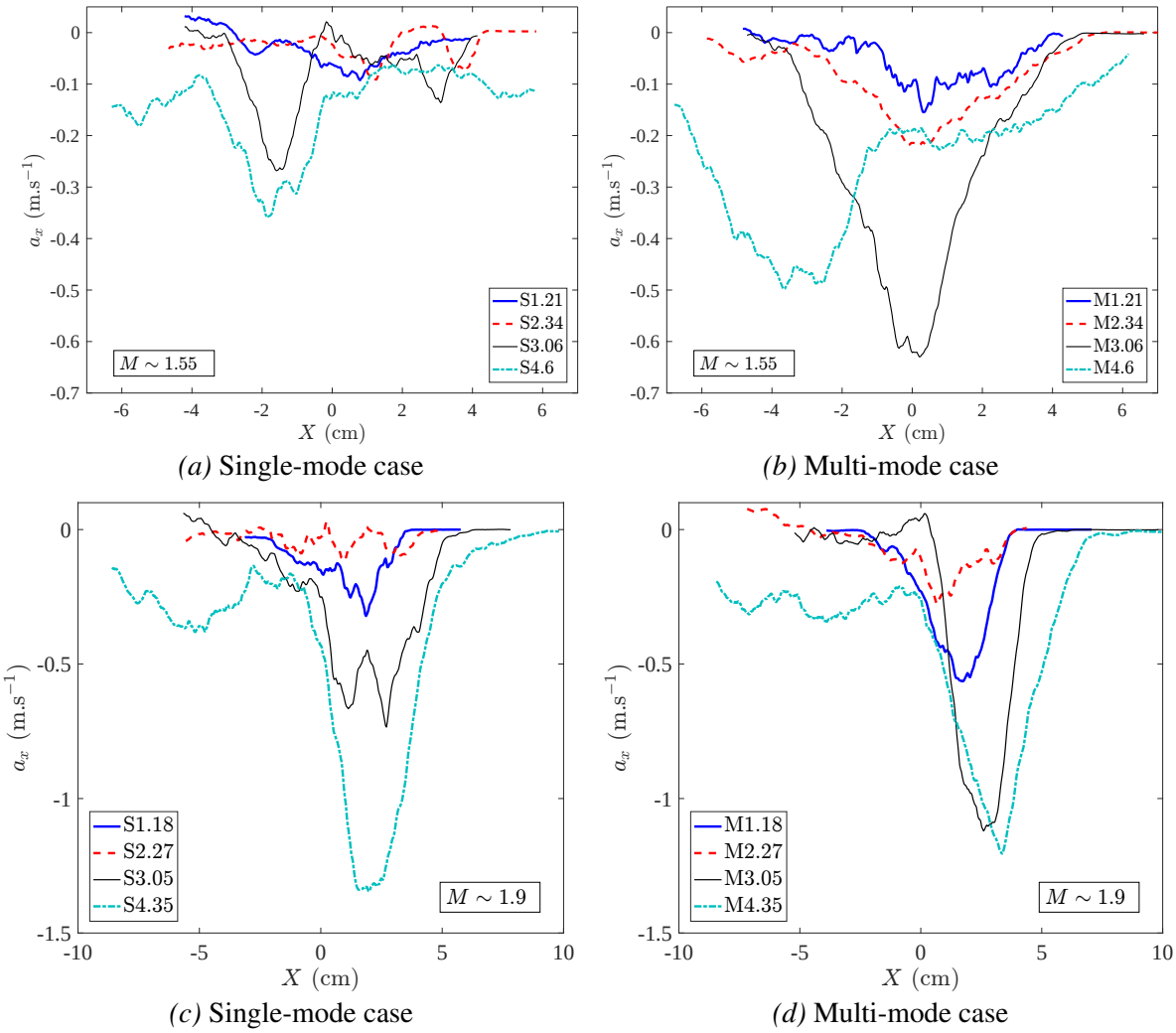

(a) Single-mode case

(b) Multi-mode case

(c) Single-mode case

(d) Multi-mode case

Figure 4.21: Effect of initial condition on temporal evolution of turbulent mass-flux profiles along the streamwise direction before and after reshock at $M \sim 1.55$ and $M \sim 1.9$ for the (a,c) single-mode (S) case and (b,d) multi-mode (M) case.

At $M \sim 1.55$, at all times, the multi-mode case has more fluctuating mass flux across the majority of the mixing layer. At the earliest time, $\tau = 1.21$, the single- and multi-mode cases appear very similar in shape, but with slightly more flux in the multi-mode case. At $\tau = 2.34$ two small negative peaks can be seen in the single-mode case where shear-driven rollups cause increased fluctuations, while the multi-mode case has a maximum near the center of mass where POD analysis of the initial condition suggests there is significant modal content. Reshock amplifies the flux in both cases as more energy is delivered to the mixing region. At $\tau = 3.06$ the single-mode case shows peaks at the edges of the mixing region where there is intense penetration. The multi-mode case shows a similar level of flux near the edges, but a maximum near the center of mass. At the latest time ($\tau = 4.6$) the bubble region (the right side of the image) is becoming more homogenized, and therefore has less mass flux than the spike region where a sharper contrast in density yields more intense flux of mass. Similar to $\tau = 3.06$, the multi-mode case has greater mass flux over almost the entire domain, reinforcing the assumption that the multi-mode case is in a more turbulent state.

In the high Mach case ($M \sim 1.9$), an interesting feature that can be identified in the mass-flux fields before reshock, is the location of roll-up features, especially in the single-mode case where there are alternating positive and negative turbulent-mass flux regions due to the cresting motion of the roll-ups. In the location of a roll-up, the heavy gas tends to penetrate upward (*negative* direction) and the light gas tends to push downward near the top of the roll-up. However, on the crest and interior of the roll-up, heavy gas tends to move down and light gas moves upward resulting in regions of positive mass flux velocity. In the multi-mode case, since the fluctuations are distributed over a larger portion of the flow, and there is more mixed material, this behaviour in turbulent mass-flux is less evident than in the single-mode case. After reshock, similar to the density self-correlation fields, density and velocity fluctuations are more concentrated in one part of the flow in the single-mode case, compared to the more diffuse distribution of fluctuations along the interface in the multi-

mode case due to higher variability or nonlinearity of the initial interface perturbation.

These interesting features are concealed in spanwise-averaged profiles, especially before reshock, in this inhomogeneous flow. However, the relative magnitude of turbulent mass-flux between low and high Mach cases can be observed in the spanwise-averaged profiles in figure 4.23. The magnitude of turbulent mass-flux after reshock is almost three times higher than the low Mach case. Moreover, similar to density self-correlation profiles, the peak of turbulent mass-flux is shifted to the bubble side in the high Mach case compared to the low Mach case where this occurs on the spike side. This indicates that active mixing and greater production of turbulent kinetic energy is occurring in the bubble side for the high Mach case.

4.2.2 Reynolds Stress

Another measure related to turbulence intensity and transport is the Favre-averaged Reynolds stress. The components of the Reynolds stress, including the aforementioned term containing mass flux, are given by:

$$R_{ij} = \langle \rho u_i'' u_j'' \rangle = \langle \rho \rangle \langle u_i' u_j' \rangle - \langle \rho \rangle \langle a_i \rangle \langle a_j \rangle + \langle \rho' u_i' u_j' \rangle, \tag{4.18}$$

where the double prime indicates Favre averaging ($u_i'' = u_i - \frac{\langle \rho u_i \rangle}{\langle \rho \rangle}$). The streamwise profile of relative contribution of the three terms in the Reynolds stress for R_{11} is shown in figure 4.24 for both single and multi-mode cases at $M \sim 1.9$ before and after reshock. The first term, which is the mean density times the velocity fluctuation correlation, is clearly the dominant contributor at each time for both cases. A similar trend is observed for all three components (R_{11}, R_{12}, R_{22}) of the Reynolds stress tensor. The turbulent mass-flux term (T_2) is at least 1000 times smaller than the first term. The third term, which is the triple correlation term, is approximately 10 times larger than the second term and 100 times smaller than the first term. This finding indicates the importance of the contribution of the first term to the Reynolds stress and its significance for modeling (Balakumar *et al.*,

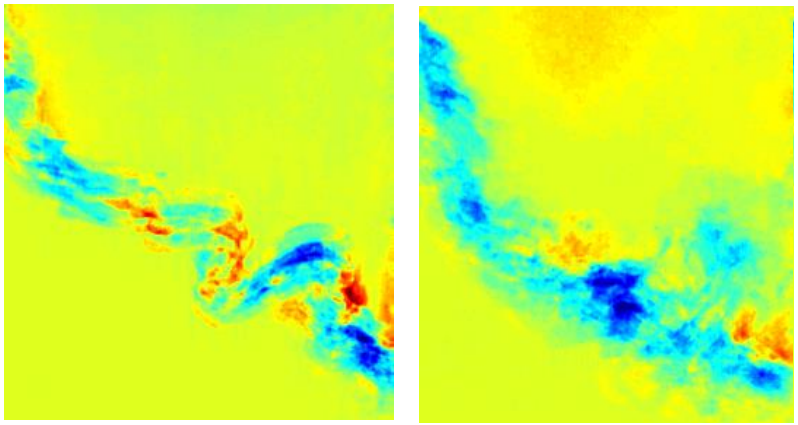

(a) Single-mode at latest time before reshock

(b) Multi-mode at latest time before reshock

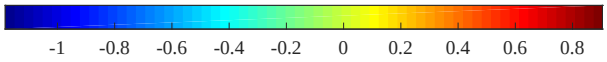

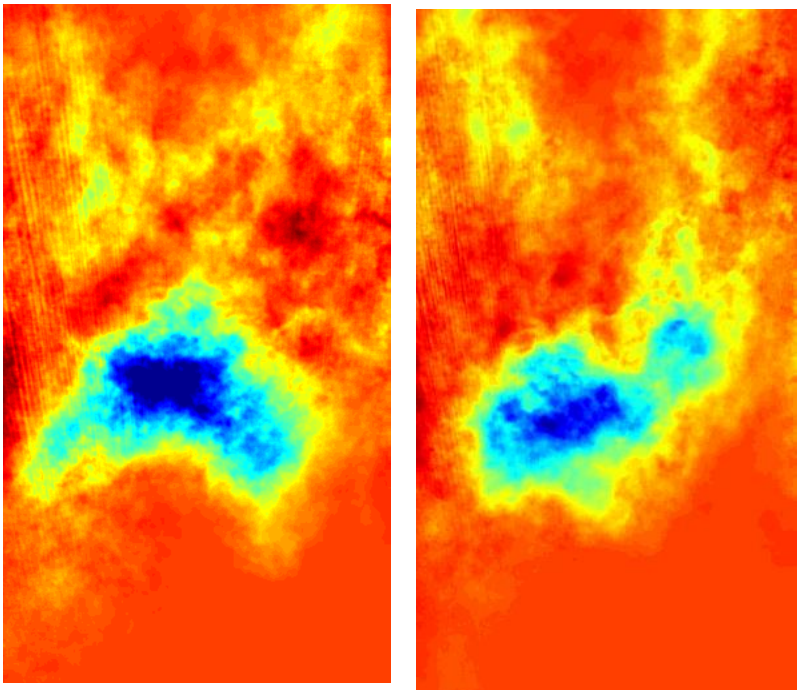

(c) Single-mode at latest time after reshock

(d) Multi-mode at latest time after reshock

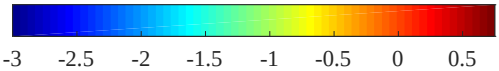

Figure 4.22: Fields of turbulent mass-flux (a,b) before and (c,d) after reshock at $M \sim 1.9$ for the (a,c) single-mode (S) case and (b,d) multi-mode (M) case.

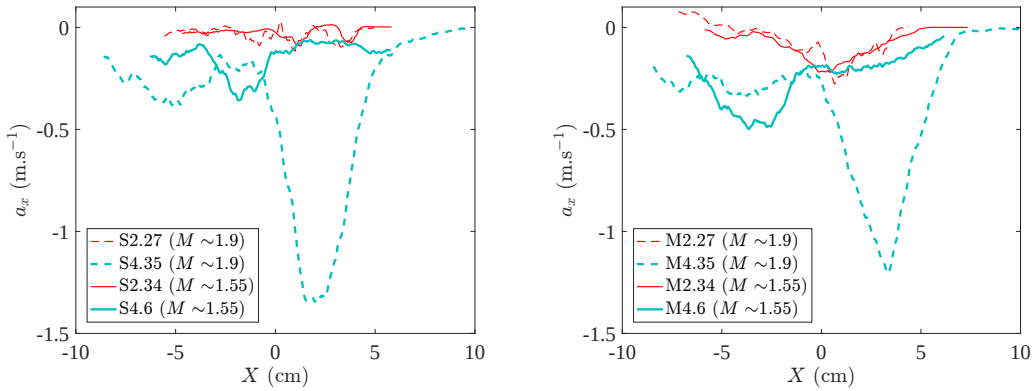

(a) Single-mode case *(b)* Multi-mode case

Figure 4.23: Mach number comparison on the temporal evolution of turbulent mass-flux profiles along the streamwise direction before and after reshock at both $M \sim 1.55$ and $M \sim 1.9$ for the a) single-mode (S) case and b) multi-mode (M) case.

2012; Shankar and Lele, 2014). In addition, the spanwise average of these terms highlights that the main differences for different initial conditions before and after reshock occur in the second term (turbulent mass-flux term). The ratio of the second term to the first term for the multi-mode case before reshock is uniformly distributed, and slightly larger compared to the single-mode case, which is due to uniform distribution of density-velocity fluctuations along the interface in the multi-mode case, whereas there are concentrated fluctuations in the roll-up locations in the single-mode case (figure 4.25 (a)). The reshock effect on the mass flux term is shown in figure 4.25 (b). After reshock, T_2/R_{11} increases significantly which is expected due to higher velocity and density fluctuations. However, even if the ratio is almost 10 to 100 times larger than this ratio before reshock, the contribution of the mass flux term is still less than 0.01 of the first term's contribution.

4.2.3 Anisotropy Analysis

Another important parameter related to Reynolds stress, is anisotropy. The normalized anisotropy is defined as

$$\beta_{ij} = \frac{R_{ij}}{R_{kk}} - \frac{1}{3}\delta_{ij}. \tag{4.19}$$

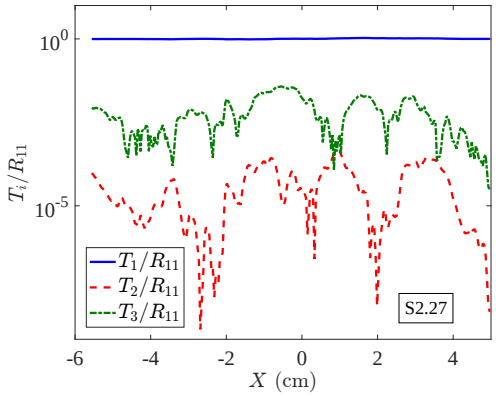

(a) Single-mode at latest time before reshock

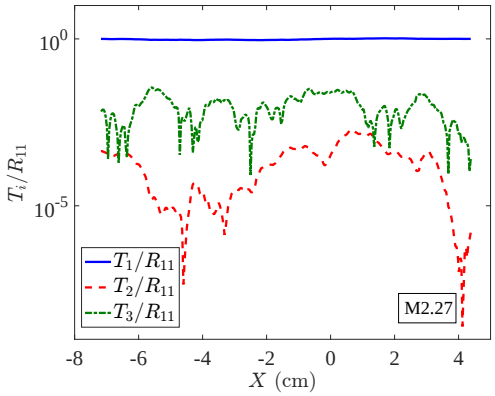

(b) Multi-mode at latest time before reshock

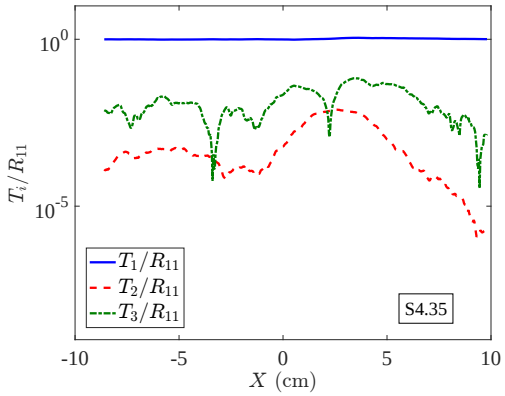

(c) Single-mode at latest time after reshock

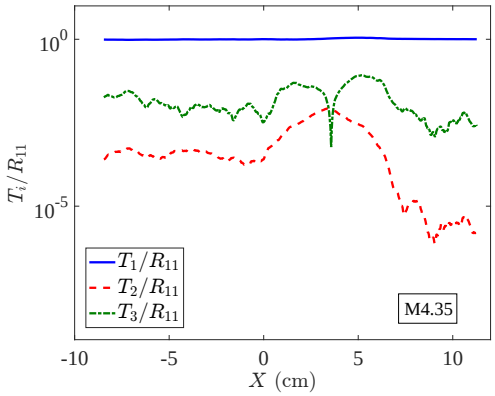

(d) Multi-mode at latest time after reshock

Figure 4.24: Relative contribution of three terms in the Reynolds stress equation (a,b) before and (c,d) after reshock for (a,c) single-mode and (b,d) multi-mode cases at $M \sim 1.9$.

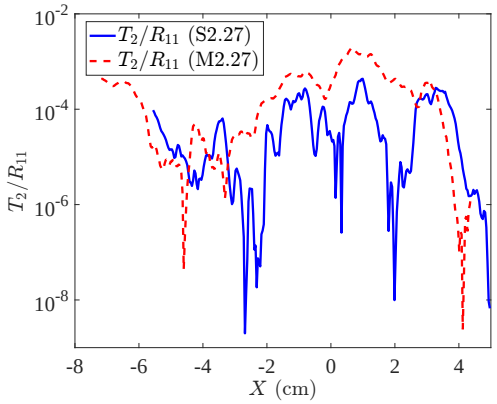

(a) Contribution of mass flux term for single and multi-mode cases at latest time before reshock

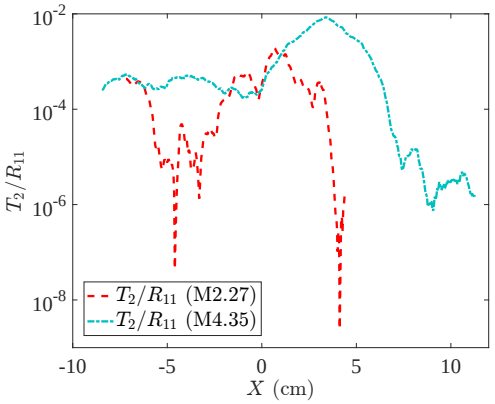

(b) Contribution of mass flux term for multi-mode cases at before and after reshock

Figure 4.25: Effect of (a) initial condition and (b) reshock on the contribution of second component of Reynolds stress.

The normalized anisotropy has a limited range: $\beta_{kk} = -1/3$, $\beta_{kk} = +2/3$ and $\beta_{kk} = 0$; correspond to zero turbulent kinetic energy in the k-direction, all turbulent kinetic energy in that direction, and the isotropic turbulence limit, respectively. For our case, only the streamwise and spanwise components of velocity are available and so we assume that the fluctuations in the out of plane direction are equal to those of the spanwise direction. This sets β_{22} equal to β_{33}. This assumption is likely less accurate before reshock but is a necessary limitation of 2D PIV measurements. Additionally, the magnitude of the anisotropy tensor, $||\boldsymbol{\beta}|| = \beta_{ij}\beta_{ij}$ at each time is important to understand the physical reason for the variations in scaling of the turbulent kinetic energy spectra.

Figure 4.26 shows the components of the spanwise average of the normalized anisotropy tensor for the low Mach number case ($M \sim 1.55$) for each initial condition at two times, immediately before reshock ($\tau = 2.34$), and late after reshock ($\tau = 4.6$). From this figure it is evident that the anisotropy decreases after reshock for both cases, with large regions of nearly equal components near the center of mass in the flow. Before reshock, both cases show a peak in anisotropy near the center of mass though the single-mode case shows a higher anisotropy. Both cases at $\tau = 4.6$ show strong non-zero values for the β_{11} and β_{22} components in the upstream flow field indicating that the former, pre-reshock bubble region now contains the majority of anisotropy. In the downstream region of the post reshock flows we see a much more isotropic region with the β_{22} term taking a positive value.

Additional insight into the flow can be gained by examining the spatial distribution of the anisotropy components at $M \sim 1.55$. Figure 4.27 shows the spatial distribution of β_{11}. It is noticeable that the anisotropy does not drop to zero away from the interface due to a small amount of noise which manifests predominantly in the streamwise direction. Although the magnitude of some of the velocity fluctuations away from the interface is small compared to the fluctuations at the interface, the normalization of anisotropy does not typically weight the magnitude of fluctuations because it is classically used in homogeneous flows. Nevertheless, it is customary to present information about inhomogeneous flow in

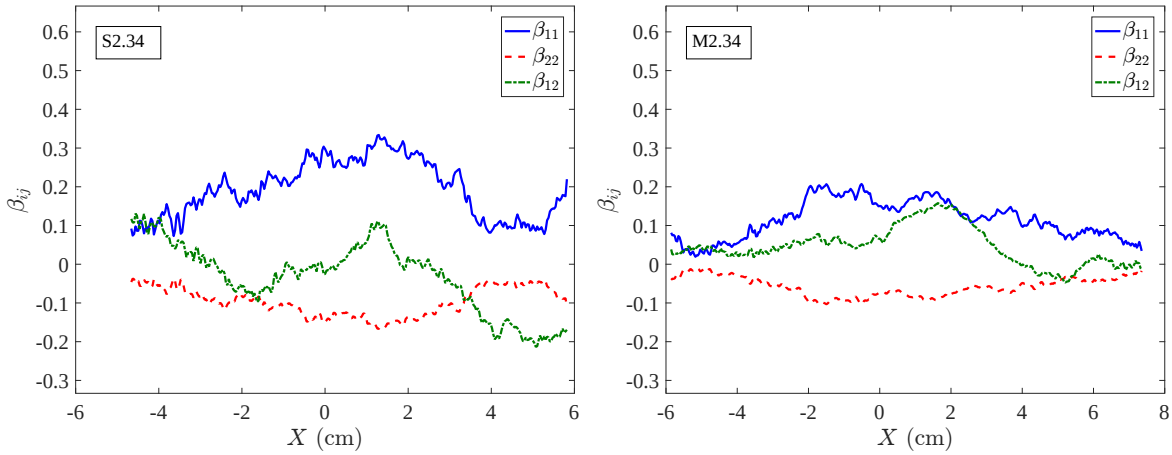

(a) Single-mode at latest time before reshock

(b) Multi-mode at latest time after reshock

(c) Single-mode at latest time after reshock

(d) Multi-mode at latest time after reshock

Figure 4.26: Normalized anisotropy tensor components (a,b) before and (c,d) after reshock for both (a,c) single-mode and (b,d) multi-mode cases at $M \sim 1.55$.

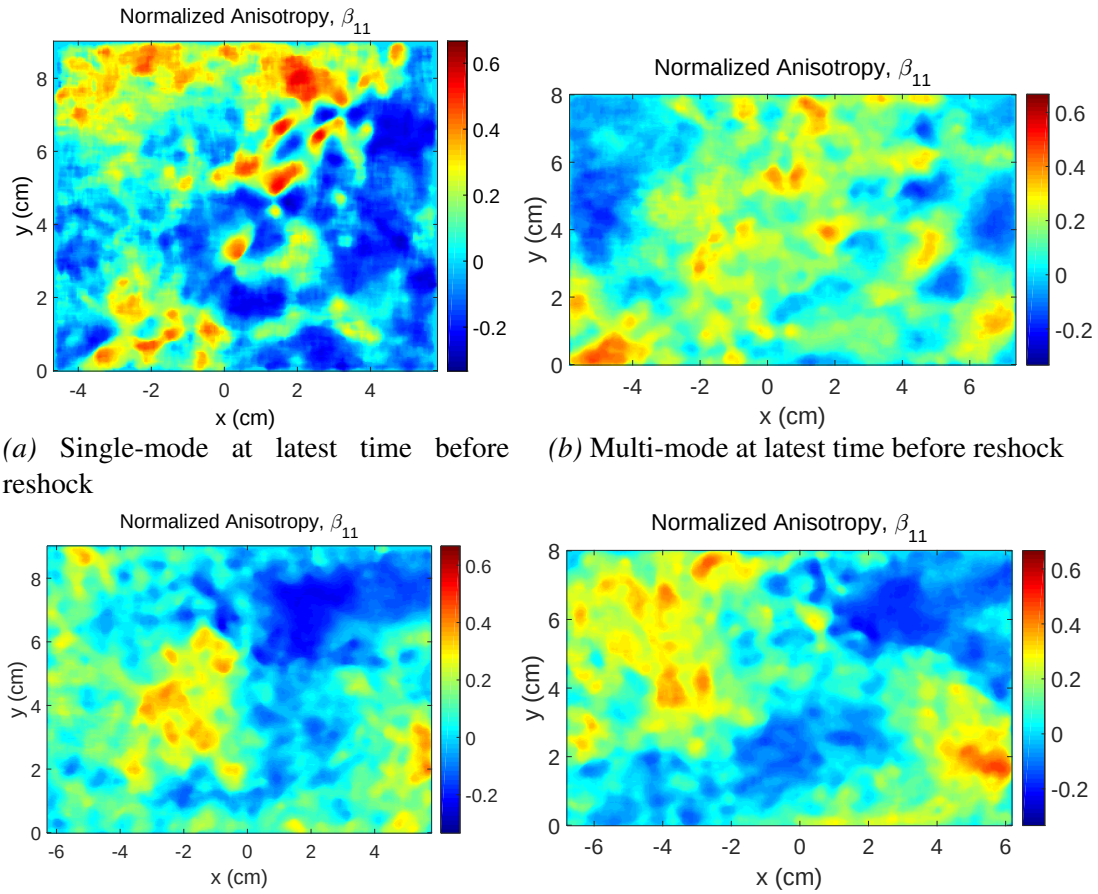

(a) Single-mode at latest time before reshock

(b) Multi-mode at latest time before reshock

(c) Single-mode at latest time after reshock

(d) Multi-mode at latest time after reshock

Figure 4.27: $\beta_{11}(x, y)$ for each case at latest time before reshock and latest time post reshock at $M \sim 1.55$.

this context while understanding the caveats involved. Before reshock, β_{11} is highest upstream of the interface in the bubble-front region and near the spike tip. The single-mode inclined interface case shows a less well organized field due in part to its less turbulent flow field. After reshock, these regions persist and are transported by the overturning process. The downstream region now contains the high β_{11} found in the pre-reshock spike while the anisotropy of the pre-reshock bubble front is pushed upstream by the emerging post-reshock spike structure.

The spanwise average of β_{ij} obscures the total anisotropy as it averages both positive and negative values over the span. Since ensemble averaging is used, the values across the span are not correlated by their average. Figure 4.28 shows the spanwise average of

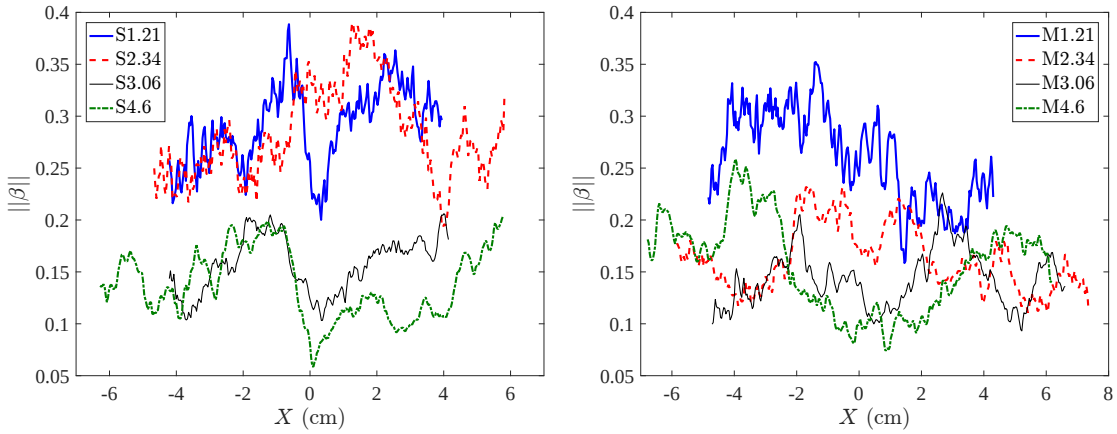

(a) Single-mode case *(b)* Multi-mode case

Figure 4.28: The magnitude of the normalized anisotropy tensor before and after reshock at $M \sim 1.55$ for the (a) single-mode (S) case and (b) multi-mode (M) case.

the magnitude of the anisotropy tensor $\|\beta\|$ at $M \sim 1.55$, which is positive everywhere, accounts for all three directions, and diminishes to zero as the flow becomes isotropic. From Figure 4.28, a clear trend emerges over time for the two cases. Both cases show a high degree of anisotropy at early times, as expected, but the multi-mode case shows a much lower anisotropy before reshock, at $\tau = 2.34$. The anisotropy remains lower for the multi-mode case after reshock. The single-mode case does not show low values until after reshock.

The spanwise average of the normalized anisotropy tensor for the high Mach case ($M \sim 1.9$) for both initial conditions is plotted in figure 4.29. In addition, to investigate the effect of Mach number on anisotropy, the spanwise average of the magnitude of the anisotropy tensor for both Mach numbers is shown in figure 4.30. After the incident shock, at the latest time before reshock, the anisotropy magnitude in the high Mach number case for single-mode is less than the low Mach case, specifically close to the center of mass, which is due to transfer of energy from the streamwise to spanwise direction in the two large roll-up locations, but this difference is not significant. However, in the multi-mode case before reshock, and noticeably after reshock, the anisotropy is significantly higher in the high Mach case. This large difference is due to higher turbulent kinetic energy in

the flow, especially in the streamwise component, because of the stronger incident shock and reshock. As a result of this higher energy in the shock direction, more time is needed for the flow to transfer energy from the shock-direction component to the spanwise and out-of-plane components to reduce anisotropy. High anisotropy is particularly noticeable in the high Mach case in the bubble side (light gas side), since the flow is still strongly inhomogeneous and active mixing is occurring in that region for both initial conditions. Overall, before reshock for the high Mach number case, similar to the low Mach number case, turbulent kinetic energy in the flow at some regions near the center of mass is transferred from the shock direction to the spanwise direction and there is localized isotropy in the flow. However, after reshock in the higher Mach case, there is a strong anisotropy in the flow and energy in the streamwise direction is dominant. Even at late time after reshock, Tritschler *et al.* (2014) observed that the anisotropy reached a small asymptotic value, but did not reach zero.

4.2.4 Turbulent Length Scales

Using simultaneous PLIF/PIV measurements, it is possible to compute different length scales to study mixing transition. The Taylor microscale can be defined using two methods. The first method is based on fitting a quadratic function to the peak and two points, both on the right side of the peak, of the velocity or density fluctuation autocorrelations. the slope of the resulting curvature at $f(0)$ is 0 (Pope, 2000; Champagne, Harris, and Corrsin, 1970; Weber *et al.*, 2014; Ramaprabhu and Andrews, 2004; Mohaghar *et al.*, 2017; Reese *et al.*, 2018). The average of the correlation functions for each field can be defined as

$$f(r) = \frac{\left\langle F(x,y)F(x+r,y) \right\rangle}{F^2} \tag{4.20}$$

where F is the density or velocity fluctuation (streamwise or spanwise), and $\left\langle F(x,y)F(x+r,y) \right\rangle$ is the spatial average (over x and y) and the ensemble average over all the fields. The

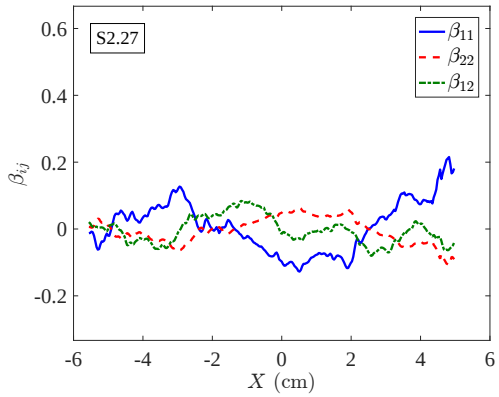

(a) Single-mode at latest time before reshock

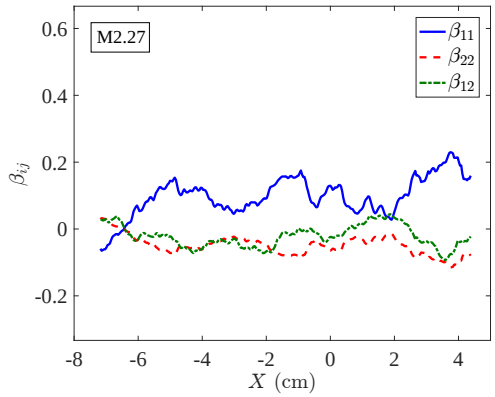

(b) Multi-mode at latest time before reshock

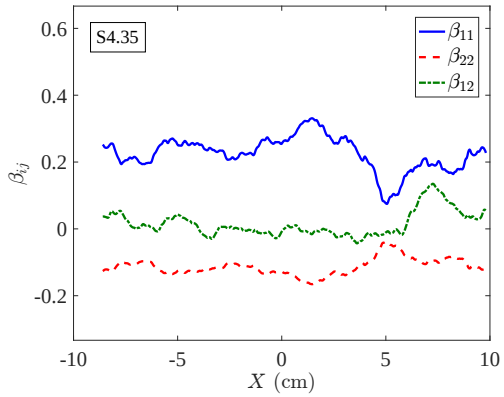

(c) Single-mode at latest time after reshock

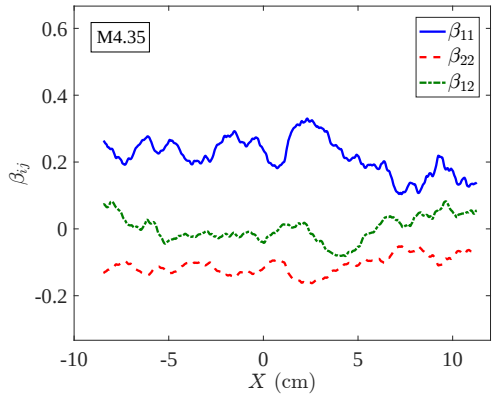

(d) Multi-mode at latest time after reshock

Figure 4.29: Normalized anisotropy tensor components (a,b) before and (c,d) after reshock for both (a,c) single-mode and (b,d) multi-mode cases at $M \sim 1.9$.

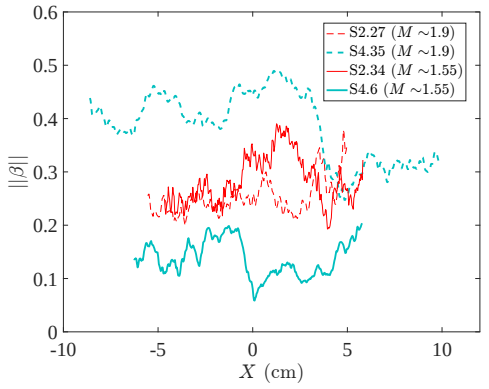

(a) Single-mode case

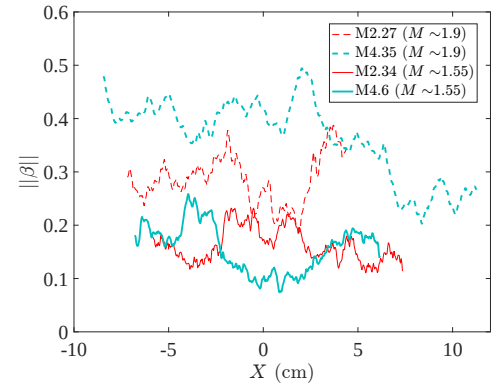

(b) Multi-mode case

Figure 4.30: Effect of Mach number on the magnitude of the normalized anisotropy tensor before and after reshock at both $M \sim 1.55$ and $M \sim 1.9$ for the (a) single-mode (S) case and (b) multi-mode (M) case.

Taylor microscale then can be calculated from the curvature of the autocorrelation function,

$$\lambda_T = \left[-\frac{1}{2}\frac{d^2 f(0)}{dr^2} \right]^{-1/2}. \tag{4.21}$$

The combined Taylor microscale from the autocorrelation function is obtained by $\lambda_{T,corr} = \sqrt{\lambda_{T,u'}^2 + \lambda_{T,v'}^2}$. Correlation functions can also be used to calculate the integral scale by finding the area under the curve of $f(r)$,

$$L_1 = \int f(r) dr. \tag{4.22}$$

An example of the longitudinal correlation function of streamwise velocity fluctuations at latest time after reshock for $M \sim 1.55$ is shown for the single-mode and multi-mode cases in Figure 4.33 (a) and (b) respectively. The red lines indicate the fitted line on the first three points of the correlation function to calculate Taylor microscale.

An alternative method for calculating the Taylor microscale is by computing the spatial variance and gradients of the velocity or density fluctuations (Pope, 2000). Thus the Taylor microscale can be calculated as,

$$\lambda_{T,\eta} = \sqrt{\frac{2\overline{\eta_i'^2}}{\overline{(\partial \eta_i'/\partial x_i)^2}}}, \tag{4.23}$$

where η is the velocity or density field. The combined Taylor microscale from the gradient method is found by $\lambda_{T,grad} = \sqrt{\lambda_{T,u'}^2 + \lambda_{T,v'}^2}$, similar to the combined Taylor microscale calculated from the correlation function. According to Figure 4.31, both methods show similar trends for Taylor microscales given by the velocity fluctuations, as both increase after reshock. Figure 4.31 also shows that the Taylor microscales from streamwise and spanwise velocity fluctuations are higher in the multi-mode case compared to the single-mode case due to higher fluctuations. Taylor microscales derived from streamwise density fluctuations calculated using the spatial gradient method, are also shown in Figure 4.32. This figure shows a trend similar to the streamwise velocity fluctuation Taylor microscales

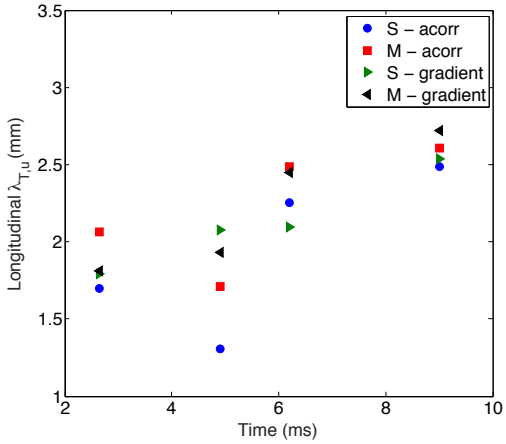

(a) Taylor microscales based on streamwise velocity fluctuations

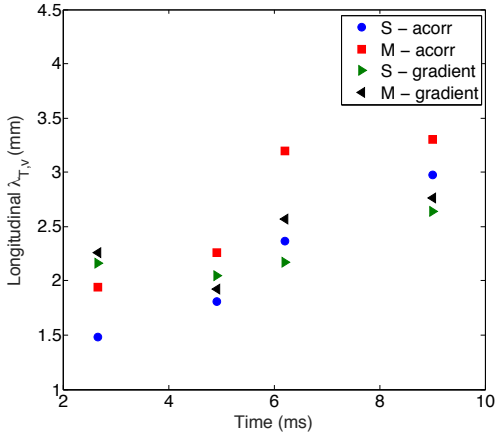

(b) Taylor microscales based on spanwise velocity fluctuations

Figure 4.31: Comparison between the use of spatial gradients and correlation functions to find the Taylor microscales at $M \sim 1.55$ derived from (a) streamwise and (b) spanwise velocity fluctuations.

from the correlation function method. However, the magnitude of Taylor microscales based on velocity fluctuation is between 1.5 and 3 mm, notably different from those given by density fluctuations, which are around 0.4 to 1 mm. This difference is thought to be due to resolution effects.

Finally, the total Taylor microscale is measured by averaging the results from the correlation and gradient methods, $\lambda_T = \frac{\lambda_{T,grad}+\lambda_{T,corr}}{2}$. The time evolution of the integral scale and Taylor microscale for both single and multi-mode cases and at both Mach numbers are plotted in figures 4.33 (c) and (d). The magnitude of the integral scale is not affected by Mach number, and similar values are obtained for both Mach numbers at each time. Although the trend in the Taylor microscale is similar to that of $M \sim 1.55$, the magnitude of the $M \sim 1.9$ Taylor microscale is a factor of 1.25 ± 0.05 times that of the former at similar nondimensional times. This is due to stronger fluctuations in the latter case. Finally, in order to get an overall picture of scale separation, the different length scales computed (from the largest scale, mixing width, to the Taylor microscale) are plotted in figure 4.33 (e) for the multi-mode case at $M \sim 1.9$.

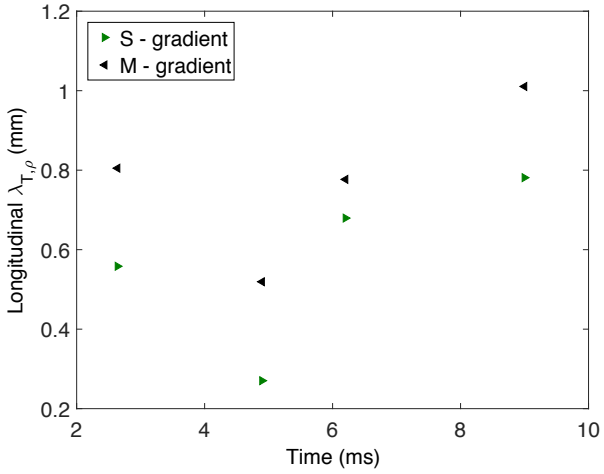

Figure 4.32: Temporal evolution of the streamwise density fluctuation based Taylor microscale at $M \sim 1.55$, found using spatial gradients.

4.2.5 Reynolds Number and Time-dependent Length-scale Criteria

To evaluate mixing transition and inertial range formation, the ratio of Liepmann-Taylor (λ_L) to inner-viscous (λ_ν) scales can be investigated, with the assumption that the flow will have an established inertial range if $\frac{\lambda_L}{\lambda_\nu} \gg 1$ (Lombardini, Pullin, and Meiron, 2012). To evaluate this criterion and to determine whether mixing transition may have occurred in this particular flow (Dimotakis, 2000), the ratio is calculated using

$$\frac{\lambda_L}{\lambda_\nu} \approx \frac{5Re^{-1/2}\delta}{50Re^{-3/4}\delta} \approx \frac{1}{10}Re^{1/4}. \tag{4.24}$$

This criterion is equivalent to $Re > 10^4$ which is suggested by Dimotakis (2000) for the onset of mixing transition. Therefore to investigate the satisfaction of mixing transition criteria, the local Reynolds number based on turbulent kinetic energy is calculated to investigate mixing transition (Tomkins *et al.*, 2013; Orlicz *et al.*, 2015). This Reynolds number is defined as

$$Re = \frac{u_{rms}\delta}{\nu_{mix}}, \tag{4.25}$$

where $u_{rms} = \sqrt{\overline{u_i'^2}}$, ν_{mix} is the kinematic viscosity of the mixture, and mixing layer thick-

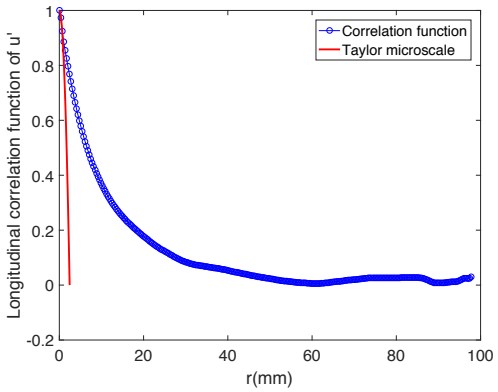

(a) Single-mode at latest time after reshock

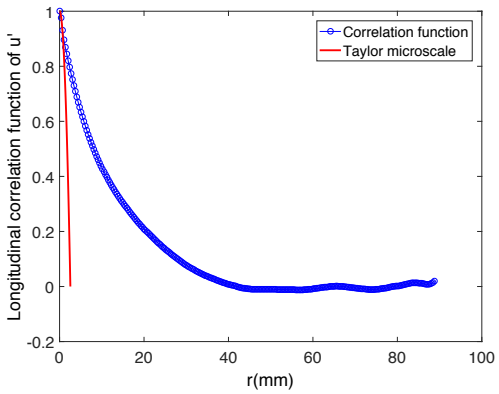

(b) Multi-mode at latest time after reshock

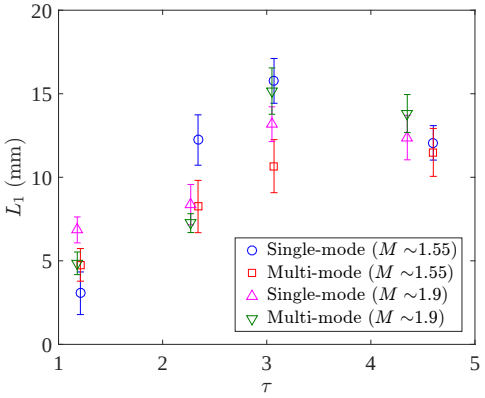

(c) Integral scale

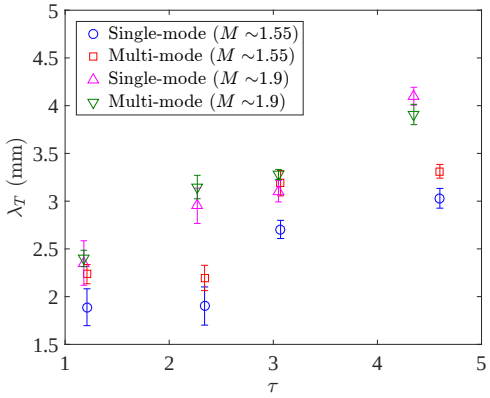

(d) Taylor microscale

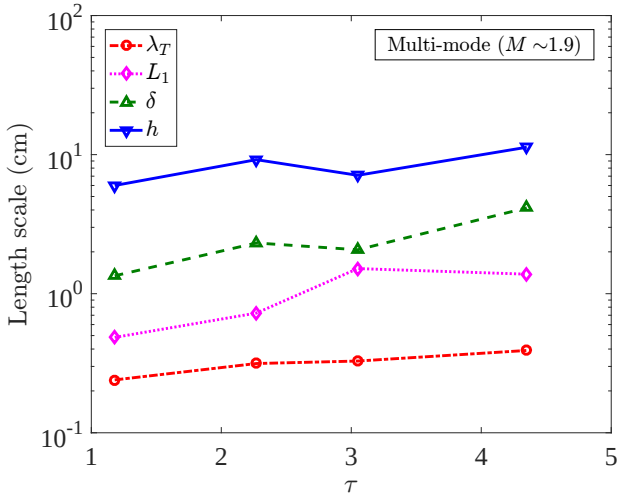

(e) Summary of length scales

Figure 4.33: (a–b) Sample correlation functions of streamwise velocity fluctuation for both cases at latest time after reshock for $M \sim 1.55$, and temporal evolution of (c) integral scale at both Mach and initial conditions, (d) Taylor micro-scale at both Mach and initial conditions, and (e) summary of length scales at $M \sim 1.9$ for multi-mode case. τ is nondimensional time.

ness is chosen for the length scale δ instead of mixing width (h). Mixing layer thickness is a more representative mixing length scale in this type of flow, analogous to the length scales chosen in other canonical flows, which were outlined by Dimotakis (2005).

The kinematic viscosity before and after reshock are approximately 6.27×10^{-6} and 4.08×10^{-6} m^2/s at $M \sim 1.55$, and 5.49×10^{-6} and 3.14×10^{-6} m^2/s at $M \sim 1.9$, respectively. The local Reynolds number for both single- and multi-mode cases at both Mach numbers is plotted in figure 4.34. The dashed lines represent the mixing transition criterion ($Re = 1 - 2 \times 10^4$, (Dimotakis, 2000)). Before reshock at early time, Reynolds numbers are below the transition criterion for all cases, but the multi-mode case has a significantly higher Re than the single-mode case. At late time, although Re increases for all cases, only the multi-mode case at higher Mach number is in the threshold for mixing transition. After reshock, due to a jump in turbulent kinetic energy, there is a rapid increase in Re for all cases. Both single- and multi-mode cases have similar values for the two Mach numbers at early times after reshock, though Re for $M \sim 1.9$ increases at a faster rate due to the higher growth rate of the mixing layer thickness. The Reynolds number criterion for mixing transition is also satisfied at all times after reshock.

In addition to the Reynolds number criterion, the other important criterion to consider for mixing transition is one proposed by Robey *et al.* (2003), particularly for time-evolving flow like RMI flow. The new time-dependent scale which is proposed for the upper bound of the inertial range is $\lambda_D = 5 \times (\nu t)^{1/2}$. Robey *et al.* (2003) suggested an extension to the mixing transition work of Dimotakis (2000) when the Liepmann scale is strongly evolving with time. According to this criterion, the inertial range forms in the flow when the viscous diffusion scale (time-dependent critical scale) is larger than the inner-viscous scale (i.e., $\lambda_D/\lambda_\nu > 1$). The inner-viscous scales and the time-dependent scale at each time for both Mach numbers and both initial conditions are plotted in figure 4.35. The ratio λ_D/λ_ν is greater than one only at the latest time after reshock, and is close to one at the latest time before reshock for the higher-Mach cases and early time after reshock

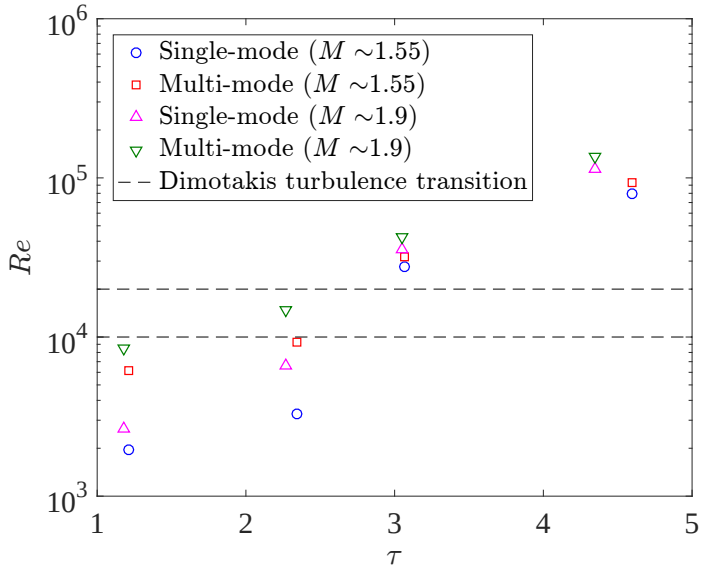

Figure 4.34: Reynolds number estimation with nondimensional time (τ) based on turbulent kinetic energy and mixing layer thickness. Reshock occurs at $\tau \sim 2.4$ (two times before and two times after reshock). Dashed lines indicate a threshold for turbulent mixing (Dimotakis, 2000).

for both Mach numbers. Therefore, unlike the Reynolds number criterion, the latest time after reshock is the only time that mixing transition occurs in the flow based on this time-dependent criterion.

4.2.6 Energy Spectra and Structure Function

In order to understand the growth of different scales and to quantify the inertial range, the time evolution of fluctuating kinetic energy, fluctuating enstrophy and the density variance spectra before and after reshock are presented. The general procedure used to compute the spectrum of a quantity $\varphi(x, y, t)'$ (velocity, density or enstrophy fluctuation) is described by Reilly *et al.* (2015). Thus, the one dimensional energy spectrum of any quantity is

$$[E_{\varphi'}]_i = FFT(\varphi') \cdot conj(FFT(\varphi')), \tag{4.26}$$

where $FFT(\varphi')$ is the Fourier coefficient of the 2π periodic function $\varphi(x, y, t)'$ in the spanwise direction and $conj(FFT(\varphi'))$ is its complex conjugate.

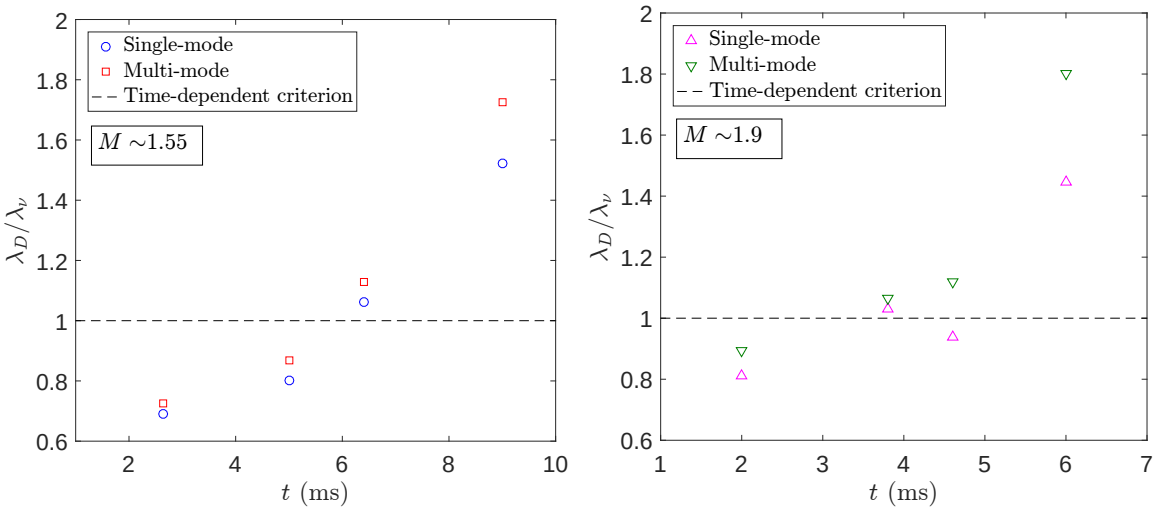

(a) $M \sim 1.55$ *(b)* $M \sim 1.9$

Figure 4.35: Time-dependent transition criterion evaluation using the ratio of diffusion to inner-viscous scales.

The temporal development of the total fluctuating kinetic energy spectra is computed by adding the u' and v' components of the energy spectra for the i-th column.

$$[E]_i = [E_{u'}]_i + [E_{v'}]_i \tag{4.27}$$

Regarding the evolution and distribution of the turbulent kinetic energy spectra, several computational and experimental works observed the existence of a $k^{-5/3}$ scaling in a small range of wavenumbers for density and velocity fluctuation spectra at late times in the RMI flow, when breakdown of scales occurs (Vorobieff, Rightley, and Benjamin, 1998; Vorobieff *et al.*, 2003; Weber *et al.*, 2014; Hill, Pantano, and Pullin, 2006; Schilling and Latini, 2010). In the recent work by Reese *et al.* (2018), $k^{-5/3}$ scaling is observed at late time after incident shock for kinetic energy spectra computed from relative velocity (termed global velocity fluctuation in their work). However, the scaling of RMI flow is still not well understood when the large scales in the flow still have not broken down completely and the flow is strongly inhomogeneous and anisotropic. Thornber *et al.* (2011b) clearly showed that when the flow is still in early development after reshock, the slope is steeper than -5/3 (found -2 for broadband case), but it can reach -5/3 or -3/2 at late time development in the

flow.

The progression of the kinetic energy spectra without w' component for the single- and multi-mode cases at $M \sim 1.55$ at each time is shown in Figure 4.36. In Figure 4.36(a–b), one can observe oscillations before reshock, especially in the single-mode case at early time ($\tau = 1.21$), which are then smoothed by reshock. The energy spectra increase after reshock ($\tau = 3.06$) for both cases, as the second shock adds more energy to the mixing region. Conversely, energy decays after incident shock at $\tau = 2.34$ and at late time after reshock ($\tau = 4.6$).

In order to investigate the level of anisotropy and memory of initial conditions across different scales with time for both single and multi-mode cases, the normalized cross-correlation spectrum between u' and v', $|E_{u'v'}(k_y)|/[E_{u'u'}(k_y)E_{v'v'}(k_y)]^{1/2}$, is considered at $M \sim 1.55$ in Figures 4.36(c–d) (Tavoularis and Corrsin, 1981b; Tavoularis and Corrsin, 1981a). Anisotropy is clearly present before reshock ($\tau = 1.21$ and $\tau = 2.34$) in the single-mode case even at smaller scales, however in the multi-mode case, the tendency toward isotropy of small scales is evident as the wave number increases. This local isotropy in the multi-mode case also suggests that memory of the initial condition is maintained before reshock (both $\tau = 1.21$ and $\tau = 2.34$) because imposed perturbations in the IC cause a tendency toward isotropy in mid-range scales. After reshock ($\tau = 3.06$ and $\tau = 4.6$), the cross-correlation spectrum decays more rapidly in both single- and multi-mode cases which indicates that local isotropy is reached at lower wave numbers than before reshock. The decrease in normalized cross-correlation spectrum from $\tau = 3.06$ to $\tau = 4.6$ in both cases at larger scales is an indicator of breakdown of large scales to small scales between these two times. Comparison of single- and multi-mode cases at $\tau = 3.06$ and $\tau = 4.6$ shows the similarity between imposed scales in the initial condition and the scales which result from breakdown of large to small scales upon reshock. Thus, a significant range of scales exists which are locally isotropic in both cases, and the anisotropy is primarily contained in the large scale which is common to the two cases.

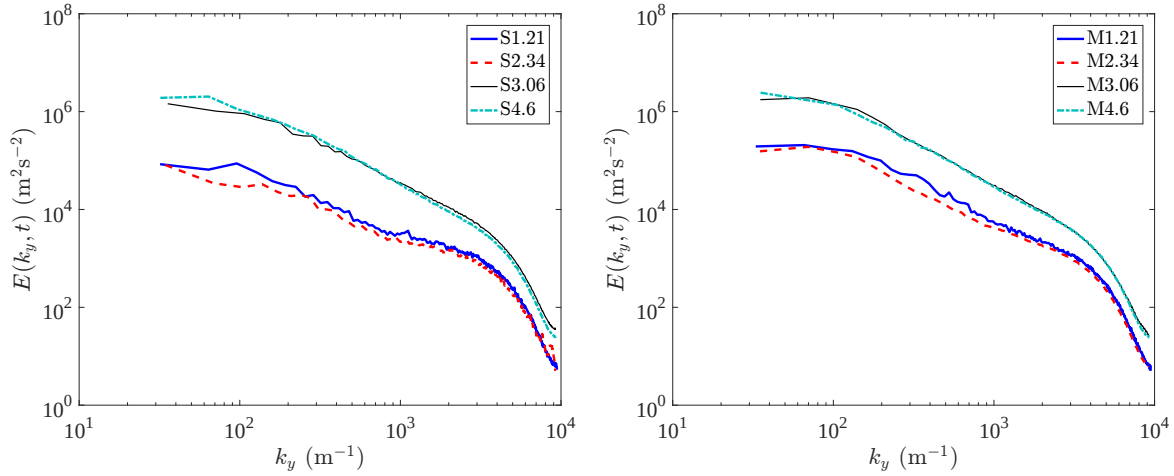

(a) Single-mode case

(b) Multi-mode case

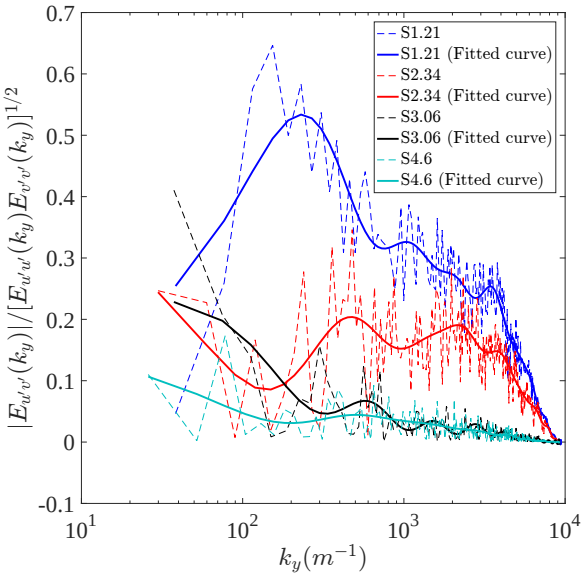

(c) Single-mode case

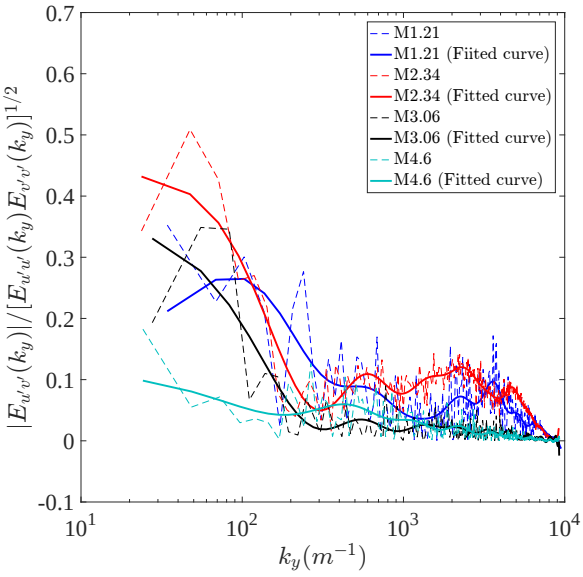

(d) Multi-mode case

Figure 4.36: Evolution of turbulent kinetic energy spectra before and after reshock at $M \sim 1.55$ for both (a)single-mode and (b)multi-mode cases, and (c–d) the normalized cross-correlation spectrum (dashed line fitted with a solid line).

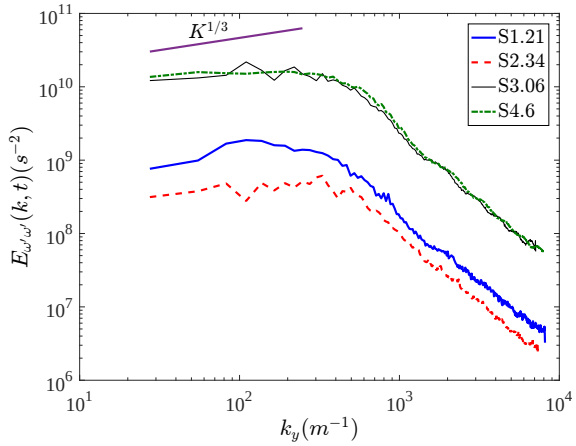

(a) Single-mode case at $M \sim 1.55$

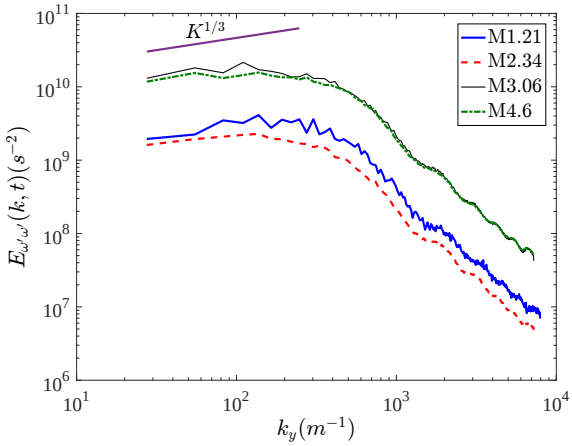

(b) Multi-mode case at $M \sim 1.55$

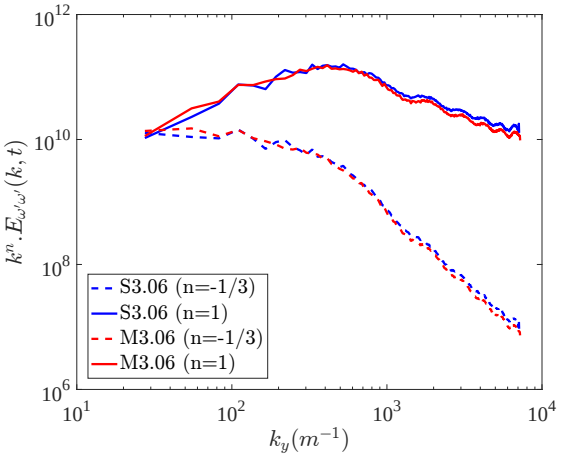

(c) Early time after reshock at $M \sim 1.55$

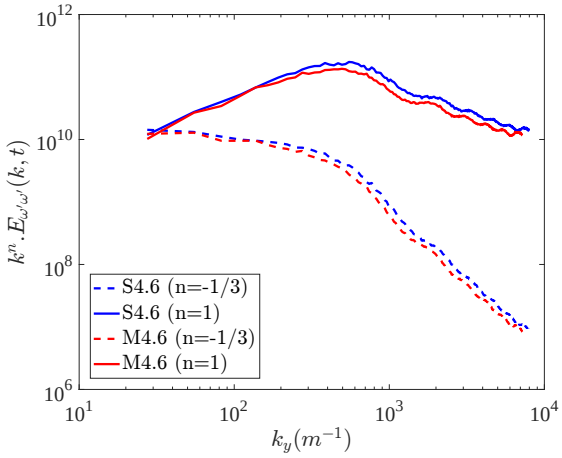

(d) Late time after reshock at $M \sim 1.55$

Figure 4.37: Temporal evolution of (a–b) the fluctuation enstrophy spectra, and (c–d) a comparison of compensated spectra at early and late times after reshock at $M \sim 1.55$.

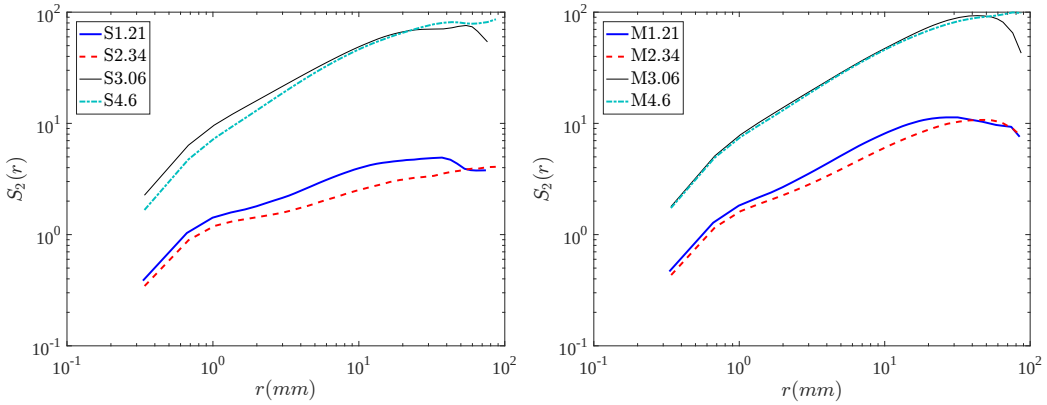

(a) Single-mode case at $M \sim 1.55$ *(b)* Multi-mode case at $M \sim 1.55$

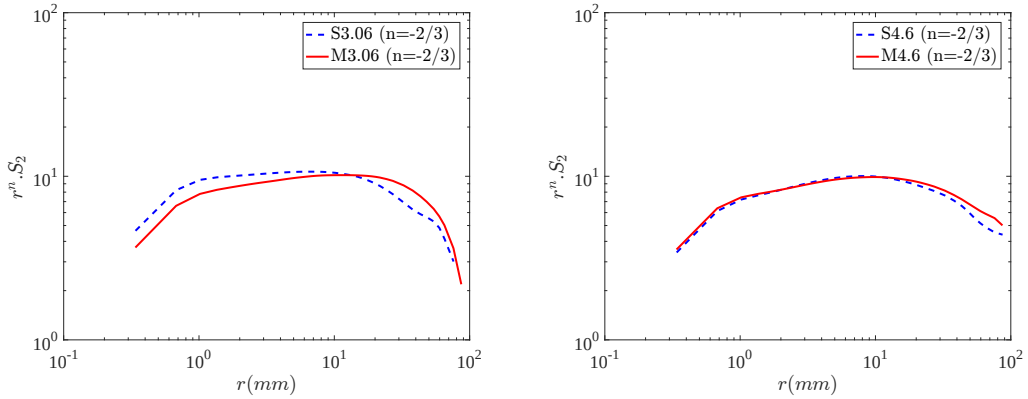

(c) Early time after reshock at $M \sim 1.55$ *(d)* Late time after reshock at $M \sim 1.55$

Figure 4.38: (a–b) Temporal evolution of the velocity structure function, and (c–d) a comparison of compensated structure function at early and late reshock times at $M \sim 1.55$.

The fluctuating enstrophy is defined as $\frac{1}{2}(\omega')^2$ and time evolution of its spectra for $M \sim 1.55$ is shown in Figure 4.37(a–b), which also shows the compensated spectra for both of the cases after reshock [Fig 4.37(c–d)], similar to the velocity energy spectra in Figure 4.36. While the slope of fluctuating enstrophy spectra is lower than velocity spectra, it is similar to the velocity energy spectra in that it is again amplified by reshock. An additional similarity is that the enstrophy spectra also decays at late time after the incident shock ($\tau = 2.34$).

The fluctuating enstrophy spectra in homogeneous, isotropic flow (classical turbulence) can be related to velocity spectra via $E_{\omega'\omega'}(k,t) = k^2 E(k,t)$. The expected slope of the inertial range in the fluctuating enstrophy spectra will be 1/3 at small wave numbers and -1 at large wave numbers for 3D turbulence. Moreover, according to Batchelor (1969) and Kraichnan (1967), the energy spectra of classical 2D turbulence scales with k^{-3}, which yields -1 scaling for enstrophy spectra at inertial range scales. Therefore -1 scaling in the enstrophy spectrum can be compared with both classical 3D turbulence at larger wave numbers and classical 2D turbulence at smaller wave numbers (Kraichnan, 1967; Batchelor, 1969). It is important to note the assumptions of classical spectra are that the flow is both isotropic and incompressible. The flow is fairly incompressible after passage of the shock, but is anisotropic and inhomogeneous which is discussed in the analysis of energy spectra. However, similar to Schilling, Latini, and Don (2007) and Orlicz *et al.* (2015), the scalings associated with classical turbulence of expected power laws of 5/3, for the small, energy-containing wave numbers, and 3, for larger wave numbers are used to compensate the enstrophy spectra. Figure 4.37(c–d) shows approximately k^{-1} scaling in the compensated spectra for less than one decade after reshock; however, the largest scales show scaling close to $k^{1/3}$ for almost one decade ($k_y \approx$20–200).

In addition, structure functions were calculated for $M \sim 1.55$ in order to find the inertial ranges and slopes of spectra so they could be compared with those from different spectra. The second order longitudinal structure function is $S_2(r) = \left\langle (\eta(x+r) - \eta(x))^2 \right\rangle$,

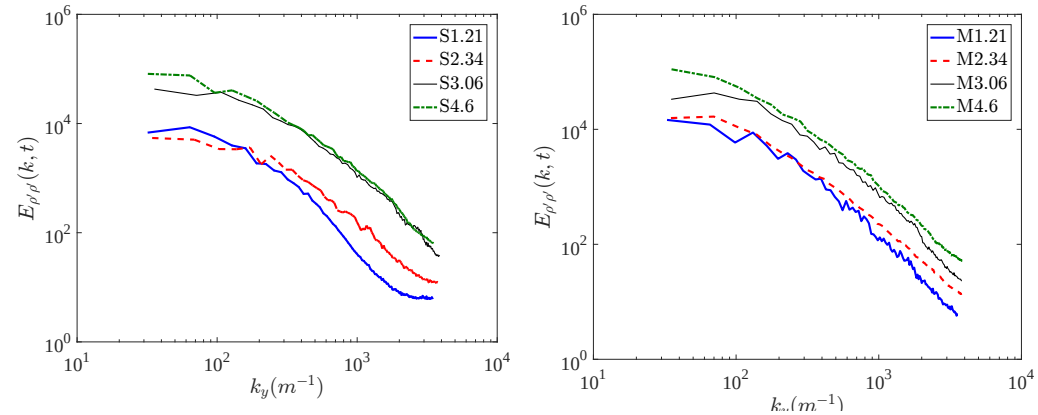

(a) Single-mode case at $M \sim 1.55$ *(b)* Multi-mode case at $M \sim 1.55$

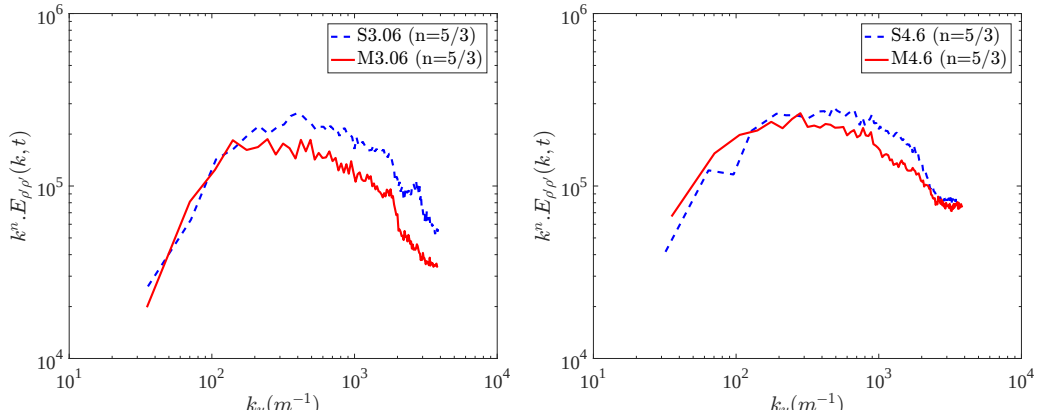

(c) Early time after reshock at $M \sim 1.55$ *(d)* Late time after reshock at $M \sim 1.55$

Figure 4.39: (a–b) Temporal evolution of the density spectra, and (c–d) a comparison of compensated spectra at early and late reshock times at $M \sim 1.55$.

where η is the velocity or density fluctuation in the direction of the separation length, r, and brackets $\left\langle \right\rangle$ denote both spatial and ensemble averaging.

Figure 4.38 shows the time evolution of the velocity structure functions for each case(a–b) at $M \sim 1.55$, as well as the comparison between the compensated structure functions after reshock (c–d). The decay of the small scale contribution can be seen during both pre ($\tau = 1.21$ to $\tau = 2.34$) and post ($\tau = 3.06$ to $\tau = 4.6$) reshock for the single- and multi-mode cases. In addition, the large scale peak is similarly damped at $\tau = 2.34$ and $\tau = 4.6$ for both cases. Analyzing the compensated structure functions after reshock shows a slope close to that of the 2/3 power law of Kolomogorov turbulence (classical turbulence) for almost an entire decade. Again, it should be noted that the flow is inhomogeneous and

anisotropic, and this result is compensated to be compared with classical scaling. Later in this chapter the exact spectral scaling is computed and discussed for energy spectra in this particular flow.

The temporal development of the density fluctuation spectrum and the comparison of compensated spectra for each case after reshock are shown in Figure 4.39 (a–b) and (c–d) for $M \sim 1.55$, respectively. Unlike the velocity fluctuation spectra, there is a small increase in the density spectra after incident shock, between $\tau = 1.21$ and $\tau = 2.34$, and after reshock, between $\tau = 3.06$ and $\tau = 4.6$, especially at small scales. Yet, similar to the velocity spectra, reshock sharply increased the spectra magnitude, which suggests that density fluctuations are stronger post-reshock. The classical scaling of -5/3 is again of interest to be compared with density spectra. Therefore, the assumption of isotropy at small scales should hold true in order to have the same scaling as a classical spectra. Some researchers have found similar scaling for density spectra even with inhomogeneous and unsteady flow, which is not assumed in the classical case (Vorobieff, Rightley, and Benjamin, 1998). In the current case, the density fluctuation spectrum shows an approximate $k^{-5/3}$ scaling for half a decade at intermediate wave numbers after reshock, as shown by the compensated spectra. There is a small increase in the inertial range which can be seen from $\tau = 3.06$ (early reshock) to $\tau = 4.6$ (late time after reshock). Furthermore, these results are verified by density fluctuation structure functions which are shown in Figure 4.40. Post-reshock, density fluctuation structure functions also show close to 2/3 scaling for intermediate r and for less than a decade.

Regarding scaling of energy spectra, several computational and experimental works observed existence of a $k^{-5/3}$ scaling in small range of wavenumbers for density and velocity fluctuation spectra at late times in the RM flow, when breakdown of scales occurs (Vorobieff, Rightley, and Benjamin, 1998; Vorobieff *et al.*, 2003; Weber *et al.*, 2014; Hill, Pantano, and Pullin, 2006; Schilling and Latini, 2010). In the recent work by Reese *et al.* (2018), $k^{-5/3}$ scaling is observed at late time after incident shock for kinetic energy spectra com-

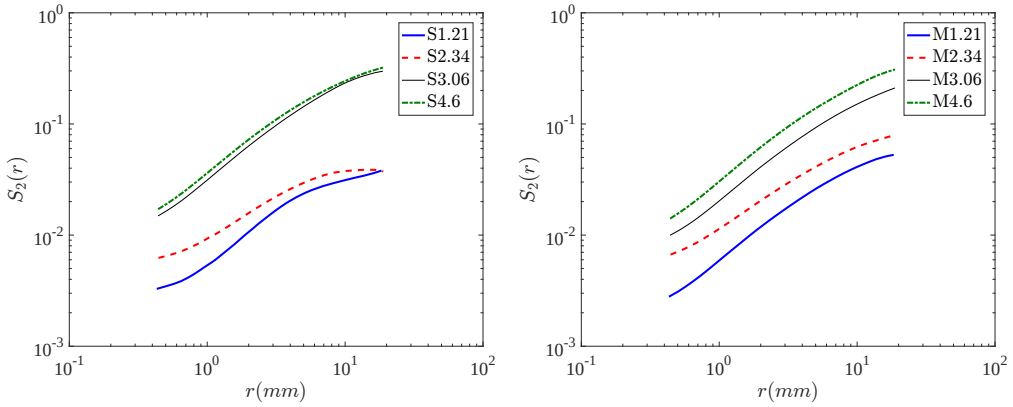

(a) Single-mode case at $M \sim 1.55$

(b) Multi-mode case at $M \sim 1.55$

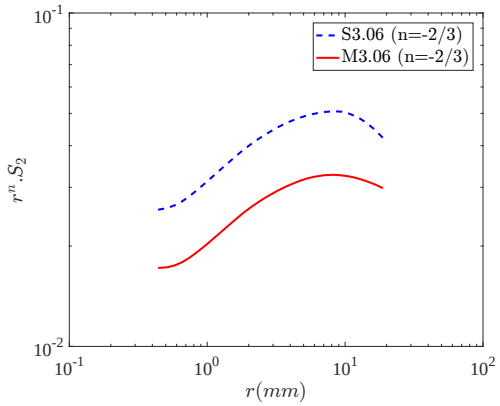

(c) Early time after reshock at $M \sim 1.55$

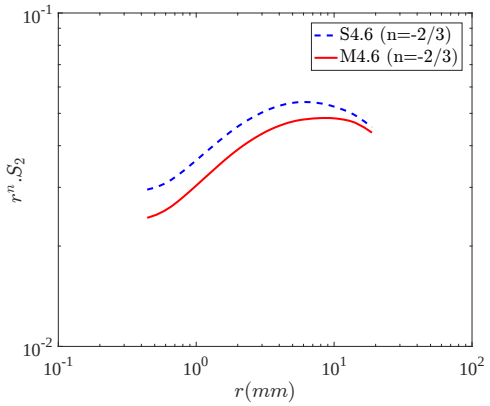

(d) Late time after reshock at $M \sim 1.55$

Figure 4.40: (a–b) Temporal evolution of the density structure function, and (c–d) a comparison of compensated structure function at early and late reshock times at $M \sim 1.55$.

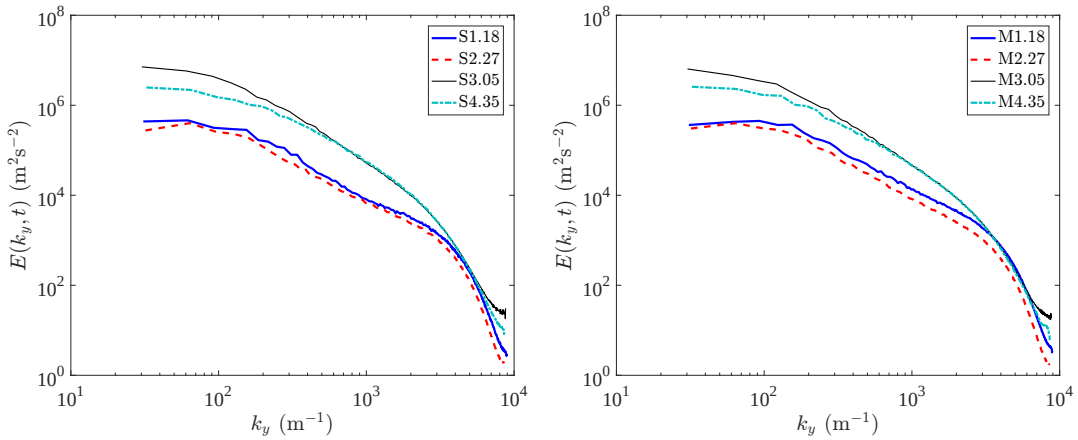

(a) Single-mode case *(b)* Multi-mode case

Figure 4.41: Evolution of turbulent kinetic energy spectra before and after reshock at $M \sim 1.9$ for both (a)single-mode and (b)multi-mode cases.

puted from relative velocity (termed global velocity fluctuation in their work). However, the scaling of RM flow is still not well understood when the large scales in the flow still have not broken down completely and the flow is strongly inhomogeneous and anisotropic. Thornber *et al.* (2011b) clearly showed that when flow is still in early development after reshock, the slope is steeper than -5/3 (found -2 for broadband case), but it can reach -5/3 or -3/2 at late time development in the flow. Zhou (2001) applied the general theory developed for turbulent flows by Kolmogorov with an external agent to the RMI and found a $k^{-3/2}$ scaling at the latest time where self-similarity is achieved.

Due to the high anisotropy observed in this flow, especially in the $M \sim 1.9$ case after reshock (owing to strong, large-scale, streamwise fluctuations produced by large-scale shear), it is important to investigate the actual scaling of energy spectra at both Mach numbers. Turbulent kinetic energy spectra before and after reshock at $M \sim 1.9$ for the two initial conditions are shown in figure 4.41. From figure 4.41, it is clear that the turbulent kinetic energy at early time after reshock is almost one decade greater than at late time before reshock due to additional energy deposited by reshock.

Additionally, to study formation of different ranges in the energy spectra and to identify any power law slopes, the precise slopes of the spectra are computed using $d(log(E(k_y))/d(log(k_y))$

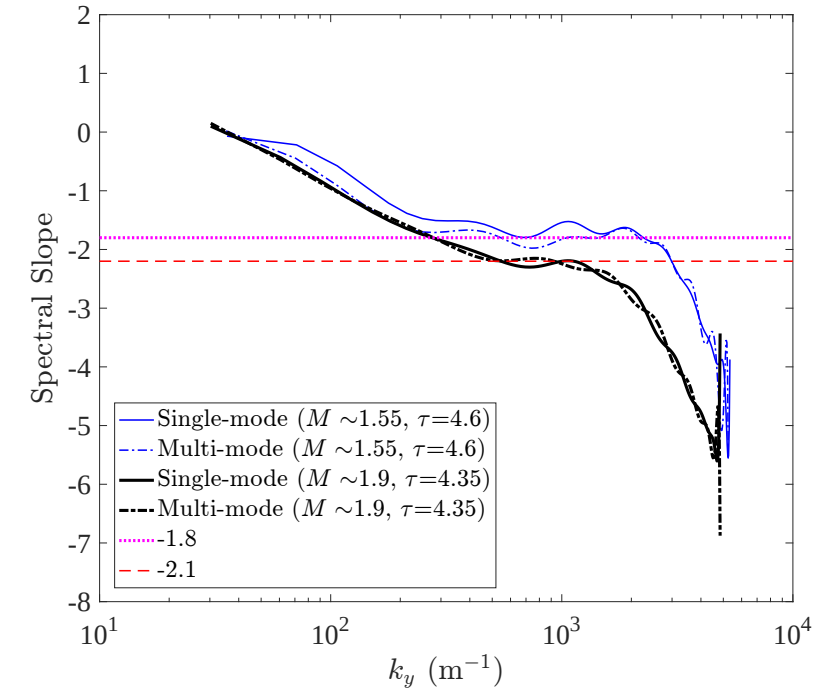

(a) Spectral slope

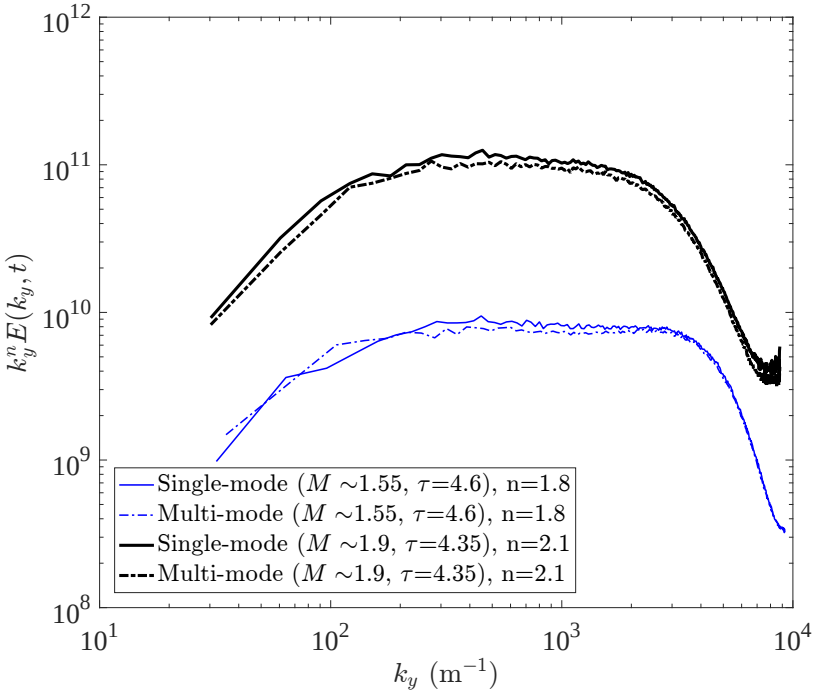

(b) Compensated energy spectra

Figure 4.42: (a) Local slope of spectra (logarithmic derivative) and (b) compensated energy spectra at latest time after reshock for both initial conditions at $M \sim 1.55$ and $M \sim 1.9$.

(Miller and Dimotakis, 1996; Kerstein, 1991). Mixing transition occurrence implies that an inertial range has formed after reshock. Therefore, it is reasonable to investigate spectral scaling at the latest time in the flow. Slopes of the spectra, and the energy spectra compensated based on the slopes found, for both low and high Mach at the latest time after reshock are plotted in figure 4.42. Due to the high energy deposited by reshock, which increases anisotropy, spectral slopes noticeably steeper than -5/3 are observed. The computed slopes are close to -1.8$\pm$0.05 for the low Mach (in the range $k_y \approx 300 - 3000$) and -2.1$\pm$0.1 for the high Mach number case (in the range $k_y \approx 300 - 2000$) after reshock. The spectral slope is steeper in the higher Mach number case due to higher anisotropy, which results from a larger deposition of energy to the shock-direction component of the flow by the higher-strength reshock.

CHAPTER 5
CONCLUSIONS

Effects of incident shock strength and initial condition on the nature of mixing and transition to turbulence in shock-driven flows called Richtmyer–Meshkov instability are investigated using simultaneous density-velocity (PLIF/PIV) diagnostics. Measurements were performed at two times before reshock, and for the first time in this regime at two times after reshock for both single and multi-mode initial conditions at $M \sim 1.55$ and $M \sim 1.9$. In both single- and multi-mode cases at each Mach number, the interface consists of a nitrogen-acetone mixture as the light gas over carbon dioxide as the heavy gas (Atwood number, $A \sim 0.22$).

Before reshock, comparison of the single and multi-mode case using density and velocity statistics, such as mixing width, mixedness, density self-correlation, anisotropy, vorticity, and normalized cross-correlation spectrum provide evidence that the flow shows a distinct memory of the initial conditions. In both cases the long-wavelength perturbation has a strong influence on the interface development before and after reshock because the overall entrainment, stretching, and overturning occur at this large scale. The coherence of the large wavelength spike and bubble features in the density field even after reshock leads to the conclusion that the memory of the largest scales is maintained.

After reshock, the reflected shock wave deposits additional vorticity which is two to three times higher than the initial vorticity deposition. The resulting disordered vorticity field produces small-scale perturbations similar to those present in the multi-mode initial condition, which then causes an apparent loss of memory of the initial condition at small wavelengths. However, the memory of the initial condition is still observed after reshock as indicated by the distribution of small-scale structures along the interface, and in the positive and negative vorticity distributions which correspond with the density gradients

of the small-scale structures as shown in Figure 4.18. Furthermore, the multi-mode case is observed to have less intense gradients and be more well mixed at all times even after reshock. The multi-mode case displayed higher positive circulation at all times, while the single-mode case showed higher negative circulation. This difference between the two cases results from the interaction of the initial shock and reshock with a more unidirectional density gradient in the single-mode case but with a multidirectional density gradient in the multi-mode case.

Analysis of mixing width (amplitude), mixing layer thickness and mixed-mass is performed to highlight the initial condition effect on the temporal development of this flow at different scales. Results indicate that mixing width is not sensitive to initial condition, since it is more indicative of large-scale features. However, mixing layer thickness and mixed-mass do differentiate the single and multi-mode cases as they are more accurate measurements of the actual amount of mixing. Larger mixing layer thickness and higher amounts of mixed-mass are observed before reshock in the multi-mode case at both Mach numbers. After reshock, although mixing layer thickness is similar for all cases, mixed-mass displays a higher growth rate at $M \sim 1.9$ than $M \sim 1.55$ due to the higher density jump after reshock in the former. In addition, the ratio of molecular mixing to entrained fluid is investigated using mixedness. Before reshock, measurements show that mixedness is lower in the high Mach case due to larger amounts of entrained fluid. However after reshock, the trend is vice versa and entrained fluid is more mixed molecularly in the high Mach case.

The density self-correlation at both Mach numbers and initial conditions and the different terms in its evolution equation at the latest time after reshock are measured. The spanwise averaging method is compared with the ensemble-averaging method of calculation and it was shown that there is a significant difference in results when the flow is inhomogeneous. In addition, the DSC computed from ensemble averaging, and fields of different terms in its evolution equation are shown for the first time to illuminate impor-

tant physics in the flow which are concealed by spanwise-averaged profiles. Transport and production terms are observed to be much larger than convection terms in the streamwise direction, and they indicate complementary behaviour which indicates that while the DSC is being produced in the core of the flow, it is being transported to the edges of the mixing region where faster mixing is occurring.

Simultaneous PLIF/PIV measurements are used to analyze the effect of Mach number on localized vorticity and roll-up locations at the latest nondimensional time before reshock in the single-mode case. The correlation between interface crossings and vorticity is observed at the roll-up locations. A higher number of peaks in the vorticity concentration and interface crossings profiles is observed in the higher Mach case. Also, the ratio of total interface length to mixing width is computed and the magnitude for $M \sim 1.9$ is observed to be nearly twice that of $M \sim 1.55$ which indicates a higher perturbation wavenumber, more interface curvature, and greater interface stretching in the high Mach number case.

The turbulent mass-flux fields are shown in addition to spanwise-averaged profiles to further increase understanding of the turbulent mixing in the flow. Before reshock, there is alternating positive and negative turbulent mass-flux along the mixing layer although the amount of negative mass-flux is higher. After reshock, there is a strong negative correlation between velocity and density fluctuations, which indicates transport of lower density fluid into higher density fluid by positive velocity fluctuations and vice versa. In addition, analysis of the contribution of each term in the Favre-averaged Reynolds stress shows that the mass-flux term is the most dependent term on the effects of initial condition and reshock.

Turbulent length scales are measured from small scales using correlation function and spatial gradient methods (which are dependent on resolution). Results suggest that resolution of density fields are fine enough to capture the Taylor microscale. However, Taylor microscales computed from velocity correlation functions are larger by a factor of 3-4 compared to those from Reynolds number.

The state of turbulence in the flow is investigated by analyzing length scales and Reynolds

number. According to Reynolds number criterion suggested by Dimotakis (2000) ($Re \approx 10000 - 20000$), it is observed that the incident shock does not induce mixing transition before reshock, although the multi-mode case at $M \sim 1.9$ is observed to be in the threshold range. However, there is a sharp increase in the Reynolds number, and mixing transition occurs after reshock in the flow. Since Reynolds number criteria were derived based on turbulent jets, and to facilitate further analysis, the time-dependent or diffusion length scale (λ_D) criterion which is suggested by Robey *et al.* (2003) for mixing transition in time dependent flows ($\lambda_D/\lambda_\nu \geq 1$), is also examined in this work. According to the finding from this method, the only time where $\lambda_D/\lambda_\nu > 1$ is at the latest time after reshock. The ratio is close to 1 at the latest time before reshock for the high Mach case and early time after reshock for both Mach numbers.

Turbulent kinetic energy spectra are measured, and showed a jump after reshock, as expected, due to higher energy deposition by reshock to a range of scales. In addition, since the results of mixing-transition analysis suggest that an inertial range forms after reshock, scaling of turbulent kinetic energy spectra at the latest time after reshock is investigated. Power law scaling of -1.8$\pm$0.05 for the low Mach case and -2.1$\pm$0.1 for the higher Mach case are observed which can be related to the high-energy, large-scale, streamwise fluctuations produced by large-scale shear which causes high anisotropy in this flow, and indeed this is found to be the case in the anisotropy analysis, especially in the high Mach case.

5.1 Limitations and Future Work

Although the current work is the first one to collect simultaneous PLIF/PIV measurements after reshock at $M > 1.5$ in shock-driven flow for two different initial conditions, there still exist potential for improvements in future experimental studies. The most important focus should be on creation of multi-mode initial conditions where the modes can be controlled, changed and characterized which is a challenging problem in membrane-less experiments.

In addition, although some statistics like mixedness are going towards an asymptote

value after reshock, it should be noted that the flow in the current work do not reach the late non-dimensional time. Therefore, the effect of initial condition on the behavior of the flow in the asymptotic regime needs further investigations. The other important open question is whether asymptote behavior of the flow after incident shock will be the same as reshock? This can be answered experimentally by investigating and comparing the results of different statistics for two experimental campaigns: 1) Collecting data after the incident shock at a very late non-dimensional time in the asymptotic regime. 2) Collecting data after reshock at a very late non-dimensional time in the asymptotic regime for the same initial condition as case 1. This can be performed by changing the time that reshock hits the interface to the early evolution of flow after the incident shock.

Further, similar initial perturbations can be used to explore two additional problems. First, since this set of experiments are performed at a low Atwood number, a set of experiments at a high Atwood number is needed to obtain data at much later non-dimensional times after the incident shock. These experimental data could be used to further evaluate the accuracy of different analytical models suggested for non-linear regimes by comparing with mixing width (amplitude). Also, different mixing characteristics could be analyzed before and after reshock and later compared with the low Atwood number data provided in the current work. Second, a set of experiments which are zoomed in a small region at the same experimental times can provide further details regarding turbulent length scales. The Batchelor scale can be computed, and then more discussions can be provided regarding the actual scale separation in the energy spectra and structure function.

Moreover, the current literature in shock-driven flows lack experimental data for simultaneous density and temperature measurements. These measurements can be taken using two different laser wavelengths (possibly 308 nm in addition to the existing 266 nm). In the future, density, velocity and temperature may also be captured simultaneously in shock-driven flows by means of improving experimental diagnostic techniques.

Additionally, there are two major drawbacks of classical two dimensional, two-component

PIV using pulse lasers:

First, the out-of-plane component of velocity is unknown in 2D PIV, which is of paramount importance after reshock in RMI as turbulence effects are inherently three dimensional. Using Stereoscopic PIV (Stereo-PIV) technique can solve this issue by enabling one to obtain the out-of-plane component of velocity in addition to streamwise and spanwise components. By combining PLIF and Stereo-PIV, simultaneous density and all three components of velocity can be measured in the flow. However, it should be noted that the error due to refractive index mismatch after reshock can be enhanced by Stereo-PIV measurements and should be considered in the measurements. Stereo-PIV is still two dimensional technique which yields all three components of velocity. To provide additional measurement dimension and resolve all three components and dimensions, Tomographic-PIV can be applied. The thickness of volume should be chosen wisely in this technique to maintain acceptable accuracy. Overall, although simultaneous PLIF/Tomographic-PIV is experimentally expensive however it can provide a three-dimensional flow field.

Second, pulse lasers cannot be used to capture high-speed and unsteady flow phenomena such as RMI. The dynamics of the highly unsteady shock wave/interface interaction is very important to understand this instability. The simultaneous PLIF/PIV measurements using pulse burst lasers with high repetition rate can be used to capture temporal evolution of different density/velocity characteristics in the flow. The processing of PLIF images accurately is more challenging than pulse lasers, since generally in this type of lasers, the energy per pulse is related to the thermal loading that the solid-state lasing elements can tolerate which causes inconsistency between energy of different pulses and therefore intensity of different images.

REFERENCES

[1] M.H. Anderson, B.P. Puranik, J.G. Oakley, P.W. Brooks, and R. Bonazza. "Shock tube investigation of hydrodynamic issues related to inertial confinement fusion". In: *Shock Waves* 10.5 (2000), pp. 377–387.

[2] J. D. Anderson Jr. *Hypersonic and high-temperature gas dynamics*. American Institute of Aeronautics and Astronautics, 2006.

[3] D. Arnett. "The Role of Mixing in Astrophysics". In: *The Astrophysical Journal Supplement Series* 127.2 (2000), p. 213.

[4] B. J. Balakumar, G. C. Orlicz, C. D. Tomkins, and K. P. Prestridge. "Dependence of growth patterns and mixing width on initial conditions in Richtmyer–Meshkov unstable fluid layers". In: *Phys. Scr.* 2008.T132 (2008), p. 014013.

[5] B. J. Balakumar, G. C. Orlicz, C. D. Tomkins, and K. P. Prestridge. "Simultaneous particle-image velocimetry–planar laser-induced fluorescence measurements of Richtmyer–Meshkov instability growth in a gas curtain with and without reshock". In: *Phys. Fluids* 20.12 (2008), p. 124103.

[6] B. J. Balakumar, G. C. Orlicz, J. R. Ristorcelli, S. Balasubramanian, K. P. Prestridge, and C. D. Tomkins. "Turbulent mixing in a Richtmyer–Meshkov fluid layer after reshock: velocity and density statistics". In: *J. Fluid Mech.* 696 (2012), pp. 67–93.

[7] S. Balasubramanian, G. C. Orlicz, K. P. Prestridge, and B. J. Balakumar. "Experimental study of initial condition dependence on Richtmyer–Meshkov instability in the presence of reshock". In: *Phys. Fluids* 24.3 (2012), p. 034103.

[8] A. Banerjee and M. J. Andrews. "3D Simulations to investigate initial condition effects on the growth of Rayleigh–Taylor mixing". In: *Int. J. Heat Mass Transfer* 52.17 (2009), pp. 3906–3917.

[9] G.K. Batchelor. "Computation of the energy spectrum in homogeneous two-dimensional turbulence". In: *Phys. Fluids* 12.12 (1969), pp. II–233.

[10] J. S. Bendat and A. G. Piersol. *Random data: analysis and measurement procedures*. John Wiley & Sons, 2011.

[11] L. H. Benedict and R. D. Gould. "Towards better uncertainty estimates for turbulence statistics". In: *Exp. Fluids* 22.2 (1996), pp. 129–136.

[12] G. Berkooz, P. Holmes, and J. L. Lumley. “The proper orthogonal decomposition in the analysis of turbulent flows”. In: *Annu. Rev. Fluid Mech.* 25.1 (1993), pp. 539–575.

[13] D. Besnard, F. H. Harlow, R. M. Rauenzahn, and C. Zemach. *Turbulence transport equations for variable-density turbulence and their relationship to two-field models*. Tech. rep. Los Alamos National Lab., lA-12303-MS, 1992.

[14] B.E. Blue, S.V. Weber, S.G. Glendinning, N.E. Lanier, D.T. Woods, M.J. Bono, S.N. Dixit, C.A. Haynam, J.P. Holder, D.H. Kalantar, B. MacGowan, A. Nikitin, V. Rekow, E. Van Wonterghem B.and Moses, P. Stry, B. Wilde, W. Hsing, and H. Robey. “Experimental investigation of high-Mach-number 3D hydrodynamic jets at the National Ignition Facility”. In: *Phys. rev. letters* 94.9 (2005), p. 095005.

[15] R. Bonazza and B. Sturtevant. “X-ray measurements of growth rates at a gas interface accelerated by shock waves”. In: *Phys. Fluids* 8.9 (1996), pp. 2496–2512.

[16] M. Brouillette. “The Richtmyer–Meshkov instability”. In: *Annu. Rev. Fluid Mech.* 34.1 (2002), pp. 445–468.

[17] M. Brouillette and B. Sturtevant. “Experiments on the Richtmyer–Meshkov instability: single-scale perturbations on a continuous interface”. In: *J. Fluid Mech.* 263 (1994), pp. 271–292.

[18] M. Brouillette and B. Sturtevant. “Growth induced by multiple shock waves normally incident on plane gaseous interfaces”. In: *Physica D: Nonlinear Phenomena* 37.1-3 (1989), pp. 248–263.

[19] J. Canny. “A computational approach to edge detection”. In: *IEEE Transactions on pattern analysis and machine intelligence* 6 (1986), pp. 679–698.

[20] F. H. Champagne, V. G. Harris, and S. Corrsin. “Experiments on nearly homogeneous turbulent shear flow”. In: *J. Fluid Mech.* 41.1 (1970), pp. 81–139.

[21] P. R. Chapman and J.W. Jacobs. “Experiments on the three-dimensional incompressible Richtmyer-Meshkov instability”. In: *Phys. Fluids* 18.7 (2006), p. 074101.

[22] J. J. Charonko and P. P. Vlachos. “Estimation of uncertainty bounds for individual particle image velocimetry measurements from cross-correlation peak ratio”. In: *Meas. Sci. Tech.* 24.6 (2013), p. 065301.

[23] B. D. Collins and J. W. Jacobs. “PLIF flow visualization and measurements of the Richtmyer–Meshkov instability of an air/SF6 interface”. In: *J. Fluid Mech.* 464 (2002), pp. 113–136.

[24] A. W. Cook. “Artificial fluid properties for large-eddy simulation of compressible turbulent mixing”. In: *Phys. Fluids* 19.5 (2007), p. 055103.

[25] A. W. Cook and W. H. Cabot. “Hyperviscosity for shock-turbulence interactions”. In: *J. Comput. Phys.* 203.2 (2005), pp. 379–385.

[26] S. B. Dalziel. “Rayleigh-Taylor instability: experiments with image analysis”. In: *Dynamics of Atmospheres and Oceans* 20.1-2 (1993), pp. 127–153.

[27] G. Dimonte and M. Schneider. “Turbulent Rayleigh-Taylor instability experiments with variable acceleration”. In: *Phys. rev. E* 54.4 (1996), p. 3740.

[28] G. Dimonte and M. Schneider. “Turbulent Richtmyer–Meshkov instability experiments with strong radiatively driven shocks”. In: *Phys. Plasmas* 4.12 (1997), pp. 4347–4357.

[29] Guy Dimonte and Marilyn Schneider. “Density ratio dependence of Rayleigh–Taylor mixing for sustained and impulsive acceleration histories”. In: *Phys. Fluids* 12.2 (2000), pp. 304–321.

[30] P. E. Dimotakis. “The mixing transition in turbulent flows”. In: *J. Fluid Mech.* 409 (2000), pp. 69–98.

[31] P. E. Dimotakis. “Turbulent mixing”. In: *Annu. Rev. Fluid Mech.* 37 (2005), pp. 329–356.

[32] L. Erez, O. Sadot, D. Oron, G. Erez, L. A. Levin, D. Shvarts, and G. Ben-Dor. “Study of the membrane effect on turbulent mixing measurements in shock tubes”. In: *Shock Waves* 10.4 (2000), pp. 241–251.

[33] D. Fries, A. O. Bradley, A. Saha, Ranjan D., and S. Menon. “Flame Speed Characteristics of Turbulent Expanding Flames in a Rectangular Channel”. In: *Combustion and Flame* 199C (2019), pp. 1–13.

[34] W. K. George. “Is there an asymptotic effect of initial and upstream conditions on turbulence?” In: *ASME 2008 Fluids Engineering Division Summer Meeting collocated with the Heat Transfer, Energy Sustainability, and 3rd Energy Nanotechnology Conferences*. American Society of Mechanical Engineers. 2008, pp. 647–672.

[35] W. K. George and L. Davidson. “Role of initial conditions in establishing asymptotic flow behavior”. In: *AIAA J.* 42.3 (2004), pp. 438–446.

[36] E.C. Harding, J.F. Hansen, O.A. Hurricane, R.P. Drake, H.F. Robey, C.C. Kuranz, B.A. Remington, M.J. Bono, M.J. Grosskopf, and R.S. Gillespie. “Observation of a

kelvin-helmholtz instability in a high-energy-density plasma on the omega laser". In: *Phys. rev. letters* 103.4 (2009), p. 045005.

[37] D. J. Hill, C. Pantano, and D. I. Pullin. "Large-eddy simulation and multiscale modelling of a Richtmyer–Meshkov instability with reshock". In: *J. Fluid Mech.* 557 (2006), pp. 29–61.

[38] W. J. Hogan, R. Bangerter, and G. L. Kulcinski. "Energy from inertial fusion". In: *Physics Today* 45.9 (1992).

[39] L. Houas and I. Chemouni. "Experimental investigation of Richtmyer–Meshkov instability in shock tube". In: *Phys. Fluids* 8.2 (1996), pp. 614–627.

[40] J. W. Jacobs. "Shock-induced mixing of a light-gas cylinder". In: *J. Fluid Mech.* 234 (1992), pp. 629–649.

[41] J. W. Jacobs and I. Catton. "Three-dimensional Rayleigh-Taylor instability Part 2. Experiment". In: *J. Fluid Mech.* 187 (1988), pp. 353–371.

[42] J. W. Jacobs and J. M. Sheeley. "Experimental study of incompressible Richtmyer–Meshkov instability". In: *Phys. Fluids* 8.2 (1996), pp. 405–415.

[43] J. W. Jacobs, V. V. Krivets, V. Tsiklashvili, and O. A. Likhachev. "Experiments on the Richtmyer–Meshkov instability with an imposed, random initial perturbation". In: *Shock Waves* 23.4 (2013), pp. 407–413.

[44] J.W. Jacobs and S.B. Dalziel. "Rayleigh–Taylor instability in complex stratifications". In: *J. Fluid Mech.* 542 (2005), pp. 251–279.

[45] M. A. Jones and J. W. Jacobs. "A membraneless experiment for the study of Richtmyer–Meshkov instability of a shock-accelerated gas interface". In: *Phys. Fluids* 9.10 (1997), pp. 3078–3085.

[46] J. Kane, R. P. Drake, and B. A. Remington. "An evaluation of the Richtmyer–Meshkov instability in supernova remnant formation". In: *Astrophys. J.* 511.1 (1999), p. 335.

[47] A. R. Kerstein. "Linear-eddy modelling of turbulent transport. Part 6. Microstructure of diffusive scalar mixing fields". In: *J. Fluid Mech.* 231 (1991), pp. 361–394.

[48] K. Kifonidis, T. Plewa, L. Scheck, H. Janka, and E. Müller. "Non-spherical core collapse supernovae-II. The late-time evolution of globally anisotropic neutrino-driven explosions and their implications for SN 1987 A". In: *Astronomy & Astrophysics* 453.2 (2006), pp. 661–678.

[49] R.H. Kraichnan. “Inertial ranges in two-dimensional turbulence”. In: *Phys. Fluids* 10.7 (1967), pp. 1417–1423.

[50] S. Kuchibhatla and D. Ranjan. “Effect of initial conditions on Rayleigh–Taylor mixing: modal interaction”. In: *Phys. Scr.* 2013.T155 (2013), p. 014057.

[51] M. Latini, O. Schilling, and W. Don. “Effects of WENO flux reconstruction order and spatial resolution on reshocked two-dimensional Richtmyer–Meshkov instability”. In: *J. Comput. Phys.* 221.2 (2007), pp. 805–836.

[52] P. Lavoie, G. Avallone, F. De Gregorio, G. Romano, and R. Antonia. “Spatial resolution of PIV for the measurement of turbulence”. In: *Exp. Fluids* 43.1 (2007), pp. 39–51.

[53] E. Leinov, G. Malamud, Y. Elbaz, L. A. Levin, G. Ben-Dor, D. Shvarts, and O. Sadot. “Experimental and numerical investigation of the Richtmyer–Meshkov instability under re-shock conditions”. In: *J. Fluid Mech.* 626 (2009), pp. 449–475.

[54] J. Lindl, O. Landen, J. Edwards, E. d. Moses, NIC Team, *et al.* “Review of the National Ignition Campaign 2009-2012”. In: *Phys. Plasmas* 21.2 (2014), p. 020501.

[55] D. Livescu and J. R. Ristorcelli. “Variable-density mixing in buoyancy-driven turbulence”. In: *J. Fluid Mech.* 605 (2008), pp. 145–180.

[56] M. Lombardini, D. I. Pullin, and D. I. Meiron. “Transition to turbulence in shock-driven mixing: a Mach number study”. In: *J. Fluid Mech.* 690 (2012), pp. 203–226.

[57] C.C. Long, V.V. Krivets, J.A. Greenough, and J. W. Jacobs. “Shock tube experiments and numerical simulation of the single-mode, three-dimensional Richtmyer–Meshkov instability”. In: *Phys. Fluids* 21.11 (2009), p. 114104.

[58] X. Luo, P. Dong, T. Si, and Z. Zhai. “The Richtmyer–Meshkov instability of a ’V’shaped air/SF6 interface”. In: *J. Fluid Mech.* 802 (2016), pp. 186–202.

[59] H. Malm, G. Sparr, J. Hult, and C. F. Kaminski. “Nonlinear diffusion filtering of images obtained by planar laser-induced fluorescence spectroscopy”. In: *Josa a* 17.12 (2000), pp. 2148–2156.

[60] F. E. Marble, G. J. Hendricks, and E. E. Zukoski. “Progress toward shock enhancement of supersonic combustion processes”. In: *Turbulent Reactive Flows*. Springer, 1989, pp. 932–950.

[61] J. McFarland, J. Greenough, and D. Ranjan. “Simulations and analysis of the reshocked inclined interface Richtmyer–Meshkov instability for linear and nonlinear interface perturbations”. In: *Trans. ASME: J. Fluids Engng* 136.7 (2014), p. 071203.

[62] J. McFarland, D. Reilly, S. Creel, C. McDonald, T. Finn, and D. Ranjan. “Experimental investigation of the inclined interface Richtmyer–Meshkov instability before and after reshock”. In: *Exp. Fluids* 55.1 (2014), pp. 1–14.

[63] J. A. McFarland, J. A. Greenough, and D. Ranjan. “Computational parametric study of a Richtmyer–Meshkov instability for an inclined interface”. In: *Phys. Rev. E* 84.2 (2011), p. 026303.

[64] J. A. McFarland, D. Reilly, W. Black, J. A. Greenough, and D. Ranjan. “Modal interactions between a large-wavelength inclined interface and small-wavelength multimode perturbations in a Richtmyer–Meshkov instability”. In: *Phys. Rev. E* 92.1 (2015), p. 013023.

[65] E. E. Meshkov. “Instability of the interface of two gases accelerated by a shock wave”. In: *Fluid Dyn.* 4.5 (1969), pp. 101–104.

[66] K. O. Mikaelian. “Oscillations of a standing shock wave generated by the Richtmyer–Meshkov instability”. In: *Phys. Rev. Fluids* 1.3 (2016), p. 033601.

[67] K. O. Mikaelian. “Turbulent mixing generated by Rayleigh–Taylor and Richtmyer–Meshkov instabilities”. In: *Phys. D* 36.3 (1989), pp. 343–357.

[68] A.R. Miles, B. Blue, M.J. Edwards, J.A. Greenough, J.F. Hansen, H.F. Robey, R.P. Drake, C. Kuranz, and D.R. Leibrandt. “Transition to turbulence and effect of initial conditions on three-dimensional compressible mixing in planar blast-wave-driven systems”. In: *Phys. plasmas* 12.5 (2005), p. 056317.

[69] P. L. Miller and P. E. Dimotakis. “Measurements of scalar power spectra in high Schmidt number turbulent jets”. In: *J. Fluid Mech.* 308 (1996), pp. 129–146.

[70] M. Mohaghar, J. Carter, B. Musci, D. Reilly, J. McFarland, and D. Ranjan. “Evaluation of turbulent mixing transition in a shock-driven variable-density flow”. In: *J. Fluid Mech.* 831 (2017), pp. 779–825.

[71] D. C. Montgomery and G. C. Runger. *Applied statistics and probability for engineers*. John Wiley & Sons, 2010.

[72] J. T. Morán-López and O. Schilling. “Multicomponent Reynolds-averaged Navier–Stokes simulations of reshocked Richtmyer–Meshkov instability-induced mixing”. In: *High Energy Density Physics* 9.1 (2013), pp. 112–121.

[73] R. V. Morgan, R. Aure, J. D. Stockero, J. A. Greenough, W. Cabot, O. A. Likhachev, and J. W. Jacobs. “On the late-time growth of the two-dimensional Richtmyer–Meshkov instability in shock tube experiments”. In: *J. Fluid Mech.* 712 (2012), pp. 354–383.

[74] B. Motl, J. Oakley, D. Ranjan, C. Weber, M. Anderson, and R. Bonazza. “Experimental validation of a Richtmyer–Meshkov scaling law over large density ratio and shock strength ranges”. In: *Phys. Fluids* 21.12 (2009), p. 126102.

[75] C. E. Niederhaus and J. W. Jacobs. “Experimental study of the Richtmyer–Meshkov instability of incompressible fluids”. In: *J. Fluid Mech.* 485 (2003), pp. 243–277.

[76] J. H. J. Niederhaus, J. A. Greenough, J. G. Oakley, D. Ranjan, M. H. Anderson, and R. Bonazza. “A computational parameter study for the three-dimensional shock–bubble interaction”. In: *J. Fluid Mech.* 594 (2008), pp. 85–124.

[77] D. H. Olson and J. W. Jacobs. “Experimental study of Rayleigh–Taylor instability with a complex initial perturbation”. In: *Phys. Fluids* 21.3 (2009), p. 034103.

[78] G. C. Orlicz, S. Balasubramanian, and K. P. Prestridge. “Incident shock Mach number effects on Richtmyer–Meshkov mixing in a heavy gas layer”. In: *Phys. Fluids* 25.11 (2013), p. 114101.

[79] G. C. Orlicz, B. J. Balakumar, C. D. Tomkins, and K. P. Prestridge. “A Mach number study of the Richtmyer–Meshkov instability in a varicose, heavy-gas curtain”. In: *Phys. Fluids* 21.6 (2009), p. 064102.

[80] G. C. Orlicz, S. Balasubramanian, P. Vorobieff, and K. P. Prestridge. “Mixing transition in a shocked variable-density flow”. In: *Phys. Fluids* 27.11 (2015), p. 114102.

[81] S. B. Pope. *Turbulent flows*. Cambridge University Press, 2000.

[82] J.K. Prasad, A. Rasheed, S. Kumar, and B. Sturtevant. “The late-time development of the Richtmyer–Meshkov instability”. In: *Phys. Fluids* 12.8 (2000), pp. 2108–2115.

[83] J. J. Quirk and S. Karni. “On the dynamics of a shock–bubble interaction”. In: *J. Fluid Mech.* 318 (1996), pp. 129–163.

[84] M. Raffel, C. E. Willert, F. Scarano, C. J. Kähler, S. T. Wereley, and J. Kompenhans. *Particle image velocimetry: a practical guide*. Springer, 2018.

[85] P. Ramaprabhu and M. J. Andrews. “Experimental investigation of Rayleigh–Taylor mixing at small Atwood numbers”. In: *J. Fluid Mech.* 502 (2004), pp. 233–271.

[86] D. Ranjan, J. Oakley, and R. Bonazza. “Shock-bubble interactions”. In: *Annu. Rev. Fluid Mech.* 43 (2011), pp. 117–140.

[87] D. Ranjan, M. Anderson, J. Oakley, and R. Bonazza. “Experimental investigation of a strongly shocked gas bubble”. In: *Phys. rev. letters* 94.18 (2005), p. 184507.

[88] K.I. Read. “Experimental investigation of turbulent mixing by Rayleigh-Taylor instability”. In: *Physica D Nonlinear Phenomena* 12 (1984), pp. 45–58.

[89] D. T. Reese, A. M. Ames, C. D. Noble, J. G. Oakley, D. A. Rothamer, and R. Bonazza. “Simultaneous direct measurements of concentration and velocity in the Richtmyer–Meshkov instability”. In: *J. Fluid Mech.* 849 (2018), pp. 541–575.

[90] D. Reilly, J. McFarland, M. Mohaghar, and D. Ranjan. “The effects of initial conditions and circulation deposition on the inclined-interface reshocked Richtmyer–Meshkov instability”. In: *Exp. Fluids* 56.8 (2015), pp. 1–16.

[91] R. Reisenhofer, J. Kiefer, and E. J. King. “Shearlet-based detection of flame fronts”. In: *Exp. Fluids* 57.3 (2016), p. 41.

[92] R. D. Richtmyer. “Taylor instability in shock acceleration of compressible fluids”. In: *Commun. Pure Appl. Maths* 13.2 (1960), pp. 297–319.

[93] H. F. Robey, Y. e. Zhou, A. C. Buckingham, P. Keiter, B. A. Remington, and R. P. Drake. “The time scale for the transition to turbulence in a high Reynolds number, accelerated flow”. In: *Phys. Plasmas* 10.3 (2003), pp. 614–622.

[94] O. Sadot, L. Erez, U. Alon, D. Oron, L. A. Levin, G. Erez, G. Ben-Dor, and D. Shvarts. “Study of nonlinear evolution of single-mode and two-bubble interaction under Richtmyer-Meshkov instability”. In: *Phys. rev. letters* 80.8 (1998), p. 1654.

[95] O. Schilling and M. Latini. “High-order WENO simulations of three-dimensional reshocked Richtmyer–Meshkov instability to late times: dynamics, dependence on initial conditions, and comparisons to experimental data”. In: *Math. Acta Sci.* 30.2 (2010), pp. 595–620.

[96] O. Schilling, M. Latini, and W. S. Don. “Physics of reshock and mixing in single-mode Richtmyer–Meshkov instability”. In: *Phys. Rev. E* 76.2 (2007), p. 026319.

[97] J. D. Schwarzkopf, D. Livescu, J. R. Baltzer, R. A. Gore, and J. R. Ristorcelli. “A Two-length Scale Turbulence Model for Single-phase Multi-fluid Mixing”. In: *Flow Turbul. Combust.* 96.1 (2016), pp. 1–43.

[98] S. K. Shankar and S. K. Lele. “Numerical investigation of turbulence in reshocked Richtmyer–Meshkov unstable curtain of dense gas”. In: *Shock Waves* 24.1 (2014), pp. 79–95.

[99] C. D. Slabaugh, A. C. Pratt, and R. P. Lucht. “Simultaneous 5 kHz OH-PLIF/PIV for the study of turbulent combustion at engine conditions”. In: *Applied Physics B* 118.1 (2015), pp. 109–130.

[100] S. M. Soloff, R. J. Adrian, and Z. Liu. “Distortion compensation for generalized stereoscopic particle image velocimetry”. In: *Meas. Sci. Tech.* 8.12 (1997), p. 1441.

[101] M. Stanislas and J. Monnier. “Practical aspects of image recording in particle image velocimetry”. In: *Meas. Sci. Tech.* 8.12 (1997), p. 1417.

[102] J. W. Strutt. “Investigation of the character of the equilibrium of an incompressible heavy fluid of variable density”. In: *Scientific Papers* (1900), pp. 200–207.

[103] M. Sweeney and S. Hochgreb. “Autonomous extraction of optimal flame fronts in OH planar laser-induced fluorescence images”. In: *Applied optics* 48.19 (2009), pp. 3866–3877.

[104] S. Tavoularis and S. Corrsin. “Experiments in nearly homogeneous turbulent shear flow with a uniform mean temperature gradient. Part 2. The fine structure”. In: *J. Fluid Mech.* 104 (1981), pp. 349–367.

[105] S. Tavoularis and S. Corrsin. “Experiments in nearly homogenous turbulent shear flow with a uniform mean temperature gradient. Part 1”. In: *J. Fluid Mech.* 104 (1981), pp. 311–347.

[106] G. Taylor. “The instability of liquid surfaces when accelerated in a direction perpendicular to their planes. I”. In: 201.1065 (1950), pp. 192–196.

[107] B. Thornber, D. Drikakis, D. L. Youngs, and R. J. R. Williams. “Growth of a Richtmyer–Meshkov turbulent layer after reshock”. In: *Phys. Fluids* 23.9 (2011), p. 095107.

[108] B. Thornber, D. Drikakis, D. L. Youngs, and R. J. R. Williams. “Growth of a Richtmyer-Meshkov turbulent layer after reshock”. In: *Phys. Fluids* 23.9 (2011), p. 095107.

[109] B. Thornber, D. Drikakis, D. L. Youngs, and R. J. R. Williams. “Physics of the single-shocked and reshocked Richtmyer–Meshkov instability”. In: *J. Turbul.* 13.1 (2012), N10.

[110] C. Tomkins, K. Prestridge, P. Rightley, M. Marr-Lyon, P. Vorobieff, and R. Benjamin. “A quantitative study of the interaction of two Richtmyer–Meshkov-unstable gas cylinders”. In: *Physics of Fluids* 15.4 (2003), pp. 986–1004.

[111] C. D. Tomkins, B. J. Balakumar, G. Orlicz, K. P. Prestridge, and J. R. Ristorcelli. “Evolution of the density self-correlation in developing Richtmyer–Meshkov turbulence”. In: *J. Fluid Mech.* 735 (2013), pp. 288–306.

[112] V. K. Tritschler, B. J. Olson, S. K. Lele, S. Hickel, X. Y. Hu, and N. A. Adams. “On the Richtmyer–Meshkov instability evolving from a deterministic multimode planar interface”. In: *J. Fluid Mech.* 755 (2014), pp. 429–462.

[113] S. Ukai, K. Balakrishnan, and S. Menon. “Growth rate predictions of single-and multi-mode Richtmyer–Meshkov instability with reshock”. In: *Shock Waves* 21.6 (2011), p. 533.

[114] M. Vetter and B. Sturtevant. “Experiments on the Richtmyer–Meshkov instability of an air/SF6 interface”. In: *Shock Waves* 4.5 (1995), pp. 247–252.

[115] P. Vorobieff, P. M. Rightley, and R. F. Benjamin. “Power-law spectra of incipient gas-curtain turbulence”. In: *Phys. Rev. Lett.* 81.11 (1998), p. 2240.

[116] P. Vorobieff, N. G. Mohamed, C. Tomkins, C. Goodenough, M. Marr-Lyon, and R. F. Benjamin. “Scaling evolution in shock-induced transition to turbulence”. In: *Phys. Rev. E* 68.6 (2003), p. 065301.

[117] I. A. Waitz, F. E. Marble, and E. E. Zukoski. “Investigation of a contoured wall injector for hypervelocity mixing augmentation”. In: *AIAA J.* 31.6 (1993), pp. 1014–1021.

[118] C. Weber. “Turbulent Mixing Measurements in the Richtmyer-Meshkov Instability”. PhD thesis. The University of Wisconsin-Madison, 2012.

[119] C. Weber, A. Cook, and R. Bonazza. “Growth rate of a shocked mixing layer with known initial perturbations”. In: *J. Fluid Mech.* 725 (2013), pp. 372–401.

[120] C. R. Weber, Nicholas S. Haehn, J. G. Oakley, D. A. Rothamer, and R. Bonazza. “An experimental investigation of the turbulent mixing transition in the Richtmyer–Meshkov instability”. In: *J. Fluid Mech.* 748 (2014), pp. 457–487.

[121] C. R. Weber, N. Haehn, J. Oakley, D. Rothamer, and R. Bonazza. “Turbulent mixing measurements in the Richtmyer–Meshkov instability”. In: *Phys. Fluids* 24.7 (2012), p. 074105.

[122] B. Wieneke. “PIV uncertainty quantification from correlation statistics”. In: *Meas. Sci. Tech.* 26.7 (2015), p. 074002.

[123] Z. Xue, J. J. Charonko, and P. P. Vlachos. “Particle image velocimetry correlation signal-to-noise ratio metrics and measurement uncertainty quantification”. In: *Meas. Sci. Tech.* 25.11 (2014), p. 115301.

[124] Q. Yang, J. Chang, and W. Bao. “Richtmyer–Meshkov Instability Induced Mixing Enhancement in the Scramjet Combustor with a Central Strut”. In: *Advances in Mechanical Engineering* 6 (2014), p. 614189.

[125] N. J. Zabusky. “Vortex paradigm for accelerated inhomogeneous flows: Visiometrics for the Rayleigh-Taylor and Richtmyer-Meshkov environments”. In: *Annu. Rev. Fluid Mech.* 31.1 (1999), pp. 495–536.

[126] Q. Zhang and S. Sohn. “Nonlinear theory of unstable fluid mixing driven by shock wave”. In: *Phys. Fluids* 9.4 (1997), pp. 1106–1124.

[127] Y. Zhou. “A scaling analysis of turbulent flows driven by Rayleigh–Taylor and Richtmyer–Meshkov instabilities”. In: *Phys. Fluids* 13.2 (2001), pp. 538–543.

[128] Y. Zhou. “Rayleigh–Taylor and Richtmyer-Meshkov instability induced flow, turbulence, and mixing. II”. In: *Phys. Reports* (2017).

[129] Y. Zhou, W. H. Cabot, and B. Thornber. “Asymptotic behavior of the mixed mass in Rayleigh–Taylor and Richtmyer–Meshkov instability induced flows”. In: *Phys. Plasmas* 23.5 (2016), p. 052712.

VITA

Mohammad Mohaghar was born in Bojnord and raised in Tehran, Iran. He graduated with a B.Sc. in Mechanical Engineering from University of Tehran in 2008, and finished his first M.Sc. degree in Automotive Engineering at Iran University of Science and Technology in 2010. Then, he had over three years of industrial work experience in some of the most prestigious companies in Iran like Mapna Co. Then to fulfill his dream of becoming a professor, he applied for an M.Sc. degree in Energy for Stainability at University of Coimbra in Portugal which was a joint program with MIT. In October 2013, he applied for a PhD in Civil Engineering (Environmental Fluid Mechanics group) at Georgia Tech, however, he later transferred his major of study to Mechanical Engineering in Fall 2014 to work under the supervision of Prof. Devesh Ranjan. During his PhD, he learned experimental skills in addition to the computational ones he had gained back home and in Europe.